Alma Mater Studiorum – Università di Bologna

DOTTORATO DI RICERCA IN

Meccanica e Scienze Avanzate dell'Ingegneria

Ciclo XXXI

Settore Concorsuale: 09/A1 Ingegneria Aeronautica, Aerospaziale e Navale

Settore Scientifico Disciplinare: ING-IND/05 Impianti e Sistemi Aerospaziali

DEVELOPMENT OF METHODS FOR THE GLOBAL EPHEMERIDES ESTIMATION OF THE GAS GIANT SATELLITE SYSTEMS

Presentata da: Luis Gómez Casajús

Coordinatore Dottorato **Supervisore**

Prof. Marco Carricato **Prof. Paolo Tortora**

Esame finale anno 2019

A Mamá y Papá.

Author's Note

This thesis is continuously revised to correct all typos that are found during a never-ending revision process. To obtain the most updated version, please feel free to contact the author by sending an e-mail to: `luis.gomezcasajus@unibo.it`.

Development of methods for the global ephemerides estimation of the gas giant satellite systems

Summary

The satellite systems of Saturn and Jupiter are complex dynamical systems, with several interactions happening between the central body, its rings and the natural satellites, such as orbital resonances, tidal interactions or librations.

During the last two decades, unmanned probes allowed to study the gas giant satellite systems. The three most relevant spacecrafts to their study have been Galileo, Cassini and Juno.

Galileo studied the Jupiter system, the primary body and the main moons during 8 years, despite the failure on the deployment of its high gain antenna that limited the science retrieval. Cassini, analogously, studied during most of the 13 years of its mission, the natural satellites, paying specific attention to Titan, the biggest moon of the system and the only one of the solar system with a thick atmosphere. In addition, the probe studied the most iconic planetary rings of the entire solar system.

Then, in 2017 both Cassini and Juno spacecrafts were used to carry out gravity measurements of Saturn and Jupiter. Both spacecraft were inserted into similar, almost polar, highly eccentric orbits with low pericenter altitudes. Tracking the motion of the probes during pericenter passes from the DSN enabled the retrieval of the gravity field of both gas giants at an unprecedented level of accuracy. These results provide constraints on the interiors of the gas giants, but also, on the satellite system ephemerides which, analogously, hold information on the properties and evolution of both the satellites themselves and the central body.

The main aim of this project is to study and characterize the key dynamics that rule the gas giant satellite systems using an improved gravity field of the central body, estimated using radio tracking data of deep space probes. To accomplish our objective, we performed the data analysis of the previously mentioned deep space missions: Cassini, Juno and Galileo. Being the three probes the very first orbiters of gas giant planets, they provided, and still provide, precious information which contributes to unveil the gas giant satellite systems dynamics, their origin and evolution.

This dissertation thesis is organized as follows: Chapter 1 overviews the unique three missions that ever performed an orbit insertion of an outer planet: Galileo, Cassini-Huygens and Juno. The chapter explains in detail the main objectives of the missions and the corresponding radio science subsystems, that allowed the measurement of the gravity field of the involved bodies and the reconstruction of the trajectories, of both the probe and the natural satellites. Chapter 2 introduces the mathematical formulation of the orbit determination problem and presents the different multi-arc approach strategies used in this work. Chapter 3 reviews the main mechanisms that rule the satellite systems dynamics, used in the integration of the celestial bodies trajectories, paying specific atten-

tion to the tidal interactions and how they can govern the orbital evolution of a satellite system. Chapter 4 describes in detail the data analysis performed with the radio tracking data of Cassini, which allowed to measure the gravity field of Saturn and its biggest moon Titan. Moreover, we focused on the study of the orbital evolution of Titan, allowed by the single-satellite global approach, finding constraints on the dissipation of Saturn and obtaining the first estimation of the quality factor of Saturn at Titan's frequency using radiometric observables. Similarly, Chapter 5 is dedicated to the data-analysis of Galileo and Juno, the two orbiters that studied the Jupiter system. We demonstrate how the accurate measurements of the gravity field of Jupiter, recently obtained by Juno, together with the local multi-arc approach, can help to improve the Galilean moon gravity results obtained by Galileo. This chapter will also focus on the Io plasma torus and the potential effect that may have on the gravity experiments, proposing methods to improve the current models and study its time-variability.

Finally, Chapter 6 will present the conclusions and the future work perspectives.

Acknowledgements

First of all I would like to thank my advisor, Professor Paolo Tortora, for introducing me the radio science field and offering me the opportunity of carrying the PhD research presented in this thesis. During this 3 years I learnt and discovered a field of great interest for me.

I would also like to thank Marco Zannoni, without him this research would not have been possible. I am grateful, not only for the support and advice, essential for the projects and research that I was involved in, but also for his friendship.

I wish to sincerely acknowledge Kamal Oudrhiri, for letting me join his team in the JPL. It was great to be a JPL'er, to be involved in the Radio Science Team and experience the work dynamics of a space agency.

A huge thank to Daniele Durante, for all the interesting discussions and the never ending suggestions that helped in the growth of this thesis. Also I would like to thank Paolo Raccioppa. Every discussion with them was a learning experience.

I wish to express my sincere gratitude to Valery Lainey for the help and the collaboration that he provided me, before, during and after my stay in the JPL.

A huge thank goes to all my laboratory fellows, for the great moments that we shared during these last 3 years, for the interesting and hilarious discussions, for being friends instead of just colleagues.

Heartfelt thanks to Cècile, who was always present and encouraged me to follow my dreams.

Last but not least, my warmest thanks to my family, Mamá, Papá, Cris and Abuela, for their love and sacrifice, and for their ever-present support that always encouraged me to reach my goals.

Contents

Chapter 1

The gas giant satellite system exploration

Contents

1.1 Introduction

The exploration of the gas giant satellite systems began with simple naked-eye observations of both Jupiter and Saturn in the ancient times, but was not until the 70's when our knowledge of the satellite systems started to grow exponentially thanks to the in-situ observations acquired by unmanned probes.

Galileo Galilei discovered in 1610 that Jupiter was the primary body of a satellite system composed by four moons; Io, Europa, Ganymede and Callisto. Subsequently, more natural satellites have been discovered and nowadays we know that the Jupiter system is populated by 79 moons [2].

Christiaan Huygens, a Dutch astronomer, discovered Titan the 25th of March, 1655, revealing that also Saturn had a satellite system. In addition, Huygens intuited that Saturn had a ring-system. A few years later the Italian astronomer Giovanni Domenico Cassini discovered Iapetus (1671), Rhea (1672), Dione and Tethys (1684). Hereinafter, more moons have been discovered and up to the moment, the Saturn system contains 62 moons with confirmed orbits [2].

The very first in-situ exploration of a gas giant satellite system was carried out by Pioneer-10, during its flyby with Jupiter in December, 1973, that took the first close-up images of the Galilean moons and Jupiter. It was followed one year later by Pioneer-11, that subsequently would become the first unmanned probe to arrive to the Saturn system.

After the Pioneers, the Voyager program took up the baton and continued with the exploration of the outer planets. Voyager-2 acquired observations, not only of Jupiter and Saturn but also of Uranus and Neptune during its flybys.

Almost two decades after the Voyagers, Galileo released an atmospheric probe into Jupiter's atmosphere and became the first gas giant orbiter, after performing the very first Jupiter Orbit Insertion (JOI) manoeuvre. In the same way, Cassini has been the very first spacecraft (S/C) that ever performed a Saturn Orbit Insertion (SOI) manoeuvre.

After the spectacular end of the Cassini mission in 2017, the only mission that is studying an outer planet is Juno, which is planned to be followed by JUICE and Europa Clipper in the near future. Table 1.1 provides a list of the different missions that visited the gas giant satellite systems of Jupiter and Saturn.

Table 1.1 – Missions that explored the gas giant satellite systems of Jupiter and Saturn.

Mission	Jupiter system	Saturn system
Pioneer-10	Flyby (1973)	
Pioneer-11	Flyby (1974)	Flyby (1979)
Voyager-1	Flyby (1979)	Flyby (1980)
Voyager-2	Flyby (1979)	Flyby (1981)
Galileo	Orbiter (1995-2003)	
Ulysses	Gravity-assist (1992 and 2004)	
Cassini-Huygens	Gravity-assist (2000)	Orbiter and lander (2004-2017)
New Horizons	Gravity-assist (2007)	
Juno	Orbiter (2006-2019)	
JUICE	Planned Orbiter (2030's)	
Europa-Clipper	Planned Orbiter (2030's)	

Of all the missions that visited the Jupiter and the Saturn systems, only three of them were orbiters: Galileo, that studied the system of Jupiter during 8 years, Juno, that has the objective of unveiling the interior of the gas giant and is currently orbiting around Jupiter, and finally Cassini, that studied the Saturn system for 13 years.

In this chapter we will introduce this three orbiter missions; the S/C's, the navigation processes, the payloads and, in detail, the radio science subsystem that will serve us to our scope, the study of the gravity and the satellite orbital evolution of the gas giant satellite systems.

1.2 The Galileo mission

Galileo was launched the 18th of October, 1989 from the Kennedy Space Center and after 6 years of interplanetary trajectory, known as VEEGA (Venus-Earth-Earth gravity assist), arrived to the Jupiter system. On April, 1991, Galileo's umbrella-like high gain antenna (HGA) failed to deploy. Therefore, the only way to navigate the S/C was through its low gain antenna (LGA), using the S-band and a reduced set of optical navigation images. Due to the HGA deployment failure, the data-rate was reduced to 8-16 bps from 134.4 kbps, that were planned with the X-band HGA. On-board software changes allowed compression and increased the data-rate up to 160 bps. The X-band Doppler data, less susceptible to the dispersive noise, was expected to have an accuracy of 0.5 mm/s. The antenna deployment failure downgraded the accuracy to 1.0 mm/s [11].

During its cruise, Galileo became the first probe that acquired close observations of Gaspra and Ida asteroids, discovering Dactyl, the first discovered moon of an asteroid. The 7th of December, 1995, Galileo's atmospheric probe accomplished the most difficult atmospheric entry to that moment. Shortly after, Galileo completed successfully the JOI manoeuvre that placed the S/C on its proper trajectory to tour the Galilean satellites. The Prime mission included 4 encounters of Ganymede, 3 of Europa and 3 of Callisto. The only encounter with Io, was a gravity assist that facilitated the JOI manoeuvre, because the scientists feared that the high radiation environment of Io could affect the S/C. After the prime mission, Galileo started the Galileo Europa Mission (GEM), a two year extension that planned 14 more orbits. The GEM was divided in three phases:

- Europa campaign: To search for an evidence of an ocean in the Galilean moon.
- Jupiter water and Io plasma torus study: To study the storms and wind patterns of Jupiter's atmosphere and the toroidal cloud of plasma that orbits the gas giant.
- Io campaign: Given the successful Prime mission, some close encounters with Io were planned.

After the GEM, the mission was extended one more time and the Galileo Millenium Mission (GMM) was born. The GMM provided additional observations of the Galilean satellites and Amalthea. Given the amount of radiation received during the GEM, Galileo's instruments were not fully operative in the course of the GMM. Finally, the S/C plunged into Jupiter the 21st of September of 2003.

1.2.1 Galileo spacecraft

Galileo, that took its name from the Italian astronomer Galileo Galilei, who discovered the Jupiter satellite system, was the first S/C that had a dual-spin attitude stabilization system configuration.

Given that Galileo did not have reaction wheels the attitude was controlled using only a set of 10 N thrusters.

The S/C, powered by two radioisotope thermoelectric generators (RTG), held eleven subsystems and nine scientific instruments on the orbiter:

- Photo-Polarimeter Radiometer (PPR): Analysed the radiant thermal energies emitted by Jupiter.
- Near-Infrared Mapping Spectrometer (NIMS): Determined the Jovian and the satellite chemical compositions.
- Solid State Imaging Camera (SSI): It formed part of the orbiter remote sensing equipment. It was the main imaging device.
- Ultraviolet Spectrometer/ Extreme Ultraviolet Spectrometer (UVS/EUV): It had three main scopes: locate and analyse the clouds of Jupiter; Study Jupiter's high atmosphere and the surrounding ionized regions; Look for satellite atmospheres.
- Energetic Particles Detector (EDP): This instrument determined the angular distributions, temporal fluctuations, intensities and compositions of energetic charged particles in Jupiter's magnetosphere.
- Dust Detector Subsystem (DDS): It had the objective of measuring the mass and speed of the Jovian dust.
- Plasma detector (PLS): This instrument aimed to measure densities, temperatures, bulk velocities and composition of low-energy plasmas.

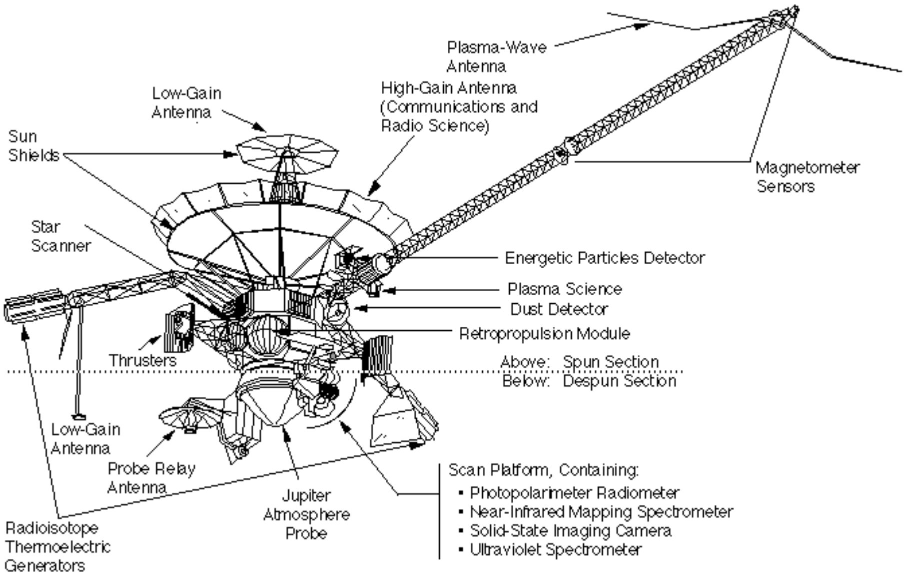

Figure 1.1 – Schematic diagram showing the Galileo S/C.

- Plasma Wave Subsystem (PWS): The main objective was to detect the intensity of the plasma waves in the Jovian magnetosphere.
- Magnetometer (MAG): It had the objective of measure the magnetic field of Jupiter and the Galilean satellites.
- HIC: Heavy Ion Counter.
- Radio Science Subsystem (RSS): Employed the telecommunications and radio-science subsystem to perform gravity measurements and relativity experiments.

A collected, and more detailed, treatment of the different scientific instruments and their objectives can be found in [68].

The S/C was formed by two main sections; a spinning section and a scan platform (despun section). A schematic diagram of the Galileo S/C is represented in figure 1.1.

The rotor of the Galileo S/C spun at 3 rpm and carried the HGA, the propulsion module, the flight computers and most of the support subsystems. Attached to the rotors were two booms, the shortest held the EDP, DDS, HIC and PLS instruments, while the longest (11 m) held the MAG and the PWS. Finally, the rotor hold the EUV.

The scanning platform, maintained a stable orientation in space an contained the remote sensing experiments like the PPR, the NIMS, the SSI the UVS and the atmospheric probe. More information about the S/C configuration can be found in [27].

Galileo RSS, was constructed around two transponders capable to receive and transmit frequencies at S (2.3 GHz) and X-Band (8.4 GHz). The RSS was designed to support the following link configurations : S/S, X/X, S/X, (in two-way configuration) and S (only one-way in downlink).

The spacecraft transmitted frequency was controlled either by the spacecraft oscillator, by means of the ultra stable oscillator (USO), by a less-stable crystal oscillator or by the ground-station in the two-way configuration.

The two transponders were designed to be operated by the HGA or by the two LGA's (S-band), but as explained before, due to a problem in the deployment of the HGA, the mission was only able to operate with the S-band, limiting the capabilities and the link configurations to S/S and S.

1.3 The Cassini-Huygens mission

The Cassini-Huygens mission to explore the Saturn system was launched on the 15th of October, 1997. It took its name from the two first astronomers that discovered satellites of Saturn. During its seven years cruise to Saturn, four gravity assists were employed to increase the spacecraft velocity and allowed to reach Saturn. They included two Venus flybys, an Earth flyby and finally a Jupiter flyby. During this last gravity assist, observations of the Jupiter system were taken, together with Galileo. This was the first occasion in which two S/C's took observations of an outer planet at the same time.

The 1st of July, 2004, Cassini performed the SOI setting the beginning of the tour phase scheduled to last for four years. The 23rd of December, 2004, the Huygens lander was released into Titan's atmosphere to acquire data of the biggest satellite of the Saturn system. After 74 orbits around Saturn, the excellent health of the probe together with the exceptional results obtained during these four years granted Cassini three further mission extensions, that carried the mission up to September, 2017. The first was the Equinox Mission, which lasted until 2010, followed by the Solstice Mission until 2016 and finally, by the Grand Finale. The Grand Finale lasted 5 months in which the probe acquired measurements of Saturn and its rings, following highly-eccentric almost-polar orbits. The mission ended the 15th of September, 2017 when the S/C plunged into Saturn.

1.3.1 The Cassini-Huygens spacecraft

The Cassini-Huygens was formed by the Cassini orbiter and the Huygens Titan lander.

The Cassini orbiter was a three-axis stabilized spacecraft equipped with a HGA, two LGA's and powered by three RTG's, that provided electrical power through the decaying of an isotope of Plutonium. The attitude was controlled either using the reaction wheels or a set of small thrusters.

The Cassini-Huygens spacecraft held 18 instruments, 12 of them were on the orbiter. Following [67], we introduce the experiments held on the orbiter:

- Composite Infrared Spectrometer (CIRS): It consists of dual interferometers that measure infra-red emissions to determine the composition and temperatures of atmospheres, rings, and surfaces.

- Imaging Science Subsystem (ISS): The instrument consisted in a wide angle camera and a narrow angle camera.

- Ultraviolet Imaging Spectrograph (UVIS): The instrument measured the views in ultraviolet spectrum.

- Visual and Infrared Mapping Spectrometer (VIMS): The instrument consisted in spectrometers observing visual and infra-red spectra.

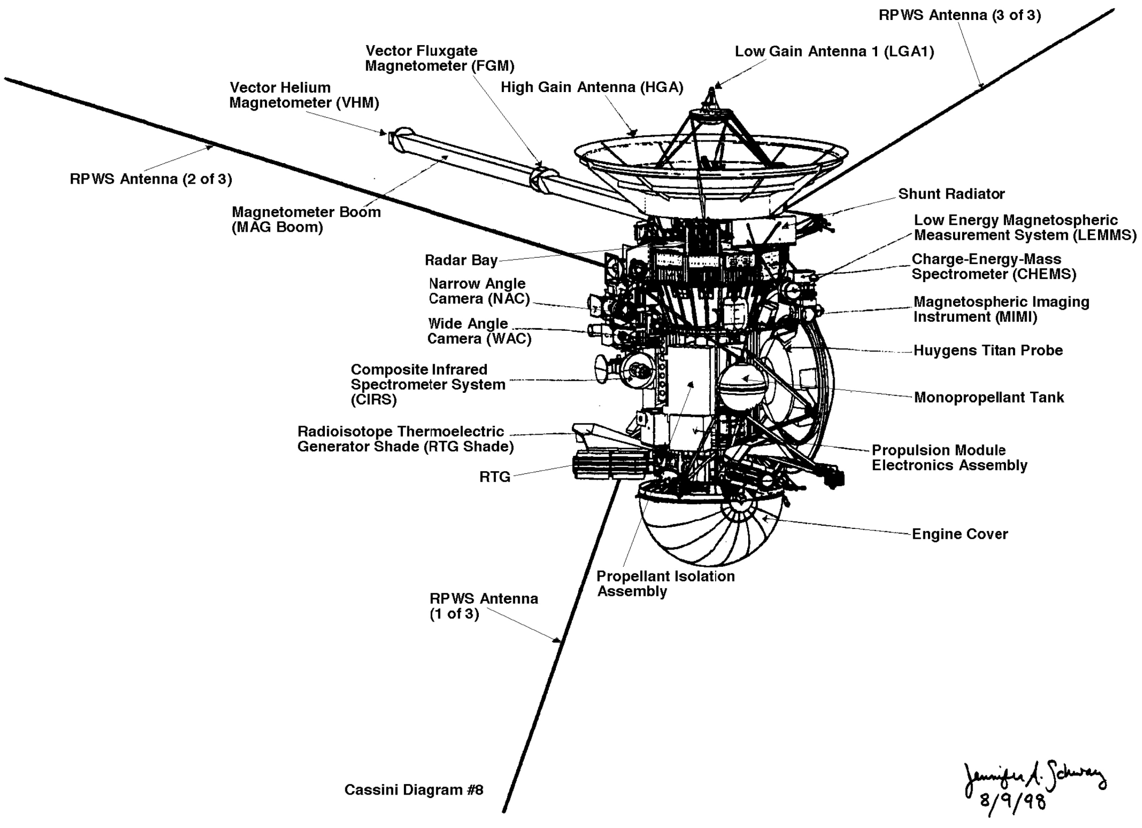

Figure 1.2 – Schematic diagram showing the Cassini-Huygens S/C [1].

- Cassini Plasma Spectrometer (CAPS): Measured the flux of ions and electrons.
- Cosmic Dust Analyzer (CDA): The instrument measured directly the physical properties of the particles in the Saturn system.
- Ion and Natural Mass Spectrometer (INMS): It measured the composition of neutral and charged particles in Saturn system through mass spectroscopy.
- Dual Technique Magnetometer (MAG): It measured the Saturn magnetic field, its variation with time and interactions with the solar wind.
- Magnetospheric Imaging Instrument (MIMI): It measured the composition, charge state and energy distribution of energetic ions and electrons of the Saturn's magnetosphere.
- Radio and Plasma Wave Science (RPWS): It measured the electric and magnetic fields and electron density in the Saturn system.
- Radar (RADAR): It used the HGA to study the surface composition and properties of bodies of the Saturn's system. In particular it allowed to study the surface of Titan, which is covered by a thick atmosphere layer, opaque in the visible spectrum.
- Radio Science Subsystem (RSS): It studied the compositions of Saturn and Titan atmospheres and ionosphere, the rings structure and the gravity field of Saturn and its satellites.

The orbiter instruments were body-fixed, therefore, pointing-turns were required to acquire observations. For this reason, during the scientific observations the HGA could not be used to communicate to the Earth, either for transmit the telemetry or for gravity radio science experiments. Figure 1.2 shows an schematic representation of the S/C.

The main elements of the Cassini RSS were the S-band transmitter, the USO, that provided an on-board highly stable frequency but failed in 2011, the deep space transponders (DST's) and the Ka-band Transponder (KaT), that was designed to support general relativity tests and failed before the SOI. With them, the RSS was designed to support the following link-configurations : X/X, X/Ka, Ka/Ka, S, X and Ka.

Due to the problem with the KaT, the two-way radio-link configurations were limited to X/X and X/Ka, preventing the complete calibration of the dispersive media [20], [66].

1.4 The Juno mission

Juno was launched the 5th of June, 2011 as a part of the NASA New Frontiers program. After an Earth-flyby, reached the Jupiter system the 5th of July, 2015, being the second spacecraft that performed a JOI manoeuvre. The S/C was set to complete 33 orbits with a 11-day orbit, but afterwards, the Juno team decided to change its orbital plan to a 14-day orbit to simplify the navigation. Due to a problem with a valve of the propulsion system, the probe was left in a 53.5-day orbit. This larger period will not prevent the mission to reach the science objectives.

The main objective of Juno is to unveil the interior structure of Jupiter, its origin and evolution by means of the gravity measurements, observations of the magnetic field and the atmosphere dynamics. This is the reason why the Juno spacecraft took its name from the Roman mythology, being Juno the goddess that unveiled the true nature of Jupiter.

1.4.1 The Juno spacecraft

Juno is a spin-stabilized S/C that nominally spins at 30 rpm. Powered by three large deployable solar panels and high energy density Li batteries. Attitude control thrusters are used for re-orienting the spin axis, for smaller trajectory/orbit corrections, and spin-up/down manoeuvres.

The Juno S/C holds nine different scientific instruments:

- Gravity Science: The very first objective of the Gravity Science experiment is to determine the structure of the gas giant by means of gravity measurements. The experiment uses the telecommunications subsystem to determine the precise relative position of the S/C with respect to Jupiter.
- Magnetometer (MAG): It has as objectives the determination of the dynamics that rule Jupiter's interior, mapping its magnetic field, and the determination of the three-dimensional structure of the polar magnetosphere.
- Microwave Radiometer (MWR): It has the objective of measuring the thermal emissions of the gas giant.
- Energic-particles (JEDI): The Jupiter Energetic-particle Detector Instrument will measure the energy and angular distribution of Hydrogen, Helium, Oxygen, Sulphur and other ions of the polar magnetosphere.
- Plasma (JADE): The Jovian Auroral Distributions Experiment aims to resolve the Jovian aurora plasma structure.
- Plasma Waves (Waves): The instrument will measure the radio and plasma spectra of the aurora.
- Ultraviolet (UVS): Will detect the ultraviolet emissions of the polar magnetosphere.
- JunoCam: The first 3-color images of Jupiter were provided by this instrument.
- Infrared Imager / Spectrometer (JIRAM): Its primary goal is to probe the upper layers of Jupiter's atmosphere.

Figure 1.3 evidences the position of the instruments in the Juno orbiter. A more detailed explanation of the instruments of the Juno S/C can be found in [23].

The gravity experiment is constructed around the on-board KaT, that provides coherent two-way measurements in Ka-Band (Ka/Ka). The Ka/Ka link is less affected by the dispersive noises than the X/X.

The redundant DST, used for navigation, supports coherent two-way Doppler measurements in the following configurations X/X and X/Ka. However the triple radio link (X/X, X/Ka and Ka/Ka) is not available.

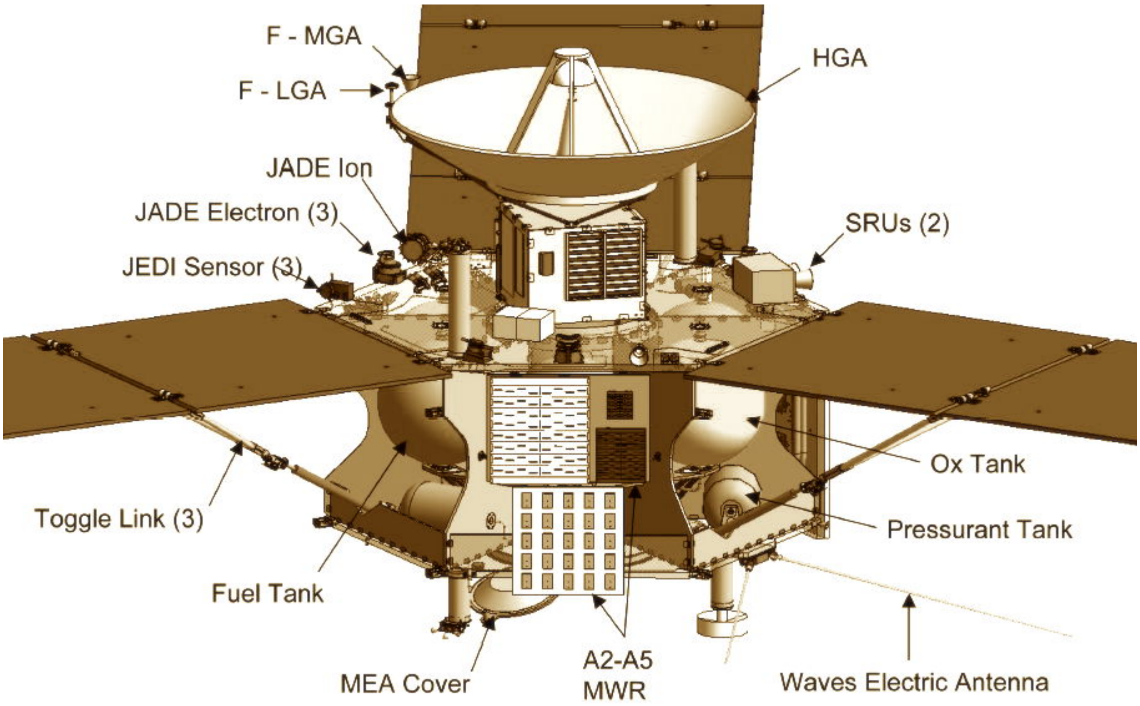

Figure 1.3 – Schematic diagram showing the Juno S/C.

Chapter 2

The orbit determination problem

Contents

2.1 Introduction

The gravity science experiments are experiments that aim at shedding some light and providing constraints on the models of the interior structure of celestial bodies. The gravity science is a particular application of the orbit determination (OD). This chapter will introduce the mathematical formulation of the OD, together with the main observations used in the OD process and the main error sources that may affect the results. Also, the distinction between local and global approach, that will be used during this dissertation thesis, will be introduced.

2.2 The orbit determination problem

The OD problem is an iterative process that consist in the estimation of a set of parameters that define the trajectory of a body. The core of the process is the comparison between the measured observables and the corresponding computed values obtained by an orbit determination program, using a set of observational and dynamical models. In what follows, we will use the JPL's OD software MONTE (Mission-analysis, Operations and Navigation Tool-kit Environment) [31].

The high-level schema of an OD process is summarised in figure 2.1.

Given an observational and a dynamical model of our system, we integrate the trajectory of our S/C and the celestial bodies studied in this research. Based on the predicted trajectory the computed observables are calculated. The differences between the measured observables and the computed ones form the residuals. In the hypothetical case that the trajectory of the bodies of study and the models that define our system were perfectly known, we would obtain zero-mean white noise residuals. However, errors and

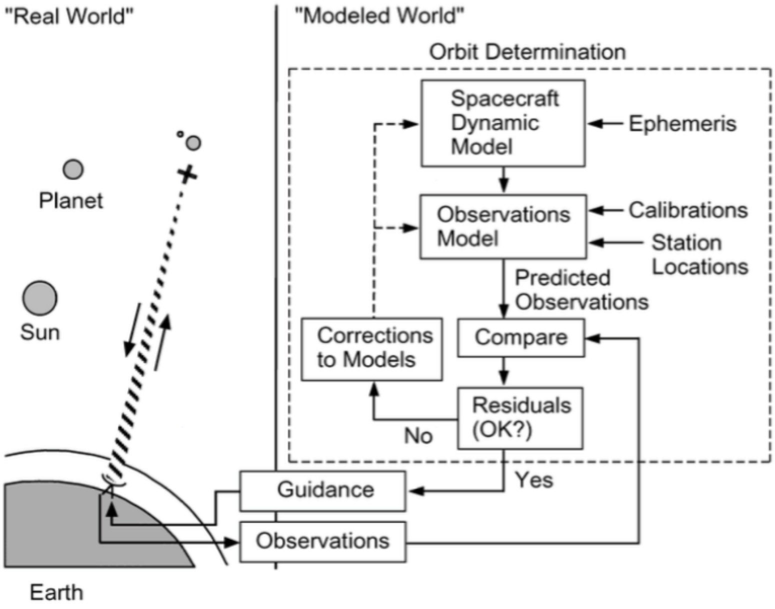

Figure 2.1 – Schematic representation of the OD process [86].

miss-modelling introduce signatures on the residuals that enable adjustments of our state-parameters by means of a batch weighted least squares estimation filter [22], that defines the best solution as the one that minimizes the weighted sum of squares of the residuals. The estimated parameters are, at least, the spacecraft initial state. Other parameters can be the initial state and the gravity field coefficients of the celestial bodies, or more generally, any parameter that may affect the trajectory of the S/C.

Given the non-linearity nature of the OD problem, the iterative corrections to our initial estimate of the solve-for parameters are defined as:

$$\delta x_c = (A^T W A + \tilde{\Lambda})^{-1}(A^T W y + \tilde{\Lambda}\tilde{x}) \tag{2.1}$$

Where δx_c is the least-squares estimate, A represents the matrix of observation partials, W the matrix of observable weights, $\tilde{\Lambda}$ the a-priori information matrix, y the set of measurements and $\tilde{x}$ the a-priori state vector. The first part of the equation 2.1 can be represented as P_x.

$$P_x = (A^T W A + \tilde{\Lambda})^{-1} \tag{2.2}$$

P_x represents the covariance matrix that provides information about the formal accuracy and correlation of the different estimated parameters. Each element of the main diagonal P_{xii} is related to the uncertainty σ_i as:

$$\sqrt{P_{xii}} = \sigma_i \tag{2.3}$$

More details about the mathematical formulation of the statistical orbit determination can be found in the chapter 4 of [82] and chapter 9 of [87].

2.2.1 Observables

An observable is any measured physical quantity that carries information about the solve-for parameters. In deep space navigation, the most used observables are:

- Range: Measured round-trip light time.
- Range-rate or Doppler: The frequency shift of the carrier of the received signal.
- DDOR: Is an angular measurement of the S/C along a baseline formed by two different ground stations.
- Optical observables: Direct measurement of the S/C angular position relative to a target body.

The two main observables used in this work are the range and the range-rate in their two-way radio-link configuration (F2). This choice is done to avoid the error in the stability of the S/C clock in the one-way case (F1) and the inter-station clock delays in the three-way configuration (F3). F3 data will be used in particular occasions, to counterbalance the lack of F2 data during close encounters.

Range observables The range observables are based on the measurement of the propagation time of an electromagnetic wave travelling at the speed of light.

The one-way ranging is based on the transmission of a signal from an emitter to a receiver. In the classical two-way configuration, the ranging is accomplish by means of the modulation of a signal in an uplink, in the ground station. The S/C receiver locks to the carrier, demodulates the signal and modulates it back into a downlink carrier coherent with the uplink. The ground receiver receives a time delayed signal that represents a measure of the round-trip propagation time, being proportional to the sum of the uplink and downlink ranges.

$$\tau = \frac{\rho_u + \rho_d}{c} \tag{2.4}$$

Where ρ_u and ρ_d represents the one-way range, in uplink and downlink respectively, and c is the speed of light.

Range-rate The range-rate observables are a measurement of the Doppler shift of the signal that provide a measure of the relative radial velocity. The signal is transmitted from the ground station at a frequency f_T at a given time, t_1. This frequency, with a given Doppler shift due to the relative motion between the S/C and the ground station, is received at time, t_2, by the probe. Then, the probe transmits a coherent signal with a different frequency, in order to avoid interferences between the up-link signal and the down-link signal. The transmitted frequency is related with the incoming signal by M_2, the turn-around ratio. Finally, the signal is received in a ground-station at t_3.

The received frequency at the ground station, f_R, can be expressed in a simplified way as follows:

$$f_R = (1 - \frac{\dot{\rho}}{c}) f_T \tag{2.5}$$

In practice, the Doppler shift is not measured instantaneously, but by counting the phase change of the Doppler cycle count, that provides a measure of the range-rate during the count-time, T_c. In this way the Doppler observables takes the form of:

$$F = \frac{1}{T_c} \int_{\bar{t}-T_c/2}^{\bar{t}+T_c/2} (1 - \frac{f_R}{f_T}) dt \tag{2.6}$$

Where $\bar{t}$ corresponds to an epoch at the midpoint of T_c.

2.2.2 Noise sources

The accuracy in the OD is limited by a certain number of error sources that may affect the radio-tracking observables. The main sources of error are:

- Instrumental noise - This noise can be caused by random errors introduced in the ground station or in the S/C radio science systems like the DST or the KaT.

- Clock instabilities - Errors in the generation of the reference frequency translate directly into errors in the range-rate measurements. The F2 configuration is used to minimize the clock instability errors that the F1 can induce, or the inter-station clock offset present in the F3 configuration.

- Dynamical miss-modelling - Imperfect non-deterministic and non-gravitational models can introduce errors on the S/C integration and affect the obtained results.

- Transmission media - When a signal propagates through a media, a path delay is induced on the signal. Depending on the properties of the medium, the induced delay can be frequency dependent or not. We talk about dispersive media when the delay depends on the frequency of the signal. Examples of dispersive media are the Earth ionosphere, the Io plasma torus, and the solar plasma. The induced path delay decays with the inverse squared of the frequency. We can correct for the dispersive noise in the signal by means of the multi-frequency link calibrations techniques [66], [20]. Non-dispersive media, is the not frequency-dependent delay, which is mainly caused by the Earth troposphere. There are two main components that can affect the carrier stability: a dry component that provokes large but stable delays and a wet component that instead provoke small but non-stable delays. The tropospheric delays can be compensated with the TSAC (Tracking System Analytical Calibration) and AMC (Advanced Media Calibrations) calibrations.

A more detailed treatment of the different error sources that can interfere in the OD process can be found in [86].

2.3 Multi-arc approach

The gravity field determination, usually, uses data from different flybys that in the best case are separated in time by months. The spacecraft dynamics during this period are difficult to be followed given the complexity of the non-gravitational interactions [70] and the size of the parameter space. Therefore, to overcome the non-deterministic nature of the orbit determination problem, we adopt the multi-arc approach. In this approach, the entire time span of the observations is decomposed in short non-overlapping and non-contiguous intervals, each one with its own set of observables and its initial conditions. This subdivision is useful when you cannot exactly follow the evolution of the dynamics. This method results in over-parametrization, with the additional initial conditions being able to absorb the dynamical model uncertainties. In the multi-arc approach, we make a distinction in the parameters that forms our state vector:

- Global parameters: Those parameters that do not vary in time and affect all the arcs in the same way. As an example, we can consider the spherical harmonics of the gravitational potential of a celestial body.

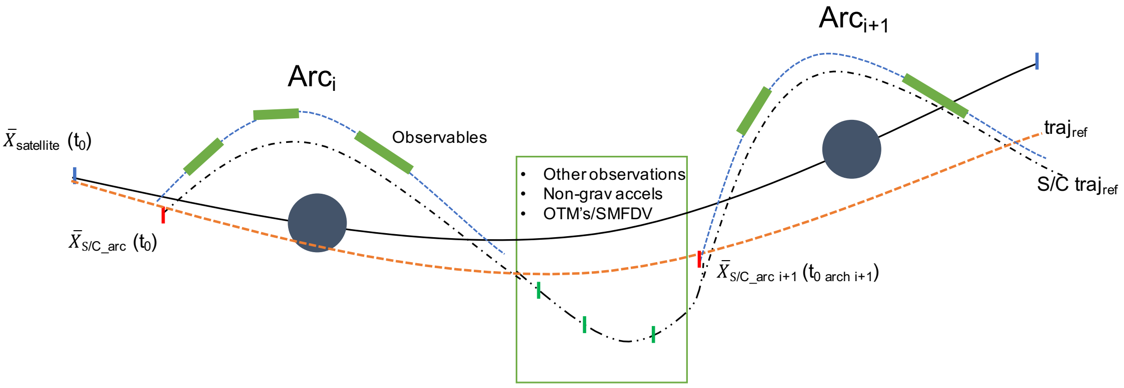

Figure 2.2 – Single-satellite global approach multi-arc strategy.

- Local parameters: Those parameters that only affect a single arc. Theoretically, any parameter can be a local parameter, but in the multi-arc approach, as a rule, the S/C state at the beginning of each arc will be a local parameter, just as if they would be different S/C's.

2.4 Global vs Local strategies

When using the Multi-arc approach, we can do another distinction that will depend on the satellite integration type:

- Single satellite global approach.
- Local approach.
- Global approach.

Single-satellite global approach The single-satellite global approach is the conventional method used in the past for all the analysis of the gravity radio science experiments. Using this approach, when generating new ephemerides, the satellites state is integrated for the entire time span covered by the data arc, from an epoch prior to the first fly-by, to an epoch after the last fly-by (See figure 2.2). This approach ensures that the satellite trajectory is internally coherent [91]. However, following this conventional procedure, a new state of only one satellite is estimated. Usually the a priori covariance matrix of the satellite is diagonal, neglecting the correlations with all the other satellites. Moving the initial state of only one satellite and integrating the equations of motion, the orbits of all the satellites might change, because of the relative gravitational interactions. This could in principle change the fit of all the other data. Hence, the updated ephemerides do not represent an "improved" version of the satellite ephemerides, but the orbits that allows to better fit only the data under analysis. Moreover, the integration of the updated satellite ephemerides over a long time span is a long process, and it slows down the analysis.

During the last five years, the radio science (RS) team and the navigation (NAV) team started experiencing issues to obtain a satisfactory single satellite global fit of all flybys of Titan, Dione, Rhea, and Enceladus. The problem arose when the satellite ephemerides had to be integrated and updated over time scales in the order of 10 years. That, could be an indication of errors in the models or a missing model in the estimation setup interfering in the propagation of the satellites.

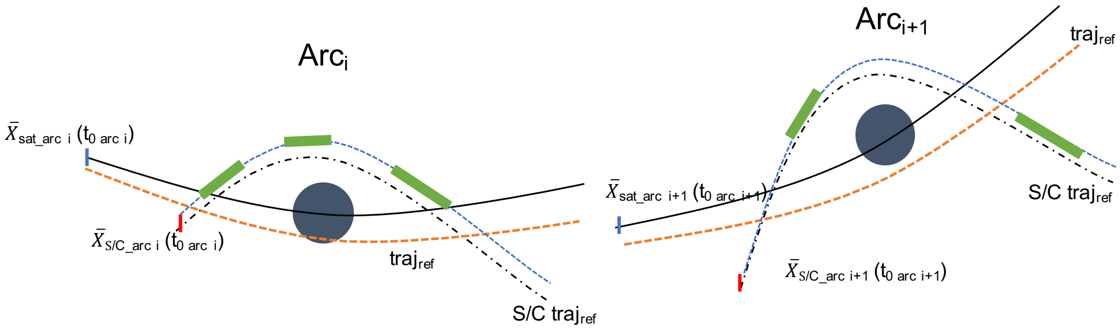

Figure 2.3 – Local approach multi-arc strategy.

This approach has been used during this dissertation thesis to study the gravity field of Titan and its orbital evolution during the timespan of the Cassini mission. See section 4.5.

Local approach The current strategy for the analysis of Cassini gravity science data consists in the multi-arc approach using a local fit. Using this approach, the state of the satellite is treated as a local parameter of a multi-arc analysis, under the hypothesis that the gravity field of a body is weakly correlated to the satellite ephemerides and dynamical properties of its system. Therefore, for each fly-by, not only a different state of the S/C, but also a different state of each body are estimated. After the estimation, new satellite "local" ephemerides are generated for each fly-by, integrating from the new states for a time-span that only covers the corresponding fly-by (See figure 2.3). This approach does not ensure that the satellite trajectory is strictly coherent but, as for the S/C trajectory in the classic multi-arc analysis, the deterministic coherence is replaced by a stochastic coherence. If the differences of the orbits are within the uncertainty of the ephemerides, the two orbits are compatible from a statistical point of view.

For the purpose of the estimation of the satellite gravity field the local approach can be considered fully equivalent to the global approach. This technique is used in section 5.3 to provide updates on the gravity field of the Galilean satellites.

Global approach In this case, all the satellites are integrated during all the time span, taking into account the correlation between all the satellites when fitting the data and using all the forces that influence the satellite dynamics. Therefore, in this case, the ephemerides obtained actually represent a potential improved version of them. Given the size of the parameter space, this approach needs a great amount of observations and is expensive from a computational time point of view. When adding a large amount of measurements, it becomes crucial to weight the data properly in order no mask some mismodelling. This technique is used by the JPL and the IMCCE to generate the ephemerides of satellite systems [49].

During this work, due to the limited number of available observations, we will use the single-satellite global approach (Section 4.5) and the local approach (Section 5.3) to obtain an updated gravity field and improved dynamical models of the bodies involved in the problem.

Chapter 3

Dynamics of the satellite systems

Contents

3.1 Introduction

The satellite systems of Saturn and Jupiter are complex dynamical systems, with several interactions happening between the moons, the rings and the central body, such as orbital resonances, tidal interaction or librations. In this chapter we will expose the theoretical background of the main mechanisms that govern the evolution of the planetary systems.

3.2 Gravitational Potential

Deviations in shape and mass distribution of a celestial body from spherical symmetry manifest themselves in its gravitational field and can provide information about the interior of the body of study. The gravitational potential energy outside of an isolated body, of any internal structure, can be described by means of an integral over the mass distribution, the so called Poisson's integral:

$$U(\vec{r}) = -G \int \frac{1}{|\vec{r} - \vec{r\prime}|} \rho(\vec{r\prime}) dV \tag{3.1}$$

In the particular case of a point mass M equation 3.1 gives the classical result $U = -GM/r$.

Following [56], exterior to a mass distribution, V, it can be shown that the gravitational potential satisfies Laplace's equation:

$$\nabla^2 U(\vec{r}) = 0 \tag{3.2}$$

Using this relation and separating the variables, the potential, U, of an isolated body can be conveniently expanded in series of spherical harmonics of degree l and order m:

$$U(\vec{r}) = -\frac{GM}{r}\Big[1 + \sum_{l\geq 2}\sum_{m=0}^{l}\left(\frac{R}{r}\right)^{l} P_{lm}(\sin\phi)\left(C_{lm}\cos m\lambda + S_{lm}\sin m\lambda\right)\Big] \tag{3.3}$$

Equation 3.3 provides a representation of the gravitational potential energy per unit mass produced by the isolated body.

Where G is the gravitational constant, M and R are the mass and equatorial radius, r is the distance from the body′s center of mass, ϕ is the latitude, λ is the longitude, P_{lm} are the un-normalized associated Legendre functions, C_{lm} and S_{lm} are the un-normalized spherical harmonic coefficients.

We can adopt the normalized harmonics using the following relations:

$$\begin{aligned}
\bar{P}_{lm} &= \sqrt{(2l+1)(2-\delta_{0m})\frac{(l-m)!}{(l+m)!}} = N_{lm}P_{lm} \\
C_{lm} &= N_{lm}\bar{C}_{lm} \\
S_{lm} &= N_{lm}\bar{S}_{lm}
\end{aligned} \tag{3.4}$$

Finally, the gravitational acceleration can be expressed as the gradient of a scalar potential.

$$\vec{a_g} = -\nabla U(\vec{r}) \tag{3.5}$$

3.3 Tidal potential

When introducing a secondary body B of mass M_b placed at $\vec{r_b} = (r_b, \phi_b, \lambda_b)$ in the body-fixed frame, the gravitational potential of the primary body will change due to the tidal perturbation generated by the secondary body. The external perturber will create a tide-raising potential, W, that will change the shape and the mass distribution on the primary, as it, its gravitational potential will be modified as well.

At the surface of the perturbed body, the potential $W(\vec{R}, \vec{r_b})$, can be expanded into a sum of terms $W_l(\vec{R}, \vec{r_b})$, that will be proportional to the normalized Legendre polynomials $P_l cos(\gamma)$. Then, in any point $\vec{R}(R, \phi, \lambda)$ on the surface of the primary the potential W takes the form of:

$$\begin{aligned}
W(\vec{R}, \vec{r_b}) &= \sum_{l=2}^{\infty} W_l(\vec{R}, \vec{r_b}) = -\frac{GM_b}{r_b}\sum_{l=2}^{\infty}\left(\frac{R}{r_b}\right)^{l} P_l cos(\gamma) \\
&= -\frac{GM_b}{r_b}\sum_{l=2}^{\infty}\left(\frac{R}{r_b}\right)^{l}\sum_{m=0}^{l}\frac{(l-m)!}{(l+m)!}(2-\delta_{0m}) \times P_{lm}(sin\phi)P_{lm}(sin\phi_b)cos(m(\lambda-\lambda_b))
\end{aligned} \tag{3.6}$$

Where G is the gravitational potential, γ is the angle between $\vec{R}$ and $\vec{r_b}$, and δ_{0m} the Kronecker delta symbol as explained in [54].

Then, as introduced before, tidal distortion of the primary due to the secondary provides an additional $\Delta U(r)$ to the body's potential in an exterior point $\vec{r}$. Assuming the linear theory, this term can to be shaped by terms of $U_l(\vec{r})$ that are proportional to the terms $W_l(\vec{R}, \vec{r_b})$, that will evolve in time and will have a rich spectrum of frequencies [29].

Due to the Dirichlet boundary condition, each degree l scales with $(R/r)^{l+1}$ and each term $W_l(\vec{R}, \vec{r_b})$, will introduce a linear deformation on the primary's body shape [21]. According to where the proportionality factor is inserted, at the degree level or at both degree and order, two different formalisms can be found in literature.

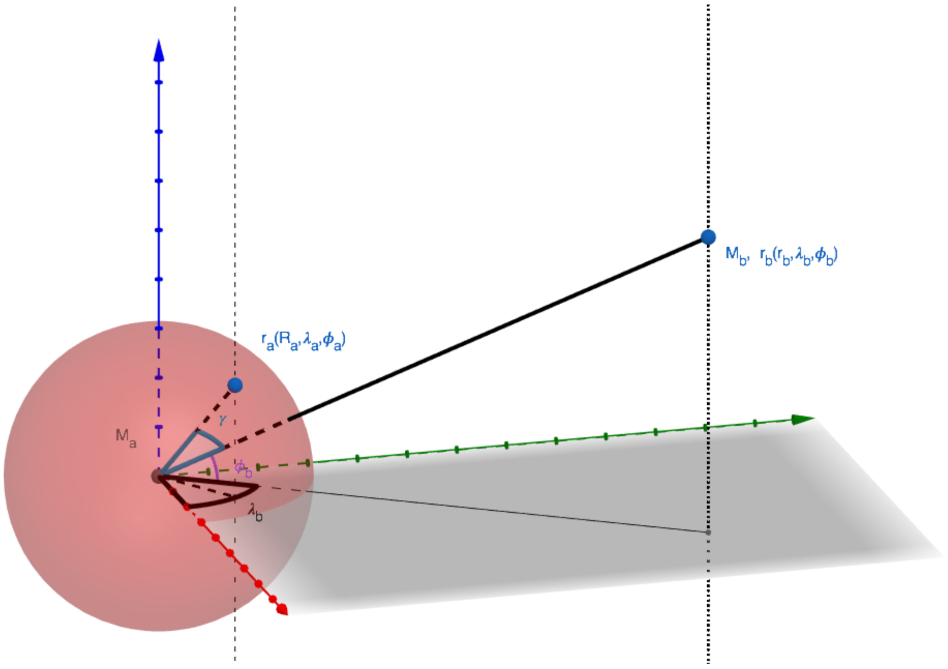

Figure 3.1 – Schematic diagram of the geometry angles. R_a represents a point on the surface of the primary body A, with coordinates $\vec{R} = (R_a, \phi, \lambda)$. The perturber body, B, is identified by $\vec{r_b} = (r_b, \phi_b, \lambda_b)$.

Kaula Formalism (k_l) The proportionality factor is inserted at the degree level, being proportional to the Love number k_l. Then, we can set the total change in the exterior potential as:

$$\begin{aligned}\Delta U(\vec{r}) &= \sum_{l=2}^{\infty} k_l \left(\frac{R}{r}\right)^{l+1} W_l(\vec{R}, \vec{r_b}) \\ &= \frac{GM^*}{r^*} \sum_{l\geq 2} \left(\frac{R}{r}\right)^{l+1} k_l \left(\frac{R}{r^*}\right)^{l} \sum_{m=0}^{l} (2-\delta_{0m}) \frac{(l-m)!}{(l+m)!} \\ &\quad P_{lm}(\sin\phi) P_{lm}(\sin\phi^*)(\cos m\lambda \cos m\lambda^* + \sin m\lambda \sin m\lambda^*)\end{aligned} \tag{3.7}$$

IERS Formalism (k_{lm}) The IERS formalism appears to be different, because it expresses directly the tidal effect as a change in the body spherical harmonics coefficients. The Love numbers are function of both degree and order and the change in the exterior potential takes the form of:

$$\begin{aligned}\Delta U(\vec{r}) = \frac{GM}{r} \sum_{l\geq 2} \sum_{m=0}^{l} \left(\frac{R}{r}\right)^{l} \bar{P}_{lm}(\sin\phi) \bar{P}_{lm}(\sin\phi_b) \\ \frac{k_{lm}}{2l+1} \left(\frac{GM_b}{GM}\right) \left(\frac{R}{r_b}\right)^{l+1} (\cos m\lambda_b + \sin m\lambda_b)\end{aligned} \tag{3.8}$$

Then, using the IERS formalism we can express the deviation on the spherical harmonics as:

$$\begin{aligned}\Delta\bar{C}_{lm} - i\Delta\bar{S}_{lm} &= \frac{k_{lm}}{2l+1}\frac{GM_b}{GM}\left(\frac{R}{r_b}\right)^{l+1}\bar{P}_{lm}(\sin\phi_b)\exp\left(-im\lambda_b\right) \\ &= \frac{k_{lm}}{2l+1}\frac{GM_b}{GM}\left(\frac{R}{r_b}\right)^{l+1}\bar{P}_{lm}(\sin\phi_b)\left(\cos m\lambda_b - \mathrm{i}\sin m\lambda_b\right)\end{aligned} \tag{3.9}$$

When comparing both formalisms, we see that the IERS formulation is an extension of the Kaula's formulation, where k_l it is replaced by k_{lm}. Kaula then, represents a particular case of IERS where k_{lm}=k_l. For example, for the degree 2, Kaula's formulation becomes equivalent to IERS under the assumption of $k_{20} = k_{21} = k_{22} = k_2$. That implies that the linear deformation in the primary body due to the tidal distortion will be the same in every direction.This kind of assumption is convenient for the long term dynamics when you do not want to deal with that many parameters. It also can be useful in short term dynamics if the data set is not really sensitive to the variation of the k_{lm}.

Instead, when considering short term dynamics in Jupiter and Saturn the IERS formulation becomes necessary. Their high rotation rate enhances the differences between the different k_{lm} for a certain l, so we can consider different responses for different degrees and orders.

In the real world, due to the in-elasticity of the celestial bodies, the perturbed body does not react instantaneously to the mass-redistribution caused by the secondary, a lag exists between the tide-raising potential and the tidal induced potential. Then, we can represent the love numbers as a complex number, where the real part $Re(k_{lm})$ represents the part of the potential aligned with the tide-raising potential, the imaginary part $Im(k_{lm})$ is related to this lag and describes the dissipation in the interior of the body.

The dissipation factor or quality factor Q is a dimensionless coefficient that gives an indication of the tidal energy dissipation. For a gas giant, it is expected to be frequency-dependent, with dissipation-peaks at certain frequencies as suggested by [61] with the discovery of Saturn's Q_p at Rhea's frequency. More details will be given in the following sections.

The quality factor is related with the $Im(k_2)$ and to the geometrical lag ϵ by means of:

$$\frac{1}{Q} = \frac{-Im(k_2)}{|k_2|} = tan(2\epsilon) \tag{3.10}$$

Finally, using the IERS form with the complex number notation we generalize the deviation on the spherical harmonics due to the tidal distortion as:

$$\Delta J_n = -\frac{Re(k_{l0})}{2l+1}\sum_j\Big(\frac{GM_b}{GM}\frac{R}{r_b}^{l+1}\bar{P}_{l0}(u_b)\Big) \tag{3.11}$$

$$\Delta C_{lm} - i\Delta S_{lm} = \frac{k_{lm}}{2l+1}\sum_j\Big(\frac{GM_b}{GM}\frac{R}{r_b}^{l+1}\bar{P}_{lm}(u_b)(s-it)^m\Big) \tag{3.12}$$

3.3.1 Hydrostatic equilibrium

If we consider that a perfectly fluid body is not subjected to secular stresses, its shape could be described, uniquely, by the spherical harmonics of the second degree, forming an equipotential surface defined by the gravity of the body, its rotation and the tidal distortion caused by the primary. This means that the deviations from the spherical symmetry are only caused by the rotation of the body and the tidal distortion. Then, we can introduce k_f, the fluid Love number, that describes the complete relaxation of a body in long time-scales adjusting to the tidal and rotational potentials [42].

Hence, the degree-2 gravity coefficients J_2 and C_{22} assume the following expressions:

$$J_2 = \frac{5}{6} k_f \frac{w^2 R^3}{GM} \tag{3.13}$$

$$C_{22} = \frac{1}{4} k_f \frac{w^2 R^3}{GM} \tag{3.14}$$

Where w is the rotational period. One way to evaluate the hydrostaticity of a body, by means of the gravity measurements, is to measure the ratio J_2/C_{22}. The expected value for a slow-rotating body is 10/3, that corresponds to the ratio between the equations 3.13 and 3.14.

If the body of study is in hydrostatic equilibrium, its moments of inertia will be related to the C_{22} through k_f.

The moment of inertia of an hydrostatic body can be inferred by means of the Darwin-Radau equation, [55]:

$$\frac{C}{MR^2} = \frac{2}{3}\Big[1 - \frac{2}{5}\Big(\frac{4 - k_f}{1 + k_f}\Big)^{1/2}\Big] \tag{3.15}$$

Also, J_2 and C_{22} coefficients can be expressed in terms of the inertia moments [21]:

$$\begin{aligned} J_2 &= \frac{C - A}{MR^2} \\ C_{22} &= \frac{B - A}{4MR^2} \end{aligned} \tag{3.16}$$

3.3.2 Tidal heating

The tidal interaction is known to be one of the main drivers of the planetary systems evolution. The major satellites of both Jupiter and Saturn gas giant systems are in a synchronous state, that means that the satellite's rotation period around its central body is the same as its spin period. Due to the gravitational pull of the primary, a bulge pointing along the line that connects the centres of the satellite and the planet raises on the satellite.

The height of the bulge created by the gravitational pull, depends on the semi-major axis of the orbit and the resistance that the satellite present against the raising and lowering of its own bulge. Given an orbit with eccentricity, this cyclic process results in tidal heating that progressively circularizes the satellite's orbit [73]. As a consequence of the progressive circularization of the orbit, the tidal heating is reduced, until after a certain time the satellite will follow a circular orbit without tidal heating.

In an alternative case, in which the motion of the satellite is perturbed by a mean motion resonance, its eccentricity would rise counteracting the tidal eccentricity damping and the tidal de-heating.

The rate of dissipation in the spin orbit satellite is related to the internal properties by means of [79]:

$$\dot{E} = \frac{21}{2} Im(k_2) \frac{R_e^5 G M^2 n}{a^6} e^2 \tag{3.17}$$

Where G is the gravitational constant, M is the mass of the planet, n is the mean motion, a is the semi-major axis and $Im(k_2)$, commonly characterized as $-k_2/Q$, describes how is the response of the interior of the satellite to the applied potential. The $Im(k_2)$ is is a way of cloaking our ignorance on interior processes and depends on how the mechanical energy is dissipated into heat [75].

3.3.3 Orbital evolution

The long-scale orbital evolution is dominated by the antagonist effects of the dissipation on the central body and on the different satellites that orbit around it. While tidal heating tends to circularize the orbit, the dissipation on the primary results in torques that push the satellite outward, at the same time, its rotation rate is reduced to keep the angular momentum of the system constant.

As introduced before, the gravitational pull of a satellite orbiting a primary will create a tidal bulge on the central body. This bulge, due to the in-elasticity of the body, will not point directly towards the satellite, a lag between the created bulge and the tidal generating potential will exist. This lag between the raising potential and the tidal bulge will cause torques on the satellite and will depend on the dissipation of the primary, taking the following form:

$$T = \frac{3}{2}\frac{Gm^2R_p^5k_{2p}}{a^6Q_p} \tag{3.18}$$

A large lag angle implies a small quality factor, Q_p, high dissipation rates on the primary and hence stronger torques that will make the satellite migrate faster.

If the rotation rate of the primary is greater than the mean motion of a satellite, that is for satellites beyond the co-rotation point, the tidal bulge will be carried ahead of the satellite creating torques that will cause the satellite to drift away, increasing its semi-major axis while the rotation-rate of the planet will decrease to conserve the total angular momentum of the system [73]. This situations is encountered for the most of the Saturn and Jupiter satellites.

In the opposite case, when the mean motion of the satellite is greater than the rotation-rate of the planet, the bulge lags behind the satellite causing an inward motion of the satellite. This situation is encountered in the Martian system, in which Phobos is moving inward toward Mars.

We can define a characteristic time-scale to describe the outward migration of a moon due to the tidal energy dissipation.

$$t_{tide} = \frac{a}{\dot{a}} \tag{3.19}$$

Then, the effect of the tidal dissipation in the primary at a certain frequency can be expressed as:

$$Q_p = 3k_2\frac{M_m}{M_p}(\frac{R_p}{a_m})^5 n t_{tide} \tag{3.20}$$

Combining 3.20 and 3.19 we arrive to the following formula, that defines the instantaneous outward evolution of a satellite:

$$\frac{\dot{a}}{a} = \frac{3k_2}{Q_p}\frac{M_m}{M_p}(\frac{R_p}{a_m})^5 n \tag{3.21}$$

The torques 3.18 are a strong function of a, the semi-major axis. Assuming a constant k_2/Q ratio, the inner moons migrate faster than the outer moons. Then, due to this outward orbital migration, the satellites may have encountered certain orbits or locations, in which the ratio of two different orbital frequencies would be an integer. This kind of situation is a mean motion resonance (MMR) and is the case of Tethys and Mimas, Dione and Enceladus or Titan and Hyperion in the Saturn system, or Io-Europa-Ganymede in

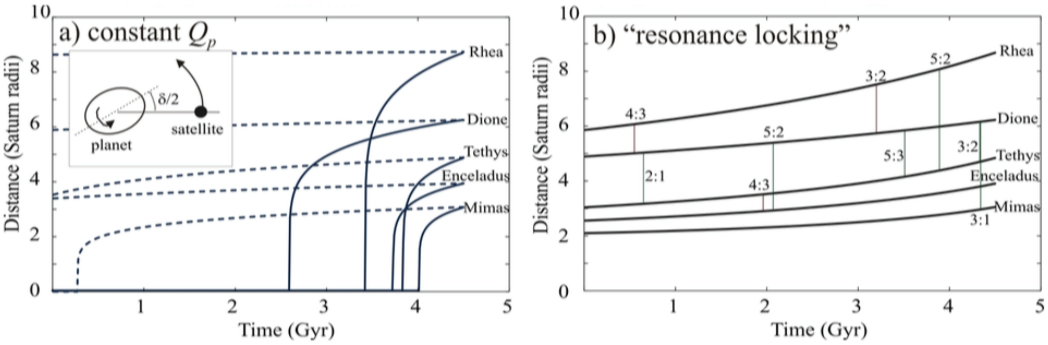

Figure 3.2 – Outward migration of Mimas, Enceladus, Tethys, Dione and Rhea for different cases. a) Outward migration using the classical tidal theory considering a constant $Q_p = 16000$ (dashed lines) against the expected outward migration using the recent Q_p estimated values [61] (solid lines). b) Outward migration under the resonance-locking mechanism [33] using the values estimated using astrometric measurements. This figure has been taken from [75].

the Jovian system. This kind of resonance perturbs the orbits making the eccentricities of the satellites grow and as a consequence, boosting the tidal heating.

These resonances provide a way to excite orbital eccentricities creating a long term heat source. It exists a particular case in which there is an equilibrium eccentricity value when the eccentricity excitation due to the MMR and the eccentricity damping due to the tidal heating counteract their effect. When this situation is encountered, the total rate of dissipation in the satellites is then independent of the satellite structure and only depends on the rate of dissipation in the primary.

Recently, using astrometric observables, measurements of the dissipation of Jupiter and Saturn at different satellite frequencies has been retrieved, [60], [62], [61]. For the Saturn system, this studies confirmed a Q_p compatible with 2000 for Enceladus, Tethys and Dione. Rhea instead, presented a completely different value, 300, not compatible with the other values and evidencing the frequency-dependent nature of the quality factor Q_p. The retrieved values lead to an important consequence: if we consider Q_p constant, the satellites would be younger than the age of the solar system, that is, the moons must have formed billions of years after the formation of Saturn, an incompatible result with the classical formation theory, in which the satellites were formed from the same protoplanetary disk.

This result is evidenced in the first sub-plot of the figure 3.2, retrieved from [75]. The figure shows, using dashed-lines, the outward evolution of the different Saturnian satellites, considering a constant Q_p of 16000 for all the satellites and, in solid-lines, the outward evolution considering as Q_p the retrieved values from [61].

These obtained Q_p values at different frequencies are in agreement with [26] that proposes that Mimas, Enceladus, Tethys, Dione and Rhea may have been formed with the debris of a primitive massive ring. This different formation theory actually places the moons in its current positions.

3.3.4 Resonance locking

An alternative explanation has been proposed in [33]. The theory proposes that Q_p is frequency dependent and not constant in time, being controlled by the evolution time-scale of Saturn's interior. That means that the low Q_p retrieved values do not imply young satellites. The second sub-plot of figure 3.2 shows the hypothetical outward evolution of the Saturn satellites under the resonance-locking mechanism using the present-day Q_p obtained from [61].

The resonance locking mechanism works as follows: during a resonance lock, the outward migration is reinforced by the resonance between the moon's tidal forcing and an oscillation mode. This oscillation mode can be a gravitational mode or an inertial wave.

Due to the internal structure evolution of the primary, the frequency of the mode changes. When the frequency of the mode crosses one of the tidal forcing frequencies, the moons can enter in a resonance and migrate to a rate comparable to the planetary evolution time-scale. When the frequency is approaching the tidal forcing frequency, dissipation in the primary enhances the torque on the satellite, as evidenced in equation 3.18, provoking an outward migration. This outward migration moves the satellite away from the frequency of the mode, therefore the outward migration is reduced, until the dissipation peak catches the tidal forcing again. In other words, the moons can "surf" the dissipation frequency peaks.

It is noteworthy that the resonance locking mechanism may provide a way to explain the values obtained with astrometry, while keeping the old moon formation scenario as a possibility.

Chapter 4

Saturn system data analysis

Contents

4.1 Introduction

The Saturn system is a complex dynamical system. The satellites, the central body and the rings, interact between them by means of the gravitational forces giving raise to interesting phenomena like the MMR of the Saturn system 1:2 Dione-Enceladus, 2:4 Tethys-Mimas or the 3:4 Hyperion-Titan.

Cassini is the only S/C that so far performed a SOI and for 13 years studied the Saturn system in-situ, performing 293 orbits around Saturn, most of them dedicated to the study of the satellites of the system, especially Titan and Enceladus. During the last year of its operational life, Cassini orbited Saturn in a highly eccentric low-pericenter orbit with a period of 6.4 days that allowed to measure the gravity coefficients of the gas giant to an unprecedented accuracy.

This chapter will be dedicated to the data-analysis procedure followed to retrieve the gravity field of Saturn and its biggest satellite Titan. In addition, the chapter will focus on the study of Titan's orbital evolution using the single-satellite global approach introduced in the section 2.4.

4.2 Dynamical Model - Cassini data analysis

This section introduces the dynamical model used in our studies, both the measurement of the gravity field of Saturn and the study of the orbital evolution and the gravity of Titan, that we will describe in section 4.4 and 4.5.

The dynamical model that we used in our study included all the forces that acted on both the Saturn system bodies and the Cassini spacecraft: gravitational forces, that affect the propagation of all the bodies in the solar system and non gravitational forces that only affect the motion of the S/C. Mathematical details of the implementation of these models in MONTE can be found in [30], [72] and [71].

4.2.1 Gravitational accelerations

The Cassini dynamical model used in this study included the gravitational forces of all the main bodies of the solar system, the sun, planets of the solar system, Saturn satellites and the rings of Saturn. In particular, the following effects were activated:

- Relativistic point-mass gravity acceleration from the Sun, the planets, the Moon and Pluto. The state vectors were obtained from JPL planetary ephemerides DE435.
- Relativistic point-mass gravity acceleration from Saturn. The state vector was obtained from JPL's Saturn ephemerides SAT389.
- Relativistic point-mass gravity acceleration from the Saturn's satellites Mimas, Enceladus, Tethys, Dione, Rhea, Titan, Hyperion, Iapetus, Phoebe and Helene. The state vectors were obtained from the SAT389.
- The gravity field of Saturn and its planetary rings, represented by the standard spherical harmonic expansion of its gravitational potential up to the tenth degree retrieved from the JPL saturn system ephemerides SAT389.
- The gravity field of the main Saturn satellites, represented by means of the spherical harmonic expansion, retrieved from the last publications of the RS team.
- Tides risen on Saturn by its satellites.
- Tides risen on Titan by Saturn.
- The self-oblateness of Saturn's satellites, that is the acceleration on a body due to its own deviations from the spherical symmetry.

In addition, the effect of Saturn's large oblateness (J_2), was taken into account when computing the Doppler observables.

Rotational models The major satellites of Saturn are supposed to be in synchronous rotation around its central body, with its rotation axis normal to the orbital plane and prime meridian always oriented towards the empty focus. For that reason, we adopted a dynamically defined, perfectly synchronous, rotational model pointing to the empty focus of the orbit.

For Saturn we used the rotational model of the ephemerides set SAT389, that is defined as:

$$\alpha(deg) = 40.582523383744423 - 0.03099714786916873T \tag{4.1}$$

$$\delta(deg) = 83.537769990273958 - 0.007584170141686378T \tag{4.2}$$

$$W(deg) = 38.8999 + 810.79390237033704d \tag{4.3}$$

Where:

- α: right ascension of the north pole with respect to EME2000.
- δ: declination of the north pole with respect to EME2000.
- W: angle measured easterly along the body's equator between the prime meridian and the ascending line of nodes.
- T: time measured in Julian centuries (36525 days) past J2000.
- d: time measured in days past J2000.

Note that the values are given in double precision, which is sufficient for replication purposes.

The rotation rate term corresponds to $10°39'22''$ and was calculated by the planetary radio astronomy experiment of the Voyager 1 [28].

4.2.2 Non gravitational accelerations

The non-gravitational forces acting on the spacecraft are forces that only affect the propagation of the trajectory of the spacecraft. In our estimation-setup, the following accelerations were active:

- The solar radiation pressure (SRP).
- The acceleration product of the RTG's.
- Orbital trim maneuvers (OTM) used to change the trajectory of the spacecraft.
- Unbalanced thrust during attitude and reaction wheel desaturation manoeuvres implemented with the thrusters (SMFDV).
- Drag caused by Titan's atmosphere.

Instead, other non gravitation accelerations like the albedo and the thermal emission were neglected.

Solar radiation pressure Solar radiation can generate an acceleration above Cassini's sensitivity. The value of these accelerations depends in the S/C geometry and the thermo-optical properties of the surface provided by the NAV team.

Radioisotope thermal generators Three RTG's provided electrical power to the Cassini S/C through the decay of a radioactive isotope of Plutonium. The RTG-induced non isotropic acceleration is modelled using an exponential model:

$$\vec{A(t)} = \vec{A_0} e^{-\beta(t-t_0)} \tag{4.4}$$

Where $\vec{A(t)}$ is the thermal acceleration vector at time t, $\vec{A_0}$, provided by the NAV team, is the spacecraft thermal acceleration vector at a given reference epoch t_0, and β is the time scale of the exponential law, which derives from the 87.7-year half-life of the isotope of Plutonium used as nuclear fuel in the RTG's. The main effect of this acceleration is along the spacecraft Z body-fixed axis.

Orbital manoeuvres and Small Forces Any perturbation that may affect the trajectory of the S/C should be estimated during the orbit determination. To increase the accuracy of our estimation, we avoided, when possible, to introduce OTM or SMFDV in our estimation filter to avoid the introduction of biases in our solution. This was possible in all the flybys but T110 in which two SMFDV were performed before and after the close encounter with the satellite.

Drag We took into account also the effect of the drag in the Cassini S/C, due to the atmosphere of Titan, that perturbed, in a non-negligible way, the motion of the S/C during at least three encounters; T22 (December, 2006), T68 (May, 2010) and T99 (March, 2014).

4.3 Data-Selection and data-calibration

During the different encounters performed by Cassini, range data at X (8.4 GHz) band and Doppler data at X and Ka (32.5 GHz) bands were acquired by the antennas of NASA's Deep Space Network (DSN) at the main complexes of Goldstone, Madrid and Canberra, and in a few occasions by the ESA's ESTRACK complexes in Malargue and New Norcia.

The main observable used in gravity determination is the spacecraft range-rate, which provides a direct measurement of the variation of the radial velocity of the spacecraft. In addition, to study the orbital evolution of the Saturn satellites, we also used range data, that despite its minor contribution to the gravity field determination is really useful to constraint better the ephemerides of the system of study.

During the Cassini-era, the expected accuracy of the Doppler observables using the X-band can be about 0.03 mm/s, while for the ranging systems, limited by the interplanetary plasma and the delays in the ground station and spacecraft electronics, can be about 2 m [86].

The analysis took into account all the data available in a 24 hours window centred around the C/A during the Saturn encounters and 48 hours before and after the C/A during the satellite flybys. The additional data, non acquired during the pericenter, allowed an improvement of the orbit determination, in particular the estimation of ephemerides and the GM of the satellites of Saturn and Saturn itself, due to the stronger constraint that impose on the relative trajectories of the bodies of the problem.

For the most part we used coherent F2 data, compressed to a 60 s integration interval during the satellite flybys. During Saturn encounters we used a different strategy and compressed the data to a 30 s interval in order to retrieve more information, given that the ring occultations caused some data-retrieval issues.

When F2 Doppler was unavailable, situation encountered when the round-trip light-time prevented the tracking station that transmitted the link to receive the coherent link back, we used F3 Doppler, adding in our filter the necessary bias to correct for possible DSN inter-station clock offsets. F1 Doppler was never used due to early failure of Cassini's ultra stable oscillator (USO) and the possible instability of the spacecraft clock due to the environment.

When available, X/Ka was preferred over X/X to be less sensitive to the dispersive effects, like the ionosphere or the solar plasma. We corrected the tracking data for the Earth media effects, the troposphere and the ionosphere, using TSAC, based on a combination of weather data and dual frequency GPS, and AMC calibrations. The last ones were only available during the radio science flybys and were obtained with advanced water vapour radiometers.

Data whose elevation was lower than 15 deg, were cut in order to avoid errors due to inaccurate calibration of the tropospheric and ionospheric induced delays.

An additional effect was included when analysing the data. The S/C on-board transponder measures a frequency of the incoming signal which is shifted since it is in a rotating reference frame. In addition, when the signal is retransmitted back to the Earth, it experiences an additional Doppler shift [65]:

$$\Delta f_{spin} = (s_t + M_2)\frac{w_s}{2\pi} \tag{4.5}$$

Where w_s is the projection along the line of sight of the S/C angular velocity, M_2 is the turn-around ratio, s_t and s_r are coefficients that define the sign of the frequency shift, respectively on transmission and reception. They can only be +1 or -1. Then the sign of the frequency shift depends upon the sign of the spin rate with respect to the sign of the polarization of the signal.

4.4 The gravity field of Saturn - Cassini data analysis

Saturn, predominantly composed by hydrogen and helium, is the sixth planet from the Sun and the second biggest planet of the solar system after Jupiter. It has an oblate shape and its equatorial radius is about 60330 km. The gas giant is in a near 5:2 mean-motion resonance with Jupiter.

Together with its characteristic ring system and its more than 50 moons it gives raise to a really complex planetary system.

This section will explain in detail the process followed to estimate the gravity field of Saturn by means of the trajectory reconstruction of the Cassini probe during six gravity-dedicated orbits during the last months of the deep space mission.

During the Grand Finale phase, Cassini orbited Saturn in a highly eccentric, low-pericenter, 6.4-day orbit. Of the twenty-two proximal orbits, six were dedicated to Saturn's gravity field determination with its pericenter between 2600 and 3300 km over Saturn, passing trough the gap between the inner D-ring and the cloud level of the gas giant.

Doppler measurements were acquired by the DSN, approximately 12 hours before and after the close encounter. During these encounters ring-occultation experiments were also performed. Due to the relative position of Saturn, the Earth and the S/C, the transmitted radio signal crossed the ring-plane producing data gaps. These data gaps were found in the vicinity of the C/A, (approximately 10 minutes gap) and way after, during the so-called distant ring-occultation.

Of the six planned encounters, Rev275, did not have data during the close encounter, due to an acquisition problem at the Malargue complex. Table 4.1 summarizes the main geometrical and data-quality parameters of the six flybys, while figure 4.1 provide a schematic

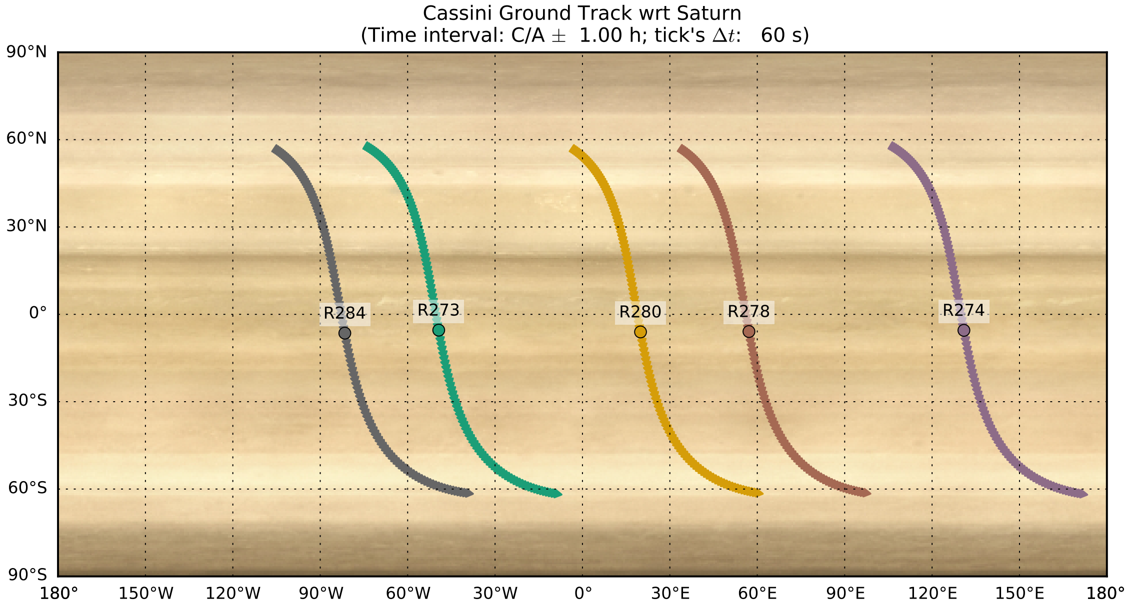

Figure 4.1 – Ground tracks of the six close flybys performed by Cassini over Saturn during the Grand Finale orbits. Note that Rev275 followed practically the same orbit as Rev273.

view of the ground-track of Cassini during the encounters. Note that Rev273 and Rev275 followed a very similar orbit probing almost the same zone of the body.

4.4.1 Multi-arc setup

The acquired radio tracking data of Rev273, Rev274, Rev275, Rev278, Rev280 and Rev284 were pre-processed and the residuals were weighted on a pass-by-pass strategy using the RMS of the residuals itself.

We used a local multi-arc strategy, integrating locally the trajectories of the satellites during the time-span of the arc. Our multi-arc filter solved for:

- State of Cassini at the begining of each arc.
- Cassini RTG's acceleration.
- Saturn GM and zonal harmonics up to 20th degree.
- Saturn non-zonal harmonics up to 2nd degree.
- Saturn $Re(k_{22})$.
- Saturn pole position at J2000.
- B-Ring mass.

Table 4.1 – Main orbital, geometrical and quality data characteristics of the proximal orbits. The values are referred to the C/A.

		R273	**R274**	**R275**	**R278**	**R280**	**R284**
Date (ERT)	(ET)	09-05-17, 06:18	15-05-17, 16:46	22-05-17, 03:15	10-08-17, 12:54	23-06-17, 10:58	19-07-17, 07:55
Altitude	(km)	2658.72	2605.52	2650.00	3355.06	3333.51	2730.60
Relative Velocity	(km/s)	30.65	30.67	30.65	30.38	30.39	30.55
Latitude	(deg)	−5.43	−5.49	−5.54	−5.90	−6.04	−6.45
Longitude	(deg)	−49.33	130.92	−49.07	57.14	19.93	−81.56
SEP Angle	(deg)	142	148	155	175	172	145
Inclination	(deg)	79.69	79.70	79.67	79.66	79.65	79.19
Number of points		1881	1609	1043	1991	2016	1559
RMS	(μm/s)	24	42.3	22.7	41.7	64	65.4
C/A Data		*Y*	*Y*	*N*	*Y*	*Y*	*Y*

- Solar radiation pressure scale factor.
- Station position offsets.

Initial state of Cassini The state vector of the Galileo S/C is estimated at the beginning of each arc, approximately 12 hours prior to the C/A. The a-priori values are obtained from the trajectory, reconstructed by the Cassini navigation team, whose last reconstructed trajectory can be found in the PDS site [19]. We used a conservative approach to set the a-priori uncertainties, using a diagonal covariance matrix with 1-σ of 1000 km in position and 0.001 km/s in velocity.

Cassini's RTG accelerations The a-priori values of the RTG's acceleration were taken from the GINFILE provided by the Cassini navigation team, that contained the values of the thermal acceleration of the S/C at 6-OCT-1997 00:00 ET. As uncertainty, we used the 10% of its value in every direction.

GM of the Saturn barycentre The GM of Saturn's barycentre is retrieved from the SAT389 ephemerides set with a large a-priori uncertainty of 10 km^3/sec^2.

Saturn gravity field coefficients In absence of internal dynamics, the gravity field of a gas giant can be expressed by its even-zonal harmonics. In our setup we included all the zonal harmonics up to the 20th. The quadrupole coefficients ($C_{21}, S_{21}, C_{22}, S_{22}$) were set to zero. They were added to take into account possible deviations between the rotation axis and the principal axis of inertia.

Saturn tidal response The tidal response was set to the values found in [89], and only the real part of the Love number k_{22} was estimated, with a large a-priori uncertainty of 0.8.

Pole position The pole position, right ascension and declination, has been estimated at a reference epoch (J2000), using 0.013 deg as a-priori uncertainty for both terms.

B-Ring mass The rings are assumed to be co-planar with Saturn's equator and to have a constant density. The dynamical model contained the A, B, C-rings and the Cassini division, whose values were retrieved from a presentation of R.A. Jacobson at the Cassini Project Science Group. We considered that the only ring capable to infer a perturbation on Cassini was the ring B whose uncertainty was set to 0.5 km^3/sec^2.

Solar radiation pressure A scale factor of the solar radiation pressure was included as a consider parameter with an uncertainty of the 20% of its value.

Station position offsets In addition, a possible position offset in the ESTRACK stations of Malargue and New Norcia was estimated. We used cylindrical coordinates with an a-priori uncertainty of $3 \cdot 10^{-4}$ km for the cylindrical-radius and the Z direction and $3 \cdot 10^{-6}$ deg in longitude.

4.4.2 Results

We reached a satisfactory single-arc fit estimating the previous parameters. The single-arc solutions are reported in the figure 4.2, showing a great agreement between the estimated even-zonal coefficients and a slightly worse concordance between the odd zonal coefficients.

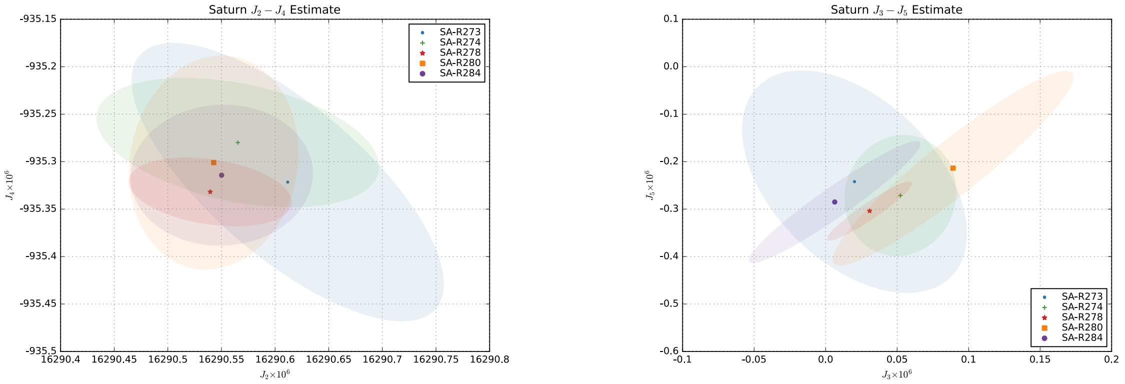

(a) Saturn $J_2 - J_4$ estimate

(b) Saturn $J_3 - J_5$ estimate

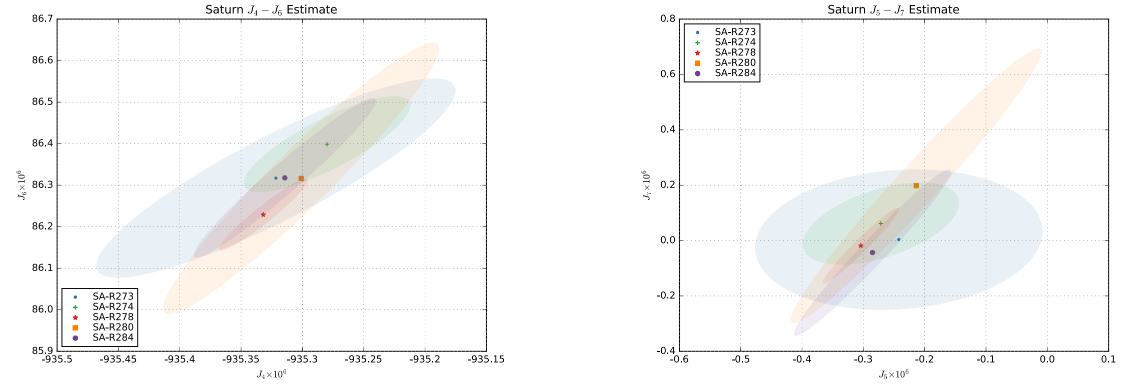

(c) Saturn $J_4 - J_6$ estimate

(d) Saturn $J_5 - J_7$ estimate

Figure 4.2 – Single arc solutions of different pairs of low-degree harmonics, even and odds, with the corresponding 3-σ error ellipses.

When combining the data of all the encounters in a multi-arc fit, we found that the set of parameters was not sufficient to achieve a robust multi-arc solution, finding strong signatures in the vicinity of the C/A. That, lead to the assumption that there was a missing effect on the Cassini dynamical model.

To overcome this problem we followed two different strategies:

- High degree non-zonal field with a new rotation rate (CASE-A).
- Acoustic modes (CASE-B).

High degree non-zonal field with a new rotation rate As a first approach, we found that using a high-degree non-zonal field of 12x12, using the rotation-rate found by Voyager-1 [28], we could fit the data, but such a high-degree field is difficult to be explained for a gas giant.

The interior of a gas giant is almost certainly in hydrostatic equilibrium, making difficult to explain the existence of fluid mountains fixed in the rotating reference frame that could be represented by a high-degree non zonal field.

From a physical point of view, a high-degree non-zonal field can be caused by an irregular longitudinal mass distribution in the deep interior or in the outer shell, if the uneven distribution is caused by the winds.

If we consider strong differential rotation, a high degree non-zonal field is not directly applicable to a planet like Saturn, that is because the winds move at different speed in function of the latitude, so their gravity disturbances cannot be associated to a solid body rotating frame.

Instead, the use of a high-degree non-zonal field becomes valid if the uneven mass distribution is caused by strong-deep convection disturbances that did not change during the Grand Finale orbits.

The non-zonal components of the gravity field induced by the deep-interior disturbances, that is the sectorial and tesseral components, are strictly related to the rotation period of the solid body due to its non-axisymmetric nature. The rotation rate of Saturn is not well known, actually, there are available several estimations of the rotation-rate of Saturn, [41], [28], [38], [35] and [64] spanning from $10°32'45''$, to $10°47'06''$.

Therefore, with the objective of understanding which is the best Saturn's rotation period to associate the non-zonal gravity field, we decided to add the rotation-rate of Saturn as a solve-for parameter of our estimation filter. However, due to the non-linearities of the model, it is not possible to estimate the rotation-rate of Saturn using MONTE. As an alternative procedure we performed multiple estimations using different rotation rates values. To check the quality of the fit we used the sum of squares (SOS) of the residuals, centred in a 4-hour window around the C/A, and the root mean square of the estimated non-zonal field coefficients. We tried all the possible values from $10°27'00''$ to $10°55'00''$ with a $6''$ step. The very same analysis was performed using different gravity field degrees, trying to obtain a proper fit using the lowest non-zonal field degree.

We found that the lowest gravity field degree capable to absorb the signatures around the pericenter was a 7x7 field.

Figure 4.3 evidences the obtained SOS of the residuals normalized with the minimum of all the tested periods, representing a measure of the goodness of the fit. Also, evidences the RMS of the non-zonal field together with the RMS of the non-zonal field sigmas. When the RMS of the field is smaller than the RMS of the sigmas, statistically the non-zonal field is compatible with zero. For clarity, we added the intervals of the different published values using different colors. The normalized SOS profile present different local minima and one clear global-minima. The global minima, minimum-1 in the figure, corresponding to $10°46'58''$, is inside the interval reported in [35] and pretty close to the one reported by [38]. Then, there is a clear local-minima at $10°35'12''$ that is in absolute agreement with the recent value found in [64]. In this case, the RMS of the tesseral field is compatible with zero within 1-σ. It is interesting to notice that, also, [28] seems to lay in a local minima.

Finally, the value published in [41] does not correspond to a local-minima and, moreover, the rotation-rates associated to that interval provided non-convergent solutions in the filter.

For clarity, we also present the different estimated values of the J_2, the B-ring mass and k_{22}, with its associated 3-σ uncertainty, in figures 4.4, 4.5 and 4.6 respectively. Only the best convergent solutions (normalized SOS<1.008) are shown in the figures, together with the retrieved mean, evidencing that in the best convergent solutions, minimum-1 and minimum-2, the obtained values are all compatible within 3-σ.

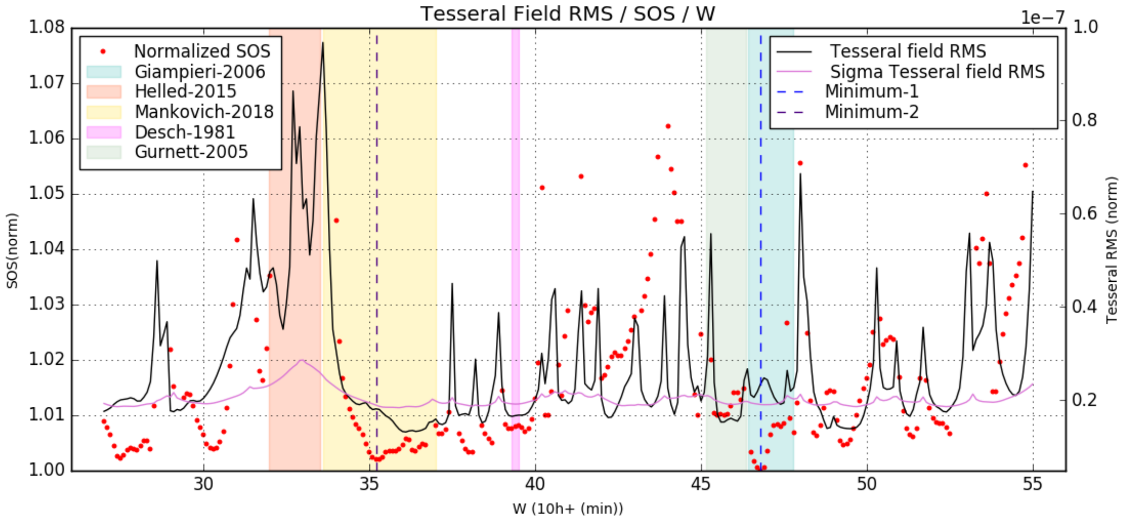

Figure 4.3 – Normalized SOS and corresponding RMS of the non-zonal field and its associated uncertainty for the different solutions retrieved with different rotation rates. The plot evidences four different published values of the rotation-rate of Saturn and the two global-minima obtained.

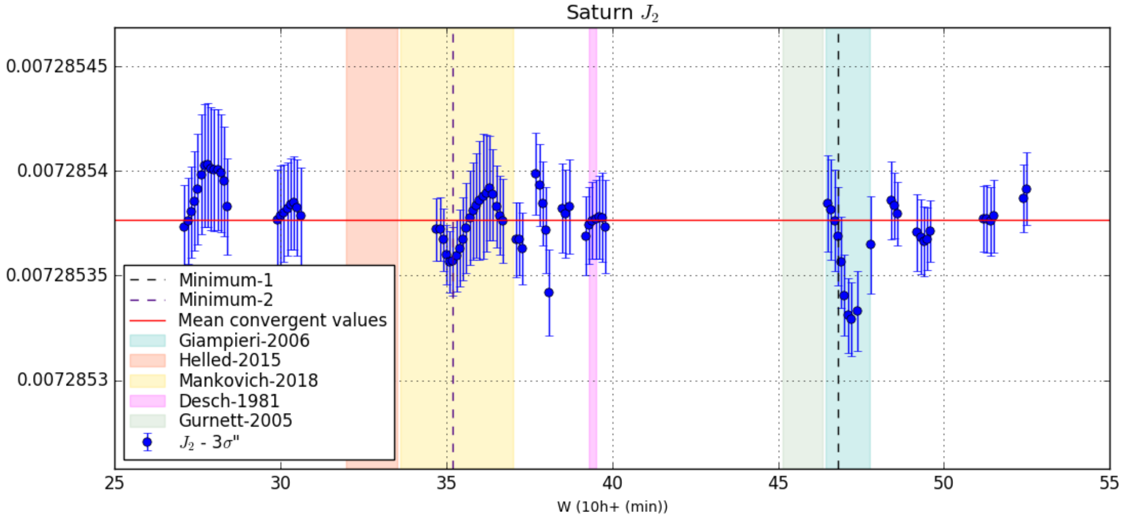

Figure 4.4 – Obtained J_2 of the best solutions (normalized SOS$<$ 1.008) and its corresponding 3-σ, evidencing the values found in the two global-minima.

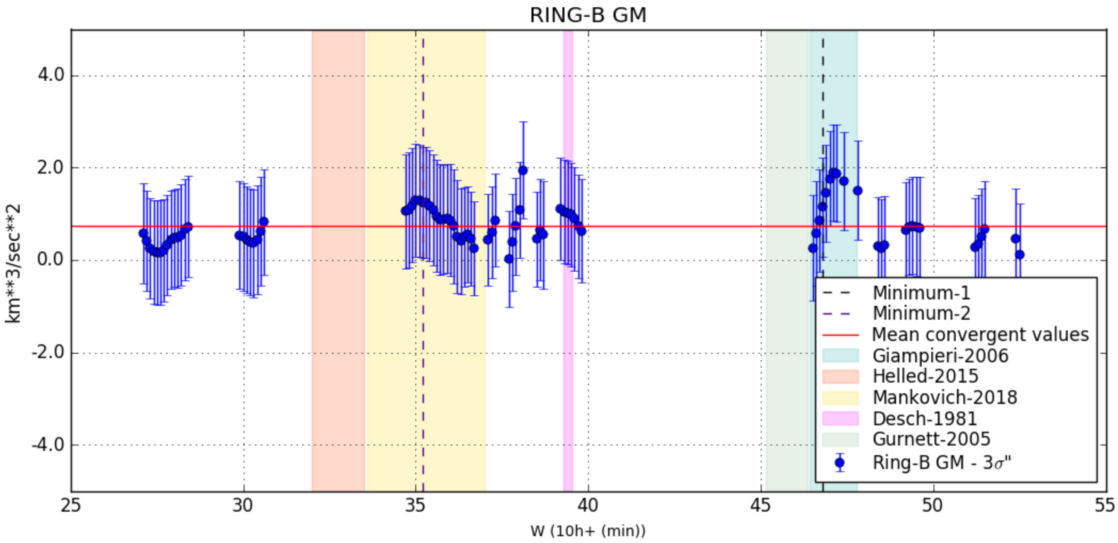

Figure 4.5 – Obtained ring-B GM of the best solutions (normalized SOS$<$ 1.008) and its corresponding 3-σ, evidencing the values found in the two global-minima.

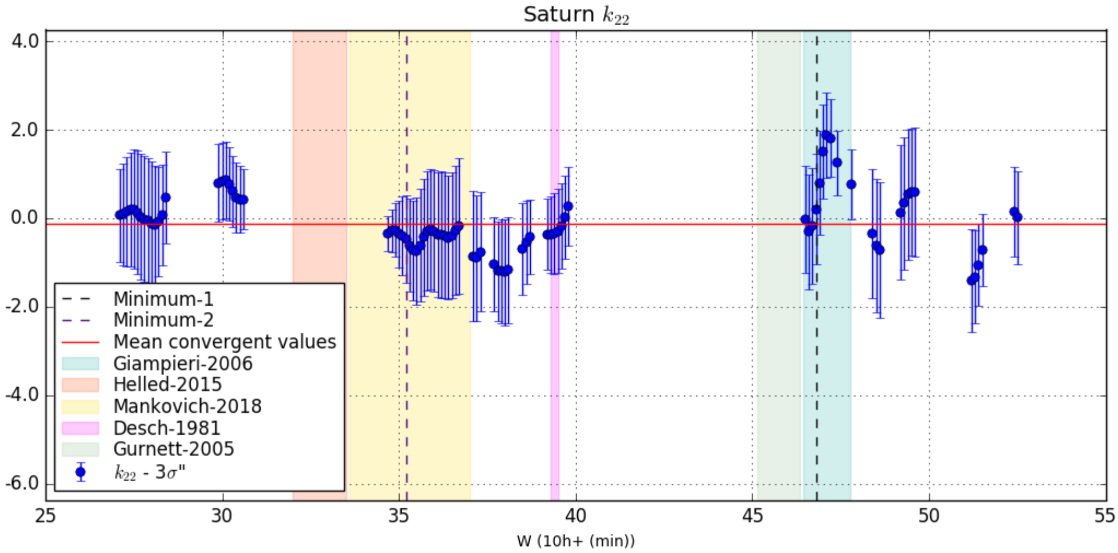

Figure 4.6 – Obtained k_{22} of the best solutions (normalized SOS$<$ 1.008) and its corresponding 3-σ, evidencing the values found in the two global-minima.

The retrieved residuals, of the six arcs used in our analysis, with the rotation rate associated to the minimum-1, are reported in figure 4.7.

We obtained a compatible solution capable to absorb the signatures, (CASE-A), using a lower degree gravity field. Even tough, there are still 50 gravity field coefficients that cannot be explained using a "better" rotation-rate of Saturn. Moreover, appear to be several local-minima which provided similar quality fits, obtaining minor differences between the obtained results, making impossible to draw a definitive conclusion about the real rotation rate of Saturn. Further analyses will be required.

Acoustic modes An alternative assumption was that the residual signatures were caused by acoustic modes. This modes correspond to periodic perturbations in the planet that affect the external gravitational field. However, the inclusion of this time-varying gravity field coefficients in the estimation filter is not straightforward because there are multiple combinations of oscillations capable to fit the data. Moreover, we cannot estimate the frequencies of the different modes due to the non-linearity nature of this model. Then, the choice of the relevant frequencies and the corresponding amplitudes is not unique and the not-continuous amount of data, acquired during the proximal orbits, is not enough to disentangle the relevant modes from the not relevant ones doing a frequency-study, by means of a power spectral density.

In our analysis, we used combinations of different frequencies of the theoretical free oscillation modes, computed by numerical simulations in [36] using the Sa8 interior model. The chosen frequencies correspond to the fundamental and gravitational modes acting on the zonal harmonics of the gravity field. The frequencies used in our analysis are summarized in tables 4.2 and 4.3.

In addition, we used six different fundamental modes measured studying the spiral patterns of Saturn's C-ring, which are created by periodic gravitational perturbations [40]. We considered this fundamental modes to act in the sectorial coefficients of the gravity field (See table 4.4).

Given the chosen frequencies, an additional issue arises: a small error on the frequencies of the modes accumulates over the time, so that, after a few flybys the phase of the oscillation mode could be completely different. To overcome this problem, we decided to treat the included modes as a local parameter of a multi-arc, keeping the amplitude of the estimated mode constant between the different encounters, introducing an over-parametrization that increases the uncertainty of the results but avoiding errors due to inconsistencies.

Table 4.2 – Periods of the fundamental acoustic oscillations acting on the zonal coefficients of Saturn (in min) [36].

	J_2	J_3	J_4	J_5	J_6	J_7	J_8
Period (min)	173.2	131.9	113.0	100.9	92.18	85.44	80.01

We used the following combinations of acoustic modes:

- Fundamental acoustic modes (degree 2 to 6) + Gravitational modes (degree 2 and 3)
- Fundamental acoustic modes (degree 2 to 8)
- Fundamental acoustic modes (degree 2 to 8) + Gravitational modes (degree 2 and 3)

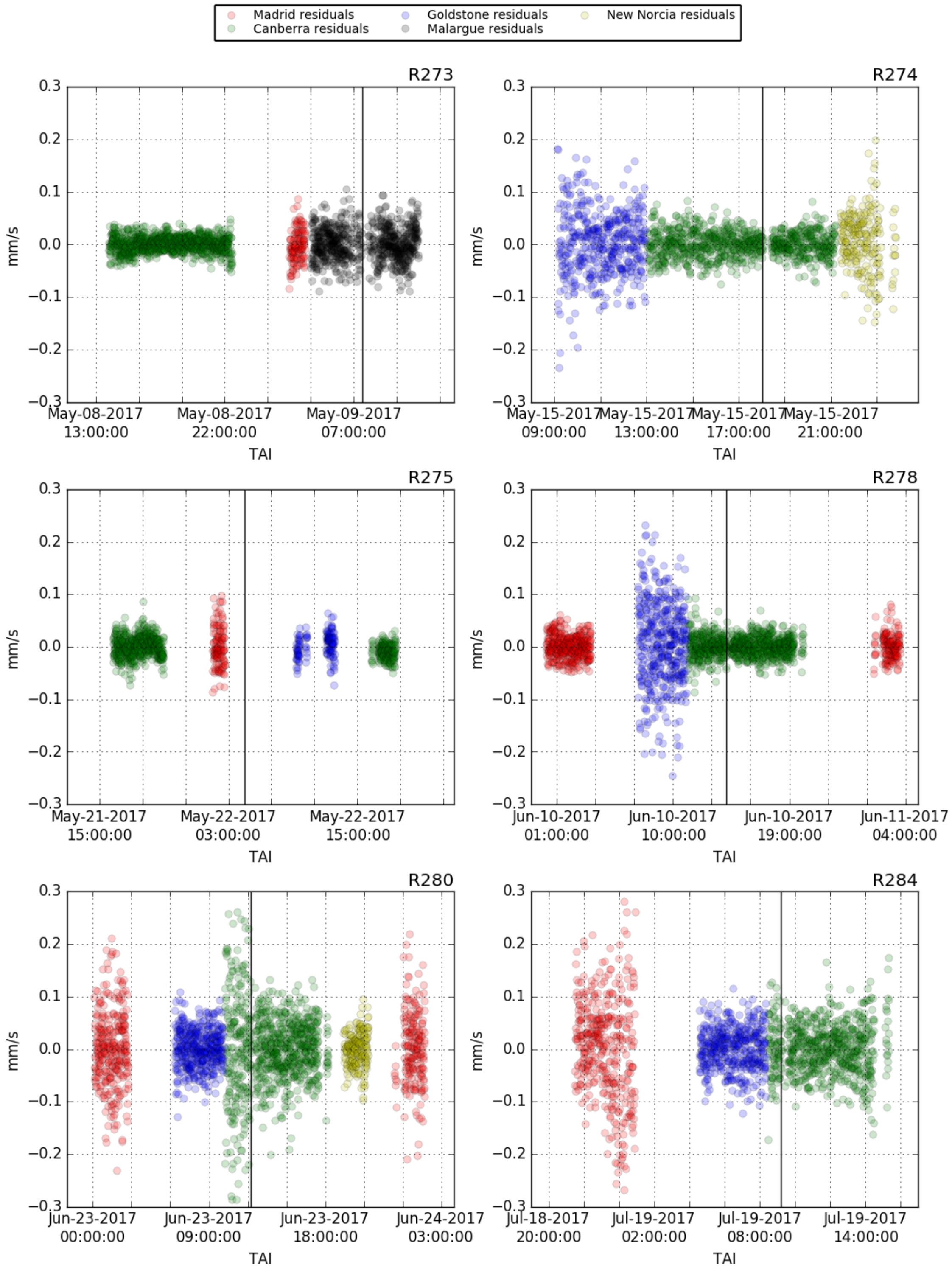

Figure 4.7 – X-band residuals of the close encounters of the Cassini S/C with Saturn during the proximal orbits (CASE-A). The RMS of the residuals can be found in the table 4.1. The vertical line corresponds to the closest approach with Saturn.

Table 4.3 – Periods of the gravitational modes acting on the zonal coefficients of Saturn (in min) [36].

	J_2	J_3
Period (min)	381.5	279.6
	264.8	206.9
	114.2	89.32
	148.5	115.3

Table 4.4 – Periods of the measured acoustic oscillations acting on the sectorial coefficients of Saturn (in min) [40].

Wave name	l,m	Period (min)
W80.98	$(4,4)$	312.2
W82.00	$(3,3)$	298.5
W82.06	$(3,3)$	298.8
W82.21	$(3,3)$	299.6
W84.64	$(2,2)$	278.6
W87.19	$(2,2)$	291.3

- Fundamental acoustic modes (degree 2 to 6) + C-ring fundamental modes (degree 2 and 4) [40]

The choice of the a-priori uncertainty for the acoustic modes is non trivial, because if it is too large, the combination of the different modes would absorb the signal of other parameters. To avoid this situation, we set their value to zero and constrained the uncertainty of the free oscillations to $3 \cdot 10^{-8}$ while the ones found by Hedman were constrained to $3 \cdot 10^{-9}$.

All the presented combinations were able to fit the data properly, obtaining good quality residuals similar to the ones reported in figure 4.7 and obtaining compatible zonal-fields as figure 4.8 evidences. As a reference case, we have chosen the solution that contains both the fundamental modes up to the 8th degree plus the fundamental modes found in [40] (CASE-C).

Comparison A comparison between the low-degree zonal coefficients obtained for CASE-A and CASE-B is shown in 4.9. The plot evidences the good-agreement between the estimated coefficients. Figure 4.10 reports the zonal estimated gravity coefficients up to the 13th degree and its associated 3-σ uncertainty, evidencing the values that are estimated with good accuracy. As can be seen, the even-zonal harmonics, up to J_{12}, are almost the same for the two reference solutions (CASE-A, CASE-B). The odd-zonal harmonics are in good agreement as shown also in 4.9. J_7 might seem different at first sight, but that is because the estimated value is smaller than the associated uncertainty in both cases.

Prior to this analysis, only J_2 ,J_4 and J_6 were properly estimated [49]. The proximal orbits allowed for an estimation of the even zonal-coefficients up to the 12th degree. The estimated coefficients are compatible within 1-σ with the previous estimated values. In addition, this analysis permitted to estimate for the first time the odd-zonal gravity harmonics. The obtained results deviate from the rigid body models, suggesting a strong

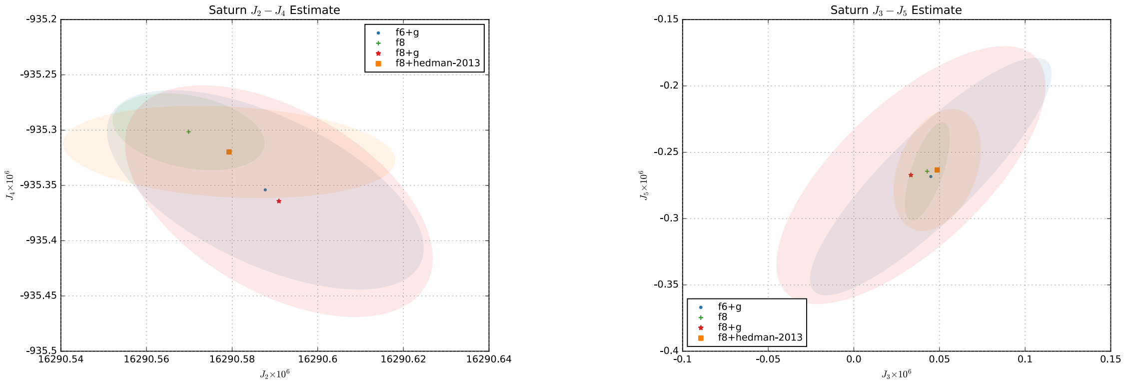

(a) Saturn $J_2 - J_4$ estimate

(b) Saturn $J_3 - J_5$ estimate

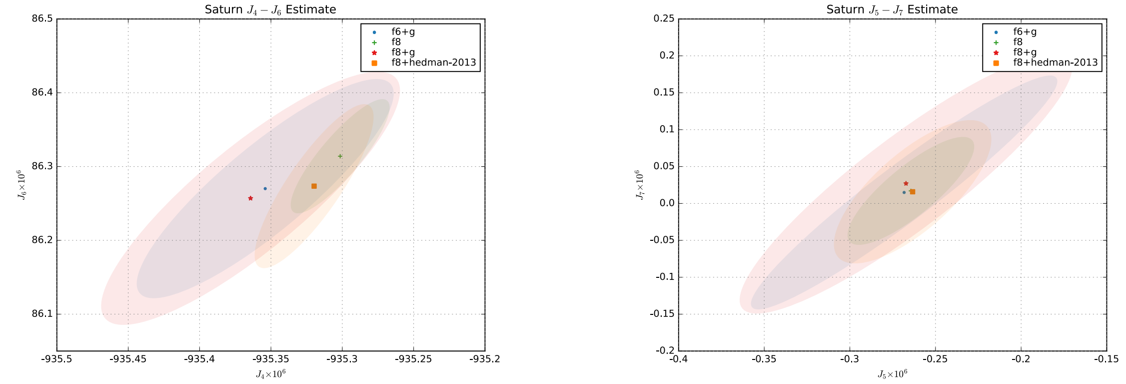

(c) Saturn $J_4 - J_6$ estimate

(d) Saturn $J_5 - J_7$ estimate

Figure 4.8 – Obtained low-degree zonal coefficients, and its 3-σ error ellipses, using different combinations of acoustic modes.

differential rotation with deep winds reaching up to 9000km [53].

Table 4.5 summarizes the values of the obtained zonal coefficients for the two baseline solutions.

Concluding, using two completely different approaches we found a common zonal gravity field, up to the 12th degree. Even though, a common zonal gravity field was found, a non-zonal or time dependent field remains with several possible explanations. More investigations will be carried out to unveil the origin of this anomalous coefficients.

An independent approach has been followed by [43], where in addition to the high-degree non-zonal field and the acoustic modes, they used stochastic accelerations unrelated to any specific physical model to detach the zonal coefficients from the unmodeled accelerations, retrieving full compatible solutions, within 3-σ, with the results presented in this chapter.

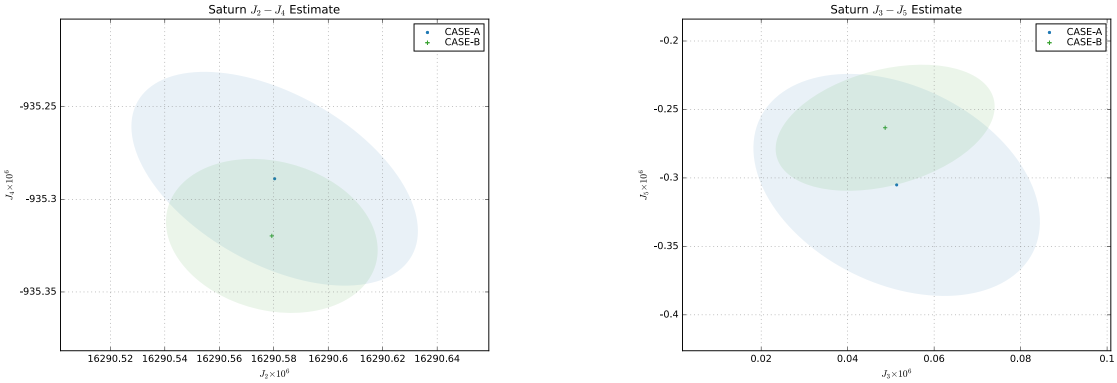

(a) Saturn $J_2 - J_4$ estimate (b) Saturn $J_3 - J_5$ estimate

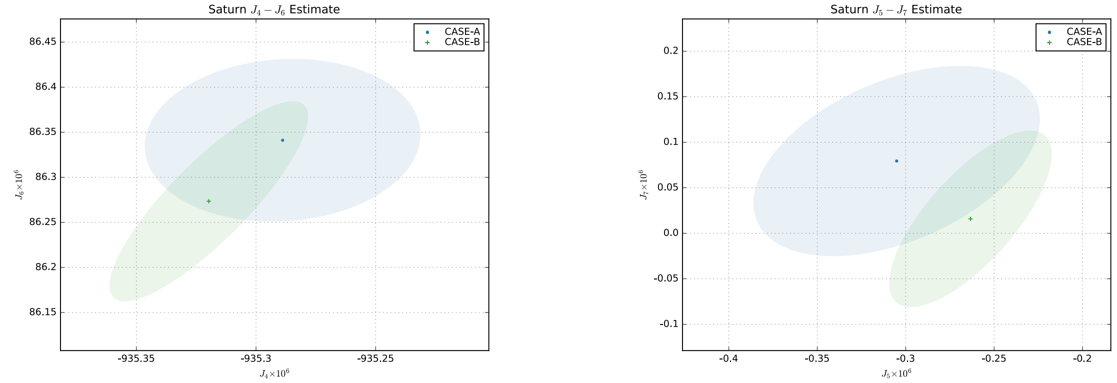

(c) Saturn $J_4 - J_6$ estimate (d) Saturn $J_5 - J_7$ estimate

Figure 4.9 – Obtained low-degree zonal coefficients with its 3-σ error ellipses obtained in CASE-A and CASE-B.

4.5 Titan gravity and orbit evolution

4.5.1 Introduction

Titan, discovered by Christiaan Huygens in 1655, is the second biggest moon of the entire Solar system after Ganymede and the only moon that has more than a trace of an atmosphere.

Previous to the work exposed in this thesis, two different analysis of the Titan gravity field were published. The first of them used data acquired in four flybys, T11 (February, 2006), T22 (December-2006), T33 (June, 2007) and T45 (July, 2008), and considered a purely 3x3 static gravity field [47]. Subsequently, [46], analysed the obtained data of two more flybys, T68 (May-2010) and T74 (February-2011), providing the first measurement of the variable tidal field exerted by Saturn, by means of the k_2 coefficient, evidencing the presence of a global ocean under the surface.

The gravity field of Titan, its tides and its orbital evolution are one of the outputs of the analysis carried out in this thesis. The Doppler data used to obtain this results were obtained during ten gravity-dedicated flybys that Cassini performed over Titan during its entire mission. Figure 4.11 presents the ground track of the Cassini S/C during its

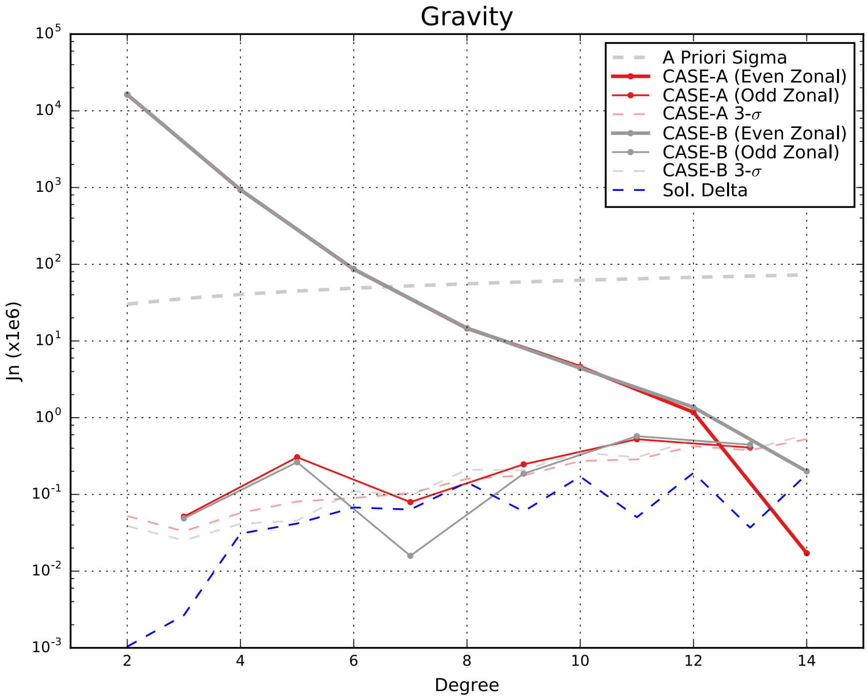

Figure 4.10 – Un-normalized coefficients estimated using the two different exposed approaches with its associated 3-σ uncertainty. In addition the figure shows the difference between both solutions, CASE-A and CASE-B.

Table 4.5 – Non-zonal coefficients of the gravity field of Saturn obtained using two different approaches: CASE-A and CASE-B.

		Apriori	CASE-A	CASE-B
GM	(km^3/s^2)	37940577 ± 10	37940568.7 ± 6.8	37940573.3 ± 6.0
J_2	$(\times10^6)$	16291 ± 30	16290.580 ± 0.017	16290.579 ± 0.013
J_3	$(\times10^6)$	0 ± 36	0.051 ± 0.011	0.0487 ± 0.0084
J_4	$(\times10^6)$	-934 ± 41	-935.289 ± 0.019	-935.320 ± 0.014
J_5	$(\times10^6)$	0 ± 45	-0.305 ± 0.027	-0.263 ± 0.015
J_6	$(\times10^6)$	89 ± 49	86.341 ± 0.030	86.273 ± 0.037
J_7	$(\times10^6)$	0 ± 52	0.079 ± 0.035	0.016 ± 0.032
J_8	$(\times10^6)$	-10 ± 56	-14.610 ± 0.053	-14.754 ± 0.070
J_9	$(\times10^6)$	0 ± 59	0.247 ± 0.059	0.187 ± 0.069
J_{10}	$(\times10^6)$	1 ± 62	4.600 ± 0.091	4.43 ± 0.12
J_{11}	$(\times10^6)$	0 ± 65	-0.524 ± 0.095	-0.57 ± 0.10
J_{12}	$(\times10^6)$	0 ± 68	-1.18 ± 0.14	-1.37 ± 0.17
J_{13}	$(\times10^6)$	0 ± 70	-0.41 ± 0.13	-0.44 ± 0.13
C_{21}	$(\times10^6)$	0.000 ± 0.013	-0.0021 ± 0.0067	-0.0011 ± 0.0031
S_{21}	$(\times10^6)$	0.000 ± 0.013	-0.0059 ± 0.0035	0.0012 ± 0.0024
C_{22}	$(\times10^6)$	0.0000 ± 0.0065	0.0055 ± 0.0021	-0.0032 ± 0.0023
S_{22}	$(\times10^6)$	0.0000 ± 0.0065	0.0037 ± 0.0031	-0.0018 ± 0.0018
GM_{RingB}	(km^3/s^2)	0.78 ± 0.5	1.144 ± 0.358	1.137 ± 0.374

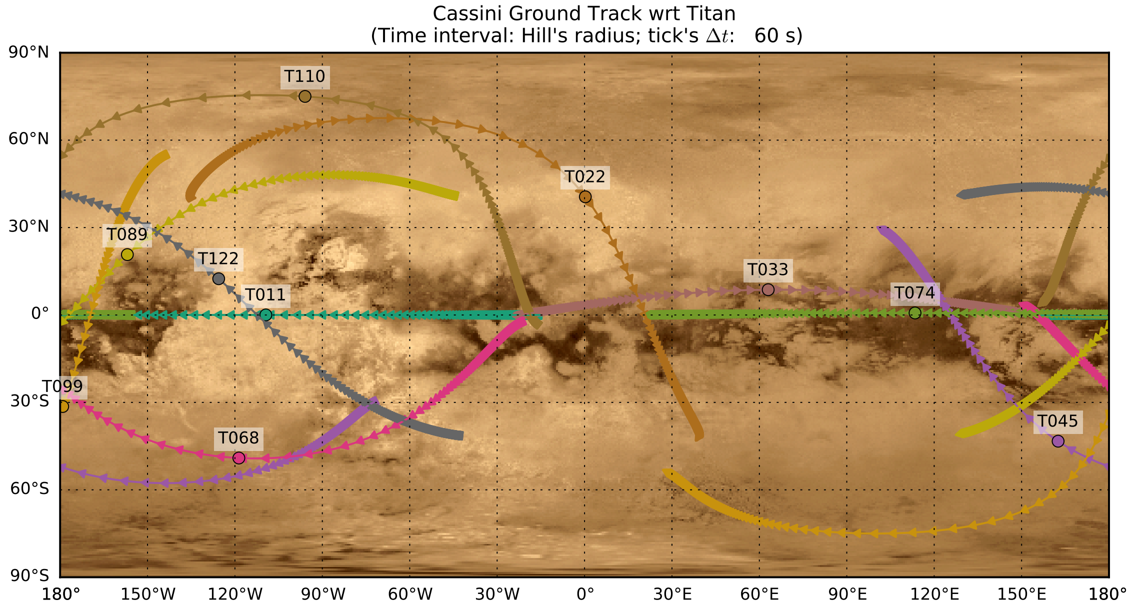

Figure 4.11 – Ground tracks of the flybys performed by Cassini over Titan.

encounters with the satellite. The geometrical parameters and the quality of the data acquired during the encounters are summarized in the table 4.6.

These flybys were properly distributed along Titan's orbit around Saturn, being an optimal configuration to detect the variations of the tidal stresses.

4.5.2 Single-satellite global approach

Given the large number of Titan observations scattered during the timespan of the Cassini mission and with the objective of studying not only the gravity of the ocean-world, but also its orbital evolution, we used the single-satellite global approach.

As introduced in section 2.4, the single-satellite global approach is the classical approach used in the past for the gravity experiments. In the analysis we integrated the orbit of Titan, uniquely, for the timespan in which the gravity-dedicated Titan flybys were performed. The orbits of the other satellites were taken from the satellite system ephemerides of reference, released by the JPL, SAT389.

The latest Saturn ephemerides set, SAT389, is obtained fitting all the available data, that is, radio tracking data of several deep space missions, like Pioneer, Voyager and Cassini, and astrometric data, using a global-fit. The result is a satisfactory orbital-fit, even though, the models that generate the ephemerides may not be perfect. For example, it is known that the relativity and tidal interactions are not included in the global-fit that generated the reference ephemerides set [50]. While fitting the data, an error in the observational model or a missing model used to generate the ephemerides may be absorbed in the initial conditions of the satellites or in the gravity parameters of Saturn, without affecting the goodness of the fit.

So, with the objective of obtaining the best possible fit of Titan's orbit we included in our dynamical model:

- The zonal gravity field of Saturn, result of the Proximal orbit analysis, see section 4.4.
- Saturn Love numbers, $Re(k_{22})$ and $Im(k_{22})$, at Titan's frequency.

The inclusion of the tidal parameters at Titan's frequency and the decision of integrating only Titan, while neglecting the effect of Saturn's Love numbers at Titan's frequency on the other satellites, is justified. As explained in [61], the major secular effect due to the planetary tides is caused when the tide generated in a primary by a secondary is acting back on the secondary. Also, [73] reasons that the effect of the indirect tidal interactions, that are the effects on a secondary body due to the tide generated in a primary body by a third body, average to zero on comparatively short time-scales.

With the objective of testing the indirect tidal interactions, to see if the single-satellite global approach can be applied, we performed the following numerical simulations:

- The orbits of the main satellites of Saturn were integrated using the models that define the SAT389 ephemerides, with the very same initial conditions. In addition, the real part of Saturn Love number k_{22} at Titan's frequency was added to the dynamical model, setting its value to the one reported in [89].
- Then, we integrated all the satellites with the same model explained in the precedent step, adding $Im(k_{22}) = -125.8 \cdot 10^{-5}$. The Imaginary part of the Love number k_{22} corresponds to Saturn's dissipation at Rhea's frequency, recently reported in [61]. The value was chosen because is not compatible with the estimated terms for the other satellites, suggesting a frequency-dependent nature of Saturn's dissipation.

Table 4.6 – Main orbital, geometrical and quality data characteristics of the Cassini flybys over Titan. The values are referred to the C/A.

		T11	**T22**	**T33**	**T45**	**T68**
Date (ERT)	(ET)	27-02-06, 08:26	28-12-06, 10:06	29-06-07, 17:00	31-07-08, 02:14	20-05-10, 03:25
Altitude	(km)	1812.00	1296.80	1932.59	1613.79	1397.63
Relative Velocity	(km/s)	5.88	5.92	6.14	6.25	5.89
Latitude	(deg)	0.023	40.55	8.67	−43.31	−49.09
Longitude	(deg)	−109.38	0.27	63.04	162.53	−118.65
SEP Angle	(deg)	147	131.88	45	29.43	119
Inclination	(deg)	179.97	67.66	8.69	122.33	130.76
Doppler points		1796	1615	1766	1695	1627
RMS	(mm/s)	0.0154	0.0199	0.033	0.070	0.0205
C/A Data		*Y*	*Y*	*Y*	*Y*	*Y*

		T74	**T89**	**T99**	**T110**	**T122**
Date (ERT)	(ET)	18-02-11, 16:05	17-02-2013, 01:57	06-03-2014, 16:27	16-03-2015, 14:30	10-08-2016, 08:32
Altitude	(km)	3651.09	1978.06	1499.70	2274.38	1698.05
Relative Velocity	(km/s)	5.77	5.79	5.83	5.71	5.78
Latitude	(deg)	0.69	20.72	−31.41	75.00	12.43
Longitude	(deg)	113.43	−156.92	−179.11	−95.93	−125.57
SEP Angle	(deg)	133	107	113	111	112
Inclination	(deg)	179.30	132.01	105.11	104.54	136.14
Doppler points		1611	2162	1931	1799	1692
RMS	(mm/s)	0.0755	0.026	0.239	0.0622	0.0613
C/A Data		*Y*	*Y*	*Y*	*Y*	*Y*

- We evaluated the differences in the position of each satellite in a RTN (Radial, Transverse, Normal) frame.
- Finally, for comparison purposes, we evaluated the expected numerical errors of the integration process. To do so, we integrated forward and then backwards, measuring the obtained differences in position at the initial conditions.

Figure 4.12 reports the obtained results, showing the radial, transverse and normal secular differences, that is, averaged with the corresponding orbital period. The figure evidences that the biggest differences caused by the imaginary part of Saturn's love number at Titan's frequency are induced on both Titan and Hyperion transverse direction. Also, Enceladus and Mimas seem to present small deviations, due to their proximity to Saturn, while the mean for the other satellites is zero. This big difference in the Hyperion orbit is not surprising, since Titan and Hyperion are locked in a 4:3 resonance. It is interesting to note that Saturn's dissipation also induces a small secular component in the radial direction of both satellites, that corresponds to the expected radial drift described by equation 3.21, but this perturbation is two orders of magnitude smaller than the transverse direction.

Figure 4.21 presents the expected numerical error of the integration process. The highest error is found in the satellites that are closer to Saturn, Mimas and Enceladus. Actually, the expected numerical noise for both satellites and the obtained secular differences are in the same order of magnitude. The expected numerical error for Titan and Hyperion is negligible when is compared against the obtained secular differences.

Taking into account the presented results, we conclude that the indirect tidal interactions are negligible. Therefore, we can safely study the effect of Saturn's Love numbers at Titan's frequency neglecting the other satellites.

4.5.3 Multi-arc setup

In this section we will address the setup used to estimate the gravity field and orbital evolution of the biggest satellite of the Saturn system, Titan. Radio tracking data obtained in ten different gravity-dedicated encounters, were analysed using MONTE after performing the necessary pre-processing. The residuals were weighted on a pass-by-pass basis using their own RMS and the a-priori weights were chosen on the basis of mathematical models of the expected noise [44].

The least squares information filter solved for the following parameters:

- Initial state of Cassini at the begining of each arc.
- Initial state of Titan at 01-OCT-2010 00:00 ET.
- Titan's gravity field.
- Tidal response of Titan.
- Saturn's gravity field.
- Saturn's tidal response.
- Titan's atmosphere corrections (Only T22, T68 and T99).
- Cassini's RTG accelerations.
- LGA possition (Only T110).

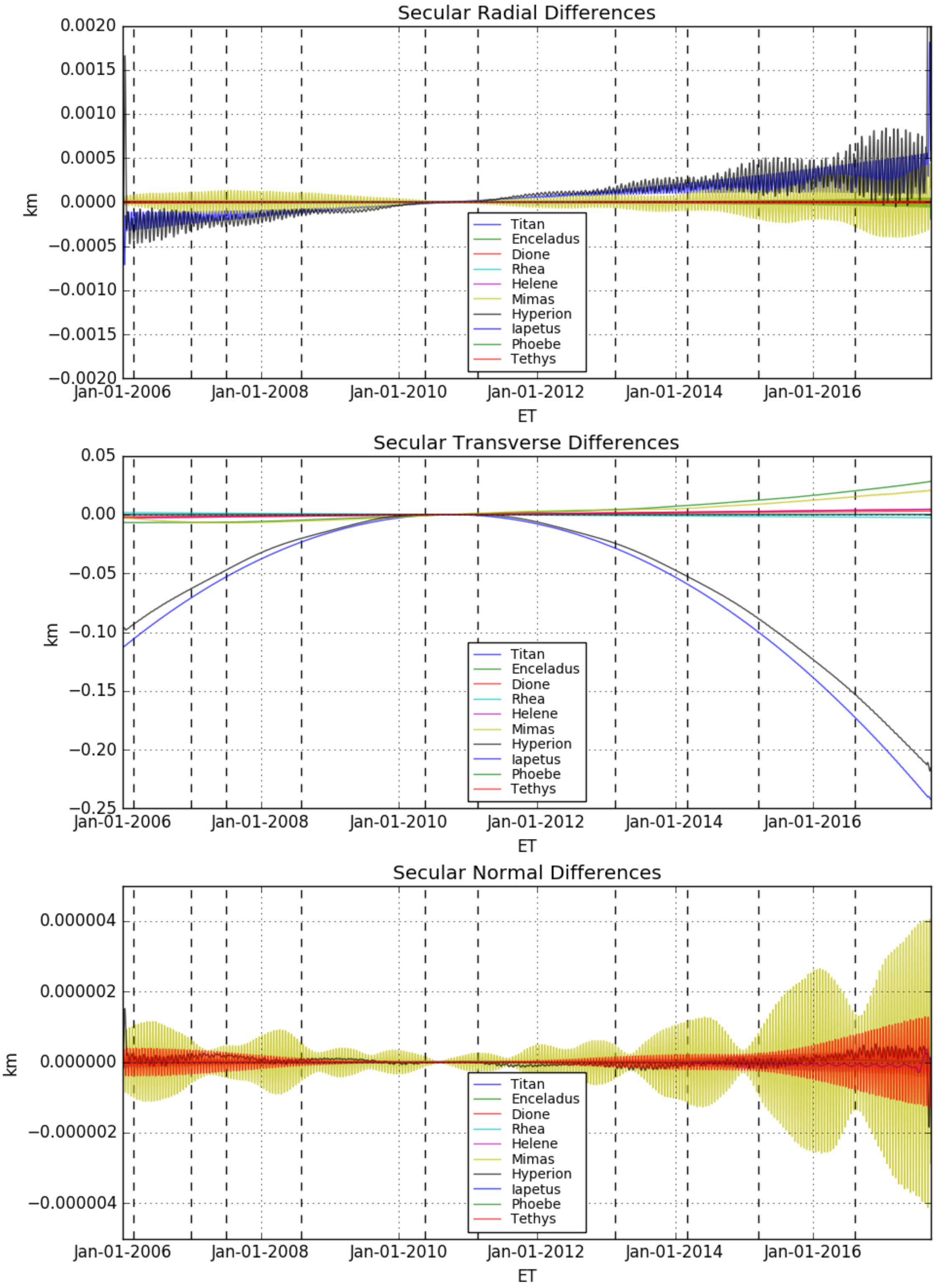

Figure 4.12 – Expected secular differences of the main satellites of the Saturn system due to the dissipation in Saturn at Titan's frequency, using the value of Rhea, in the RTN frame. The dashed lines correspond to the different Cassini gravity-dedicated encounters of Titan.

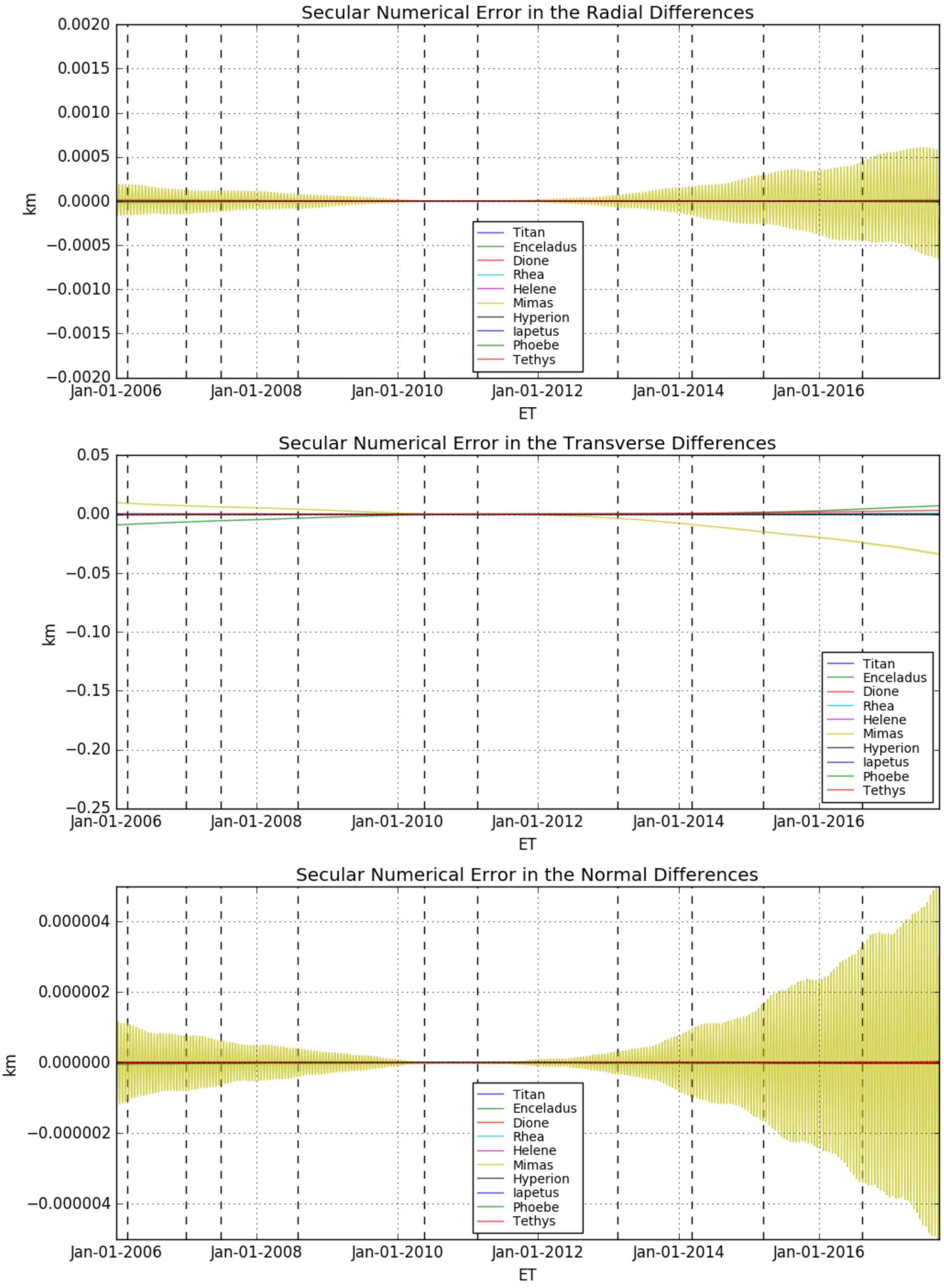

Figure 4.13 – Expected numerical error in the integration of the satellites.

- Small forces attitude corrections (Only T110).
- F3 bias.
- SRP.

Initial state of Cassini The state vector of the Cassini S/C is estimated at the beginning of each arc, approximately one day prior to the C/A. The a-priori values are obtained from the last reconstructed trajectory by the Cassini NAV Team. For the a-priori uncertainty, we used a pretty conservative approach, using a diagonal covariance matrix with 1-σ of 20 km for the position and 0.2 m/s for the velocity. This values are way larger than the uncertainties provided by the Cassini navigation team in order to not constrain the solution in any sense.

Initial state of the Satellite The reference epoch was chosen at the halfway point of the mission, to reduce the numerical errors. The a-priori values of the state vector of Titan were retrieved from the last Saturn ephemerides set released by the JPL, SAT389. The a-priori uncertainties were also set using a conservative approach, 300 km for the position and 30 m/s for the velocity.

Atmosphere corrections To take into account the possible variability of Titan's atmosphere, we estimated small corrections for it. They were introduced in T22, T68 and T99 flybys in form of small trajectory manoeuvres in the direction of the velocity of the S/C. The a-priori value was set to zero, while the a-priori uncertainty was $1 \cdot 10^{-7}$ km/s.

LGA position The motion of the LGA phase center with respect to the center of mass of the S/C induces a Doppler shift on the signal. During T110, Cassini obtained, for the first time, gravity data using its LGA. Its a-priori position in the S/C frame was retrieved from the navigation files. The a-priori uncertainty was set large enough in order to not constraint the analysis.

Small Forces - attitude corrections During T110 two different attitude manoeuvres occurred. Its values were retrieved from the Navigation gin-file. An a-priori uncertainty of 0.5 m/s was used.

F3 biases F3 biases were added to prevent errors due to the possible DSN inter-station clock offset. The values were set to zero with an a-priori sigma of 0.05 Hz.

Saturn's gravity field Using a single-satellite global approach we are sensitive to Saturn's gravity field due to Titan's orbital motion. We estimated the low degree zonal harmonics up to 6th degree. As a-priori values we used the zonal coefficients retrieved in the grand-finale analysis. The uncertainty was set to 5 times the obtained formal sigma.

Saturn's tidal response The single satellite global approach allows us to study the effect of the tidal response of a satellite at a certain frequency. We set the $Re(k_{22})$ to the value retrieved in [89] with a large a-priori uncertainty. The $Im(k_{22})$ was set to zero with an a-priori sigma of 0.005.

Titan's gravity field The a-priori values of the GM, J_2, C_{22} and k_2 were retrieved from [46] while the values that correspond to other coefficients were all set to zero. The a-priori uncertainty was set to 50 times the published formal uncertainty for the 2nd degree. For higher coefficients we used the Kaula's rule, which gives a bound on the RMS of the gravity coefficients of each order, using $A_k = 6.67$.

4.5.4 Results

The figures 4.14, 4.15, 4.16 and 4.17 displays the Doppler and the two-way range post-fit residuals obtained in the analysis of the radio tracking data, acquired during the flybys that Cassini performed over Titan during its mission. We ran eight iterations to assure the solution stability. A 4x4 gravity field was sufficient to fit the data adequately without evident signatures around the C/A. Moreover, the residuals obtained in all the performed test, described in 4.5.5, were all similar. The RMS of all the arcs are comparable but for T45, T74 and T122 in which the SEP was lower than 50 deg, increasing the plasma noise.

The figure 4.18 shows the obtained values of the J_2 and C_{22} in the $J_2 - C_{22}$ plane, along with their 3-σ error ellipses. The results are compared with the ones published in [46] and against the last estimation of the RS Team, obtained following a local-approach, (Personal communication of Daniele Durante). The solution retrieved in this study corresponds to an hydrostatic gravity field, fully compatible with the last estimation of the RS Team. However, it is different by more than 4-σ with respect to [46]. Figure 4.18 displays the obtained result, together with the solutions used for comparison purposes, in the 3-σ $J_2 - C_{22}$ plane. This difference could be caused by the addition of the 4th gravity field degree. The estimated gravity coefficients together with Titan's Love number are exposed in table 4.7.

Figure 4.19 reports on the degree-4 gravity field anomalies together with their associated uncertainties. The gravitation anomalies are refereed to the equipotential surface defined by the gravity coefficients J_2, C_{22} and Titan's rotation. Note the correlation between the ground-tracks of the Cassini over Titan, in figure 4.11, and the associated uncertainty of the figure 4.19. The uncertainty is lower in the zones that are covered by the flybys, principally the equator and the sub-saturnian point.

As introduced before, the global coverage of the flybys in the orbital frame of Titan together with the non-negligible eccentricity, allowed to estimate the real part of the Love number k_2 of Titan. The estimated value of the $Re(k_2)$ is compatible with the previous published value and with the last estimation of the RS Team, within 1.7-σ and 0.5-σ respectively. The obtained value confirms that the satellite is highly deformable over its orbital period, about 16 days. The addition of the imaginary part did not provide substantial changes in the solution. The retrieved value was compatible with zero at less than 1-σ, that is why the value was not introduced in the parameter space of the baseline solution. Even tough, it provided the following lower limit $Im(k_2) = -0.148$ at 3-σ.

In addition, the stability of the estimated gravity field coefficients has been tested against another rotational model. The rotational model given in [69], estimated using SAR images of Titan, returned a gravity solution statistically compatible within 3-σ.

4.5.5 Orbital evolution

The single satellite global approach allows us to study the orbital evolution of Titan.

The Saturn gravity solution and tidal parameters that define the outward motion of the satellites are reported in table 4.8. All the estimated gravity coefficients are compatible

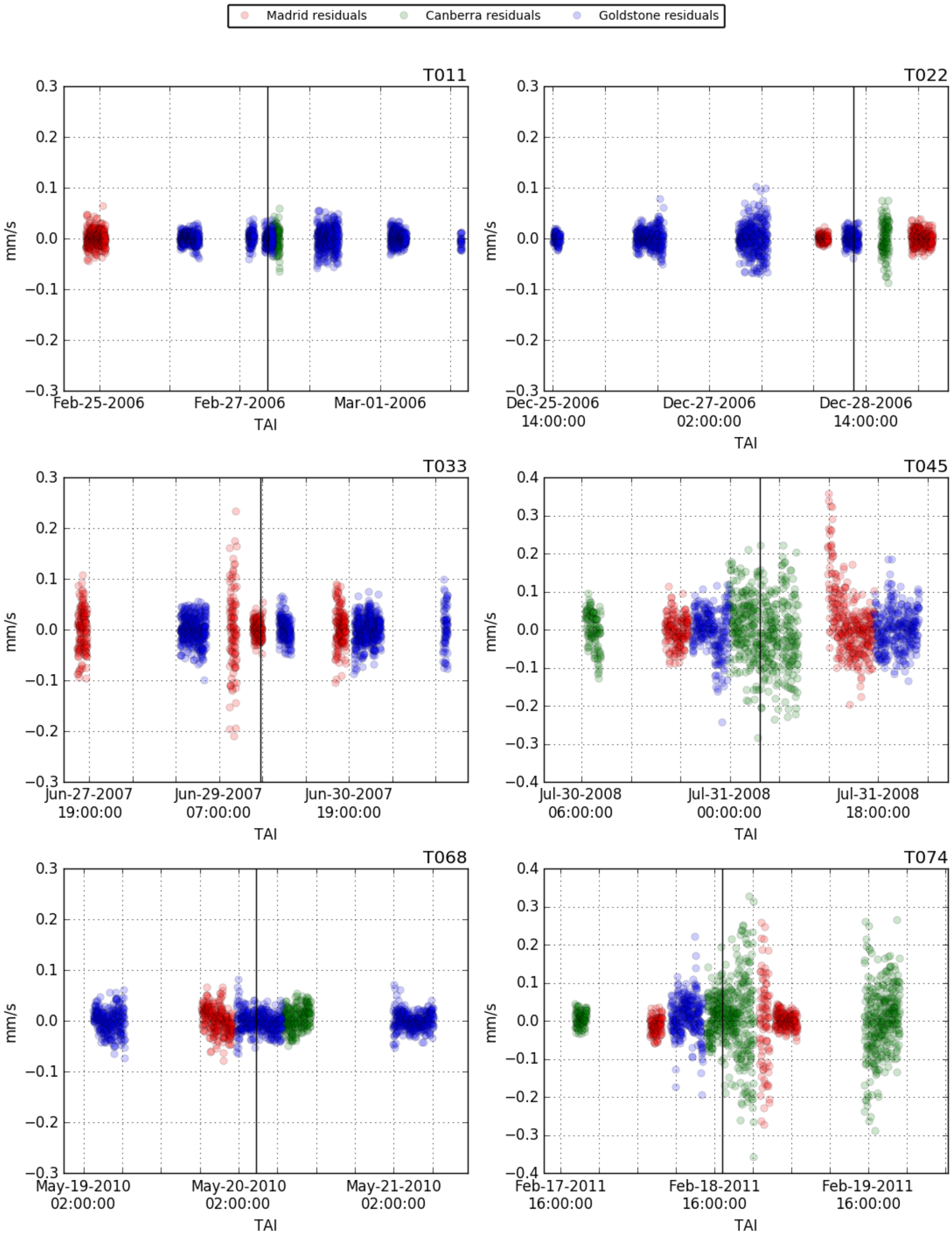

Figure 4.14 – Doppler residuals for the first six gravity-dedicated flybys of Cassini over Titan. The vertical line corresponds to the closest approach with Titan.

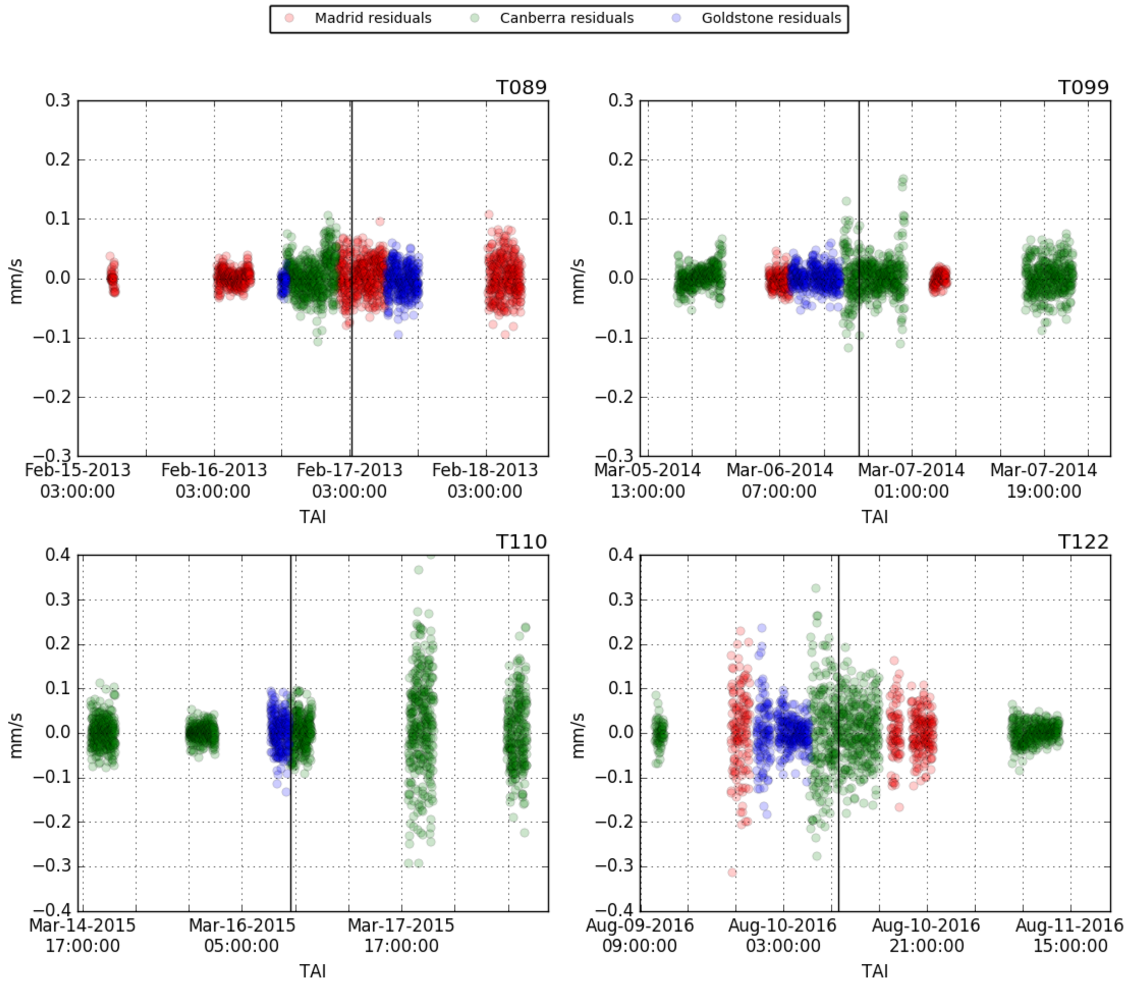

Figure 4.15 – Doppler residuals for the last four gravity-dedicated flybys of Cassini over Titan. The vertical line corresponds to the closest approach with Titan.

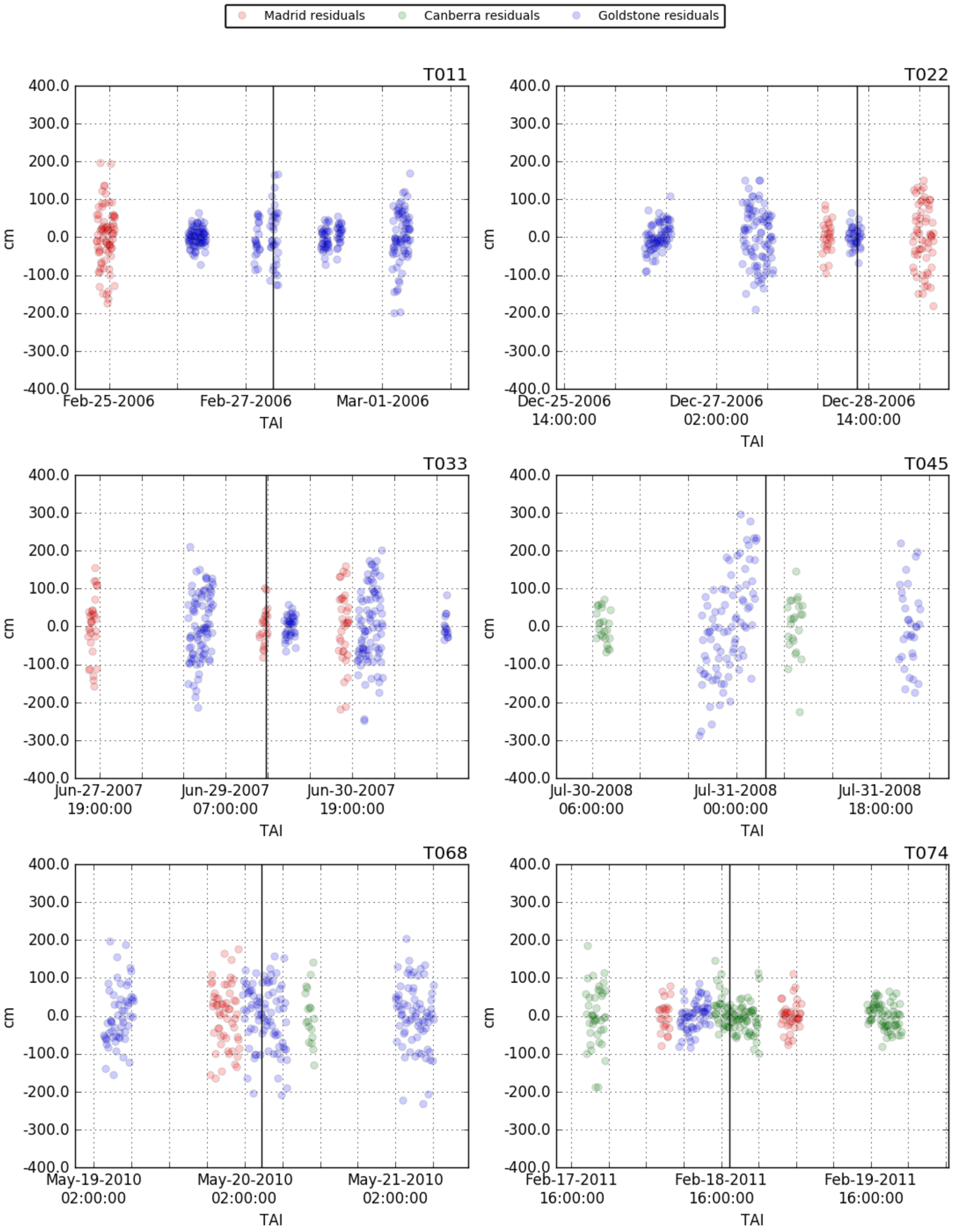

Figure 4.16 – Two-way range residuals for the first six gravity-dedicated flybys of Cassini over Titan. The vertical line corresponds to the closest approach with Titan.

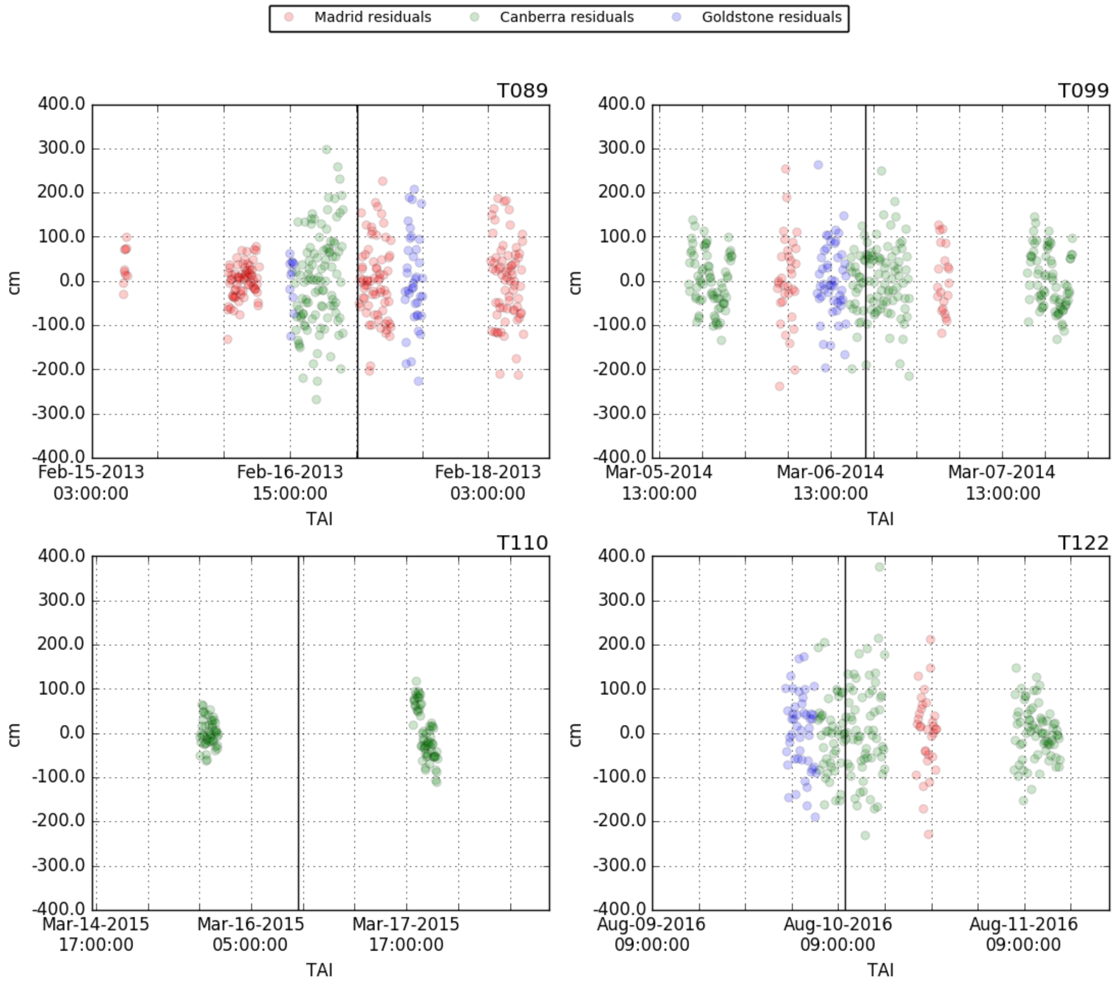

Figure 4.17 – Two-way range residuals for the last four gravity-dedicated flybys of Cassini over Titan. The vertical line corresponds to the closest approach with Titan.

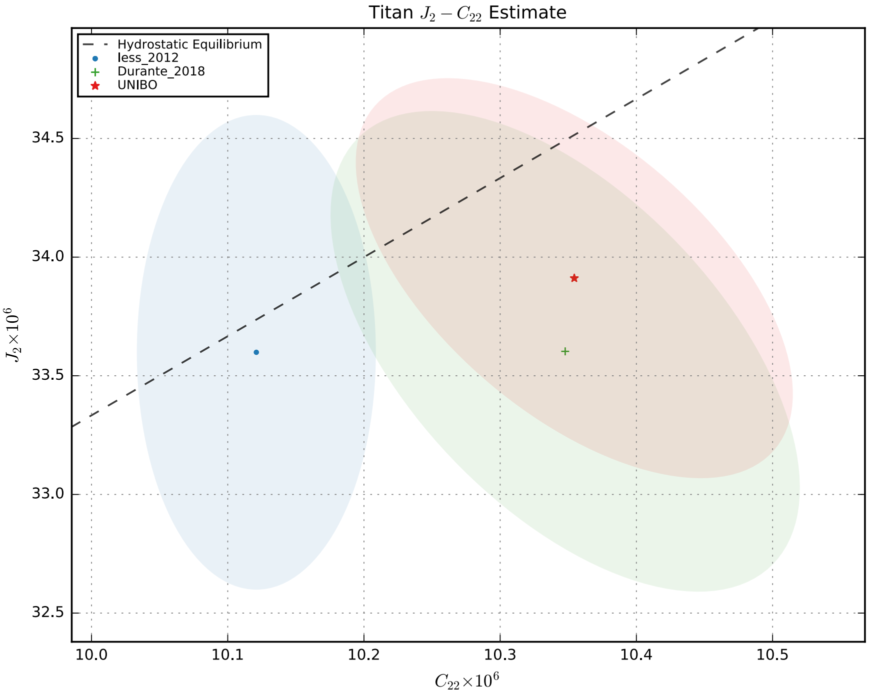

Figure 4.18 – Titan's single-satellite global approach solution, RS multi-arc local approach (Personal communication of Daniele Durante) and last published solution [46], in the $J_2 - C_{22}$, 3-σ plane.

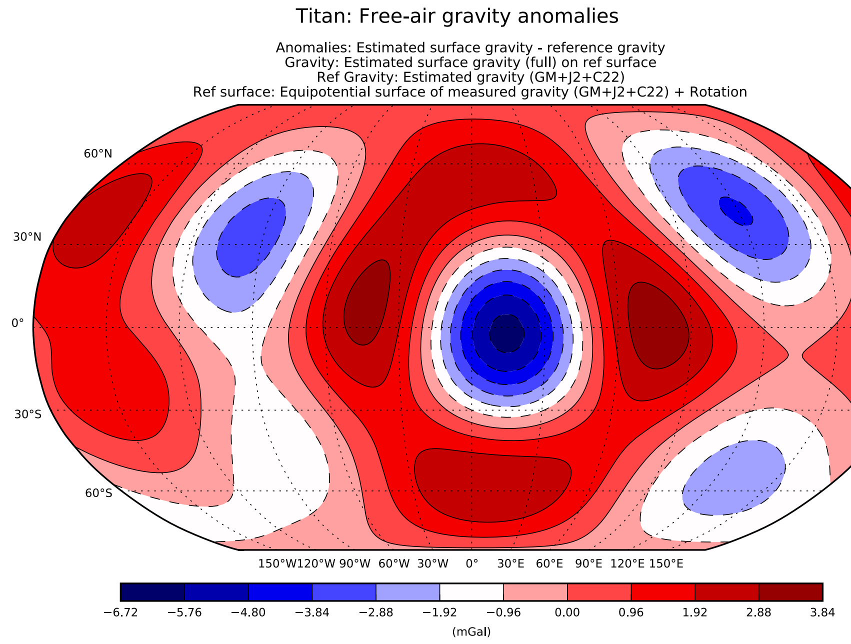

Titan: Free-air gravity anomalies

Anomalies: Estimated surface gravity - reference gravity
Gravity: Estimated surface gravity (full) on ref surface
Ref Gravity: Estimated gravity (GM+J2+C22)
Ref surface: Equipotential surface of measured gravity (GM+J2+C22) + Rotation

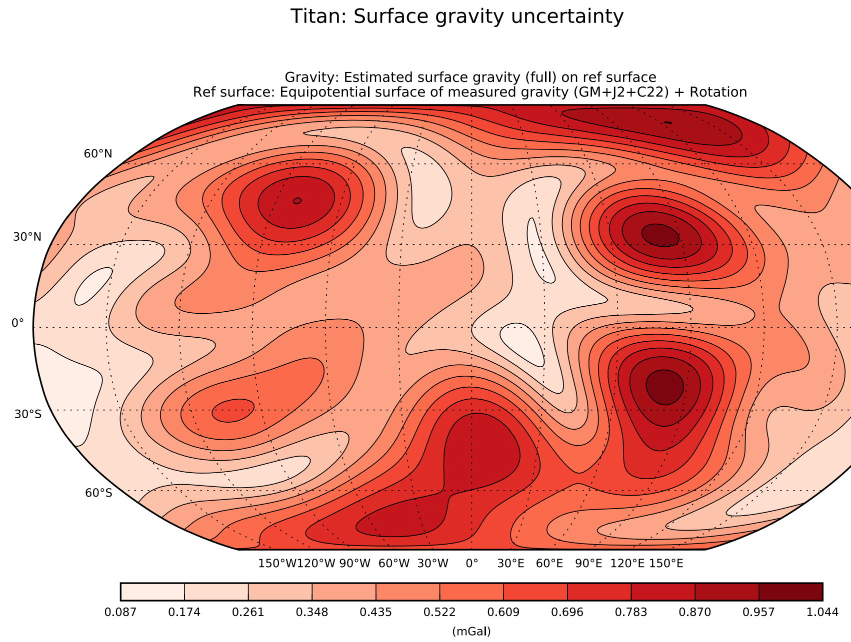

Titan: Surface gravity uncertainty

Gravity: Estimated surface gravity (full) on ref surface
Ref surface: Equipotential surface of measured gravity (GM+J2+C22) + Rotation

Figure 4.19 – Obtained Titan gravity anomalies and their associated uncertainty.

Table 4.7 – Estimated gravity field coefficients of Titan

		Apriori	Global solution
GM	(km^3/s^2)	8978.14±0.25	8978.13798±0.00015
J_2	$(\times 10^6)$	33.59±17.5	33.91±0.28
J_3	$(\times 10^6)$	0±15	−0.58±0.47
J_4	$(\times 10^6)$	0.0±8.1	−0.04±0.94
C_{21}	$(\times 10^6)$	0.0±5.0	0.10±0.16
S_{21}	$(\times 10^6)$	0.0±5.0	−0.17±0.19
C_{22}	$(\times 10^6)$	10.12±1.5	10.354±0.053
S_{22}	$(\times 10^6)$	0.0±2.5	−0.024±0.042
C_{31}	$(\times 10^6)$	0.0±5.9	1.33±0.12
S_{31}	$(\times 10^6)$	0.0±5.9	−0.16±0.23
C_{32}	$(\times 10^6)$	0.0±1.9	0.22±0.10
S_{32}	$(\times 10^6)$	0.0±1.9	0.037±0.035
C_{33}	$(\times 10^6)$	0.00±0.77	−0.2103±0.0085
S_{33}	$(\times 10^6)$	0.00±0.77	−0.2401±0.0096
C_{41}	$(\times 10^6)$	0.0±2.6	−0.35±0.13
S_{41}	$(\times 10^6)$	0.0±2.6	−0.09±0.30
C_{42}	$(\times 10^6)$	0.00±0.60	0.255±0.047
S_{42}	$(\times 10^6)$	0.00±0.60	0.150±0.034
C_{43}	$(\times 10^6)$	0.00±0.16	−0.020±0.013
S_{43}	$(\times 10^6)$	0.00±0.16	−0.006±0.013
C_{44}	$(\times 10^6)$	0.000±0.057	−0.0088±0.0019
S_{44}	$(\times 10^6)$	0.000±0.057	−0.0106±0.0015
k_{22}		0.589±1.0	0.648±0.034
J_2/C_{22}		3.32±11.7	3.275±0.039
corr J_2-C_{22}		+0.00	−0.58

within 3-σ with respect to the a-priori solution. It is interesting to note, that the obtained uncertainty for the J_2 is in the similar order of magnitude than the one retrieved in the proximal orbit analysis. This is a clear indication that the orbits of the satellites are sensitive to the J_2 at about the same level than the proximal orbits. A future global-approach could improve this value.

Table 4.8 – Estimated gravity field coefficients of Saturn and its Love numbers, using the single satellite global-approach

		Apriori	Global solution
GM	(km^3/s^2)	37940585±5	37940585±0.3
J_2	$(\times 10^6)$	16290.57±0.107	16290.56±0.025
J_3	$(\times 10^6)$	0.059±0.038	0.061±0.038
J_4	$(\times 10^6)$	−935.31±0.061	−935.31±0.056
J_5	$(\times 10^6)$	−0.22±0.09	−0.22±0.09
J_6	$(\times 10^6)$	86.34±0.144	86.33±0.143
$Re(k_{22})$		0.39±0.12	0.353±0.108
$Im(k_{22})$	$(\times 10^3)$	0.0±5	−3.06±0.207

One of the most notable parameters, estimated with the single-satellite global approach, is the value of the $Im(k_{22})$ and its corresponding uncertainty. This value is a promising result, being the first estimation of this term using radiometric observables. Moreover, this value, together with the estimated term at Rhea's frequency [61], provides a second evidence of the frequency dependent nature of Saturn Love's numbers.

The estimated k_{22} can be linearly mapped to the quality factor, obtaining $Q_p = 115.35 \pm 36.15$. This value is difficult to explain under classical tidal theory, because the satellite outward migration, which can be described by 3.21, is proportional to $(1/Q_p)$, implying a really young Titan.

Alternatively to the classical tidal theory, the resonance locking theory [33] provides a plausible mechanism to explain the low present-day values of the Saturn satellites, as the one of Titan obtained in this work. The figure 4.20, generated by J. Fuller, shows our estimated Q_p with its associated 1-σ, compared against the resonance locking expected value. Both values are compatible at 3-σ.

In addition, an independent estimation of this value, retrieved using a combination of long-baseline Earth-based observations and Cassini astrometric data, has been performed by V.Lainey, obtaining also a low-present day Q_p compatible with the result presented in this dissertation thesis (V. Lainey personal communication).

As can be seen from figure 4.20, under resonance locking, with the observed Q_p, Titan's migration time-scale would be about of 10 Gyr, implying that Titan's formation is compatible with the age of the solar system.

To assure the obtained result we first had to understand where the sensitivity to the parameter came from, and then, test the robustness of the obtained results.

Sensitivity of $Im(k_{22})$ With the objective of retrieving the origin of the sensitivity to the $Im(k_{22})$ parameter, we studied the differences on the retrieved Titan trajectory with respect to the last published Saturn satellites ephemerides set SAT389.

As show in figure 4.21, we obtained secular differences of about 4 m in the radial direction, 450 m in the transverse direction and 10 m in the normal direction. To get an idea of the meaning of the presented result, we compare it against the obtained uncertainty

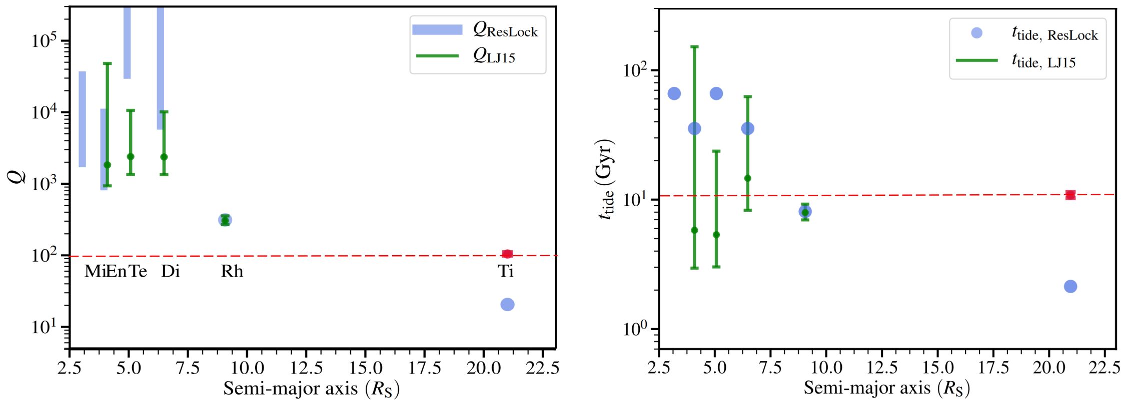

Figure 4.20 – a) Measured Q_p at different frequencies against the expected value for the resonance locking mechanism. b) Expected migration time-scale for Saturn satellites. Note: The result does not take into account the mean-motion resonances. Values of Q_p at other satellites frequencies, other than Titan, were retrieved from [61]. Credits: J. Fuller.

of Titan's position in the radial, transverse and normal directions, with respect to Saturn during the Cassini mission. The result is displayed in figure 4.22.

This comparison indicates that our sensitivity in the radial direction is about 4 m, just the obtained difference of our Titan trajectory with respect to SAT389. The uncertainty in the normal direction is higher than the obtained difference, indicating that we are not sensitive to the normal differences. Finally, we realize that the transverse differences are higher than the obtained uncertainty concluding that our sensitivity to the $Im(k_{22})$ comes from the secular differences in the Titan transverse direction.

Once concluded that our parameter comes from the sensitivity to the transverse direction of Titan, during the Cassini-mission, we ran different robustness test to assess the stability of the obtained $Im(k_{22})$.

Gravity fields of Titan and Saturn The obtained results provided gravity fields for both Titan and Saturn compatible with the last estimations of the RS team, as demonstrated by tables 4.18 and 4.8.

Stability with respect to different satellite ephemerides The single satellite global approach takes the position of the other satellites, that may influence the motion of the satellite of study, directly from the satellite system ephemerides of reference. To assess the stability of the solution and check the dependency to the other satellites orbits of reference we used the following different ephemerides sets: SAT389, SAT375 and SAT365 obtaining solutions compatible within 1-σ.

Stability with respect to different $Re(k_{22})$ Even though the $Re(k_{22})$ is not observable, its value may influence the orbital evolution of Titan and the estimation of the $Im(k_{22})$. Hence, we used two different strategies to study the stability of the solution to the change of $Re(k_{22})$ of Saturn at Titan's frequency.

- $Re(k_{22}) = 0.4137 \pm 0.5$. The a-priori value was retrieved from [89], obtained from theoretical models. We used a large a-priori uncertainty. We followed two different strategies, add the parameter as a solve-for parameter and as a considered parameter.

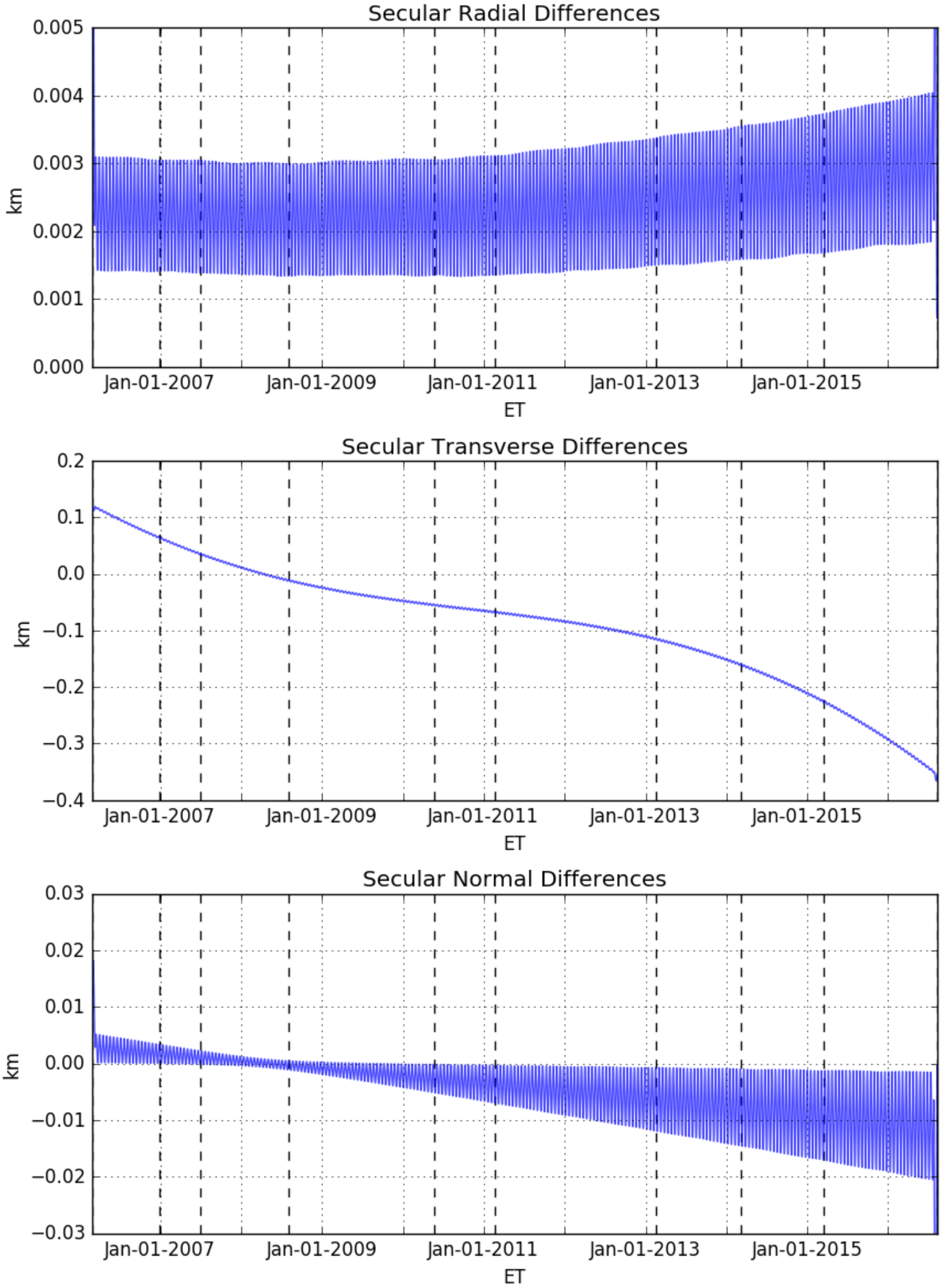

Figure 4.21 – Obtained radial, transverse and normal secular differences between the estimated orbit of Titan and the reference ephemerides SAT389. The dashes black lines represent the gravity-dedicated encounters of Cassini with Titan.

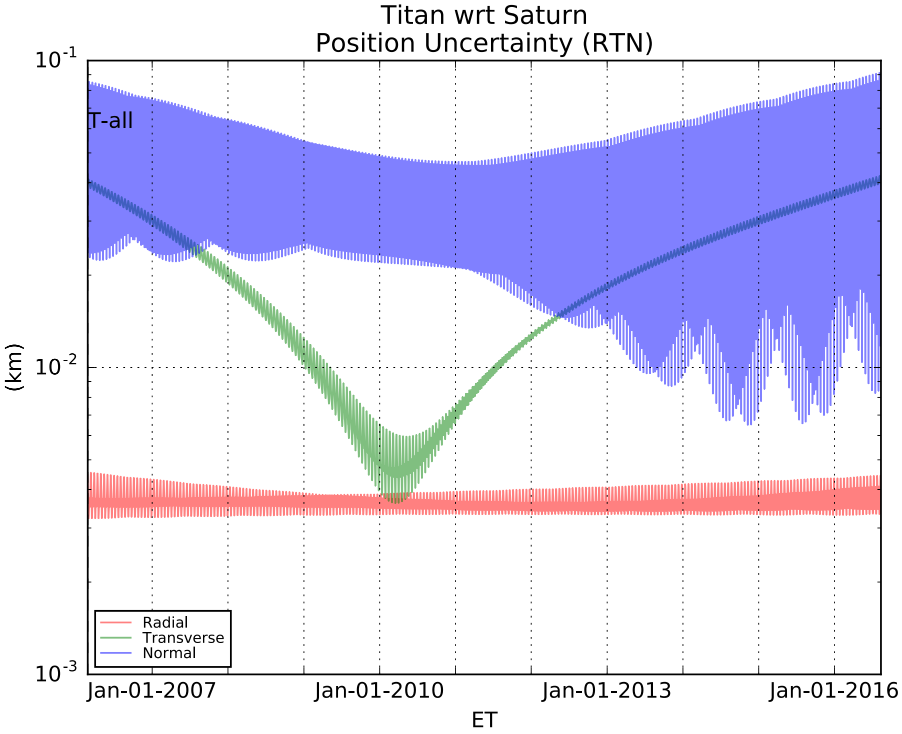

Figure 4.22 – Obtained radial, transverse and normal uncertainties for Titan trajectory with respect to Saturn.

The consider parameters are useful to take into account the uncertainty of a certain parameter into the analysis, even if the used data is not sensitive to it.

- $Re(k_{22}) = 0.39 \pm 0.12$ [61]. The a-priori uncertainty was set to 10 times the one provided in the publication. Just as the previous case, we estimated and considered the parameter.

In all cases the solution was full-compatible within 1-σ demonstrating the stability of the retrieved coefficient.

Chapter 5

Jovian system data analysis

Contents

5.1 Introduction

As the Saturn system, the Jovian system is a complex dynamical system that involves complex interactions between the satellites and the central body.

These interactions comprise the 1:2:4 Laplace resonance between Io, Europa and Ganymede, and the tidal interactions between Jupiter and Io that result in volcanic activity which creates the Io Plasma Torus, a toroidal cloud of plasma that orbits around Jupiter at Io's orbital distance.

As explained before, the gravity determination can provide constraints, not only on the interior of the gas giant but also on the satellite-system dynamics. With the objective of acquiring measurements of the gravity field of Jupiter, the Juno S/C has been performing several close encounters with the gas giant since August 2016.

In this dissertation thesis, we will address the data pre-processing and the performed data-analysis, that have as objective the determination of an updated gravity field of Jupiter. The work done in this thesis contributed to two different publications [32] and

[45]. Subsequently, two different papers extrapolated conclusions about the interior of the gas giant using the measured gravity field coefficients [52] and [37].

This chapter, will also focus on the Galilean satellites, by means of the re-analysis of the radio tracking data of the Galileo mission, 15 years after the probe plunged in Jupiter. The main purpose is to obtain new estimates of the gravity fields of the main moons of Jupiter, using the local multi-arc approach, and to study the potential effect of the IPT in the gravity experiment.

5.2 The gravity field of Jupiter from Juno data analysis

Jupiter is the biggest planet in the Solar system. Before the arrival of Juno to the Jovian system, the planet was visited by Pioneer, Voyager and Galileo. Juno's trajectory has been specifically designed to acquire measurements of the gravity and magnetosphere of the gas giant in order to unveil its interior. Tracking the motion of Juno, perturbed due to the attraction of the gas giant during the perijoves, can be used to infer the accelerations that the S/C is exposed to. In that way, solving the OD problem, we can measure, at an unprecedented level, the coefficients that define the gravity field of Jupiter, which is an indispensable input to model the interior of the gas giant.

5.2.1 Juno Dynamical Model

The dynamical model used in our analysis takes into account multiple forces acting on both the celestial bodies and the S/C: gravitational forces that act indifferently on all the bodies in the solar system, and on the spacecraft, and forces of non-gravitational origin, that only affect the S/C motion. Mathematical details of the implementation of these models in MONTE can be found in [30], [72] and [71].

Gravitational accelerations

In our dynamical model, the sources of the gravitational forces are all the main bodies of the solar system, the sun, the solar system planets and the Jovian satellites. In particular, the following effects were included:

- Relativistic point-mass gravity acceleration from the Sun, the planets, the Moon and Pluto. The state vectors were obtained from JPL planetary ephemerides DE435.
- Relativistic point-mass gravity acceleration from Jupiter. The state vector was obtained from JPL's Jupiter ephemerides JUP310.
- Relativistic acceleration from the Jupiter's satellites Adrasthea, Amalthea , Io, Europa, Ganymede, Callisto, Methis and Thebe. The state vectors were obtained from the JPL Jupiter system ephemerides JUP310.
- The gravity field of Jupiter, represented by the standard spherical harmonic expansion of its gravitational potential retrieved from Jupiter system ephemerides JUP310.
- The gravity field of the main Galilean satellites, Io, Europa, Ganymede and Callisto, represented by means of the spherical harmonic expansion, retrieved from the last publications of the RS Team.
- Tides arisen in Jupiter by its satellites.

In addition, the effect of Jupiter's large oblateness (J_2) was taken into account when computing the Doppler observables.

Rotational model For Jupiter the model adopted is the rotational model of the ephemerides set JUP310, defined by:

$$\alpha(deg) = 268.0570781451590 - 0.0065543281855586419T \tag{5.1}$$
$$\delta(deg) = 64.49582320291580 - 0.002476496988122852T \tag{5.2}$$
$$W(deg) = 284.95 + 8.70536d \tag{5.3}$$

Where:

- α: right ascension of the north pole with respect to EME2000.
- δ: declination of the north pole with respect to EME2000.
- W: angle measured easterly along the body's equator between the prime meridian and the ascending line of nodes.
- T: time measured in Julian centuries (36525 days) past J2000.
- d: time measured in days past J2000.

Non gravitational accelerations

In addition to the gravitational accelerations, the only non-gravitational acceleration we took into account was the solar radiation pressure.

5.2.2 Data selection and calibration

During the close encounters range-rate measurements acquired by the DSN antennas in Goldstone at X (8.4GHz) and Ka (32GHz) bands have been used to determinate the gravity field of Jupiter. The only exception was PJ01 in which the data was acquired by the Madrid complex instead. In addition to the close encounter data, shortly after the C/A, data were acquired by the DSN antennas in Canberra during PJ03, PJ06, and PJ08.

The tracking data were corrected for the Earth media effects, the troposphere and the ionosphere. Also, AMC corrections, available during all the radio science dedicated perijoves were applied. The AMC corrections have proven to be a great tool to reduce the noise and provide a big improvement on the RMS of the residuals (see table 5.1).

Table 5.1 – Multi-frequency link calibration and AMC improvements in the different Juno flybys in terms of % of the RMS.

Encounter	Calibration Type	Calibration imprv.	AMC imprv.
$PJ1$ (Rj)	Single-link calibration	−2.7% w.r.t X/Ka	
$PJ3$ (Rj)	Dual-link calibration	−6.9% w.r.t Ka/Ka	−50% w.r.t TSAC
$PJ6$ (Rj)	Dual-link calibration	−3.6% w.r.t Ka/Ka	−40% w.r.t TSAC
$PJ8$ (Rj)	Dual-link calibration	+5.0% w.r.t Ka/Ka	−62% w.r.t TSAC
$PJ10$ (Rj)	Dual-link calibration	+10% w.r.t Ka/Ka	−41% w.r.t TSAC
$PJ11$ (Rj)	Dual-link calibration	−9.5% w.r.t Ka/Ka	−13.3% w.r.t TSAC
$PJ13$ (Rj)	Single-link calibration	−2.0% w.r.t X/Ka)	−13.5% w.r.t TSAC

Furthermore, since the transmitted and received signals are circularly polarized and Juno spins at 30 rpm, we corrected the data to take into account the expected additional frequency shift, explained by equation 4.5.

The DSN antennas received two downlink signals at X and Ka bands coherent with X and Ka bands respectively, allowing the calibration of the dispersive effect of the plasma using the dual-link calibration technique [66], [20]. The dual-link calibration technique allows to reduce the dispersive noise by about 75% when compared to the non calibrated Ka/Ka link.

During PJ1 and PJ13 the dual-link calibration technique could not be applied, due to the unavailability of the Ka-uplink in the DSS-55 and DSS-26 respectively. In both cases, we used instead the single link calibration, which allowed to solve for the downlink contribution of the dispersive media and provided a unique opportunity to probe the IPT during both flybys.

5.2.3 Io Plasma Torus

The volcanic eruptions of Io launch ionized particles with a velocity high enough to start orbiting around Jupiter, interacting with its strong magnetic field. The result is a toroidal cloud of plasma, centred in the centrifugal equator of Jupiter at Io's orbital distance, that introduces a path delay and a carrier frequency shift on radio frequency signals. This phenomenon was first detected by ground-based observations [59].

The Io Plasma Torus is composed mainly of different ion species : S+, S2+, S3+, O+, and O2+, with $\sim$ 10% of protons [15], [74].

Classically, the torus has been divided in three different regions, the cold torus, the ribbon and the warm torus [17], that are coincident with the three peaks of the radial profile measured by in-situ observations of the electron density by the Voyager 1. The first peak, which corresponds to the cold torus, is found at about 5.3 R_J from Jupiter, where R_J corresponds to one Jupiter radius. Another peak is located at about the Io-Jupiter radial distance and corresponds to the ribbon. Finally, at 6 R_J we find the last peak, that can be attributed to the warm torus. The electron density decreases with both radial and transverse distance from the centrifugal equator as is reported in figure 5 of [15].

The available measurements has been used by [80] to develop a parametric model of the IPT, fitting its electron density distribution with four Gaussian shapes, one for the cold torus, one for the ribbon and two for the warm torus, given that the contribution of the warm torus cannot be represented with a single Gaussian curve. Then, the model was extended beyond the centrifugal equator with another Gaussian shape, obtaining:

$$\begin{aligned} N(R < 6.1R_j, r) &= N_1 e^{-\frac{(R-C_1)^2}{(W_1)^2}} e^{-\frac{r^2}{H_1^2}} + N_2 e^{-\frac{(R-C_2)^2}{(W_2)^2}} e^{-\frac{r^2}{H_2^2}} + N_3 e^{-\frac{(R-C_3)^2}{(W_3)^2}} e^{-\frac{r^2}{H_3^2}} \\ N(R > 6.1R_j, r) &= N_4 e^{-\frac{(R-C_4)^2}{(W_4)^2}} e^{-\frac{r^2}{H_4^2}} \end{aligned} \tag{5.4}$$

where N_i is the electron central density, C_i the peak location, W_i the width and H_i the scale height of the IPT and i=1 $\cdots$ 4 corresponds respectively to the cold torus, the ribbon, the warm and the extended torus. The model assumes longitudinal electron density symmetry and Norh-South symmetry in the centrifugal equator.

Figure 5.1 shows a visual representation of the IPT model, described by the equation 5.4, with a minor modification that forces the electron density distribution to follow the Jupiter's magnetic field lines.

Being a dispersive medium, the IPT induce a non-dynamical Doppler shift on the radio frequency signals. Due to the orbital geometry of Juno, the radio frequency signals crosses the IPT, yielding an increased path delay, that, if not properly calibrated, can be a potential source of bias in the Jupiter estimated gravity field coefficients.

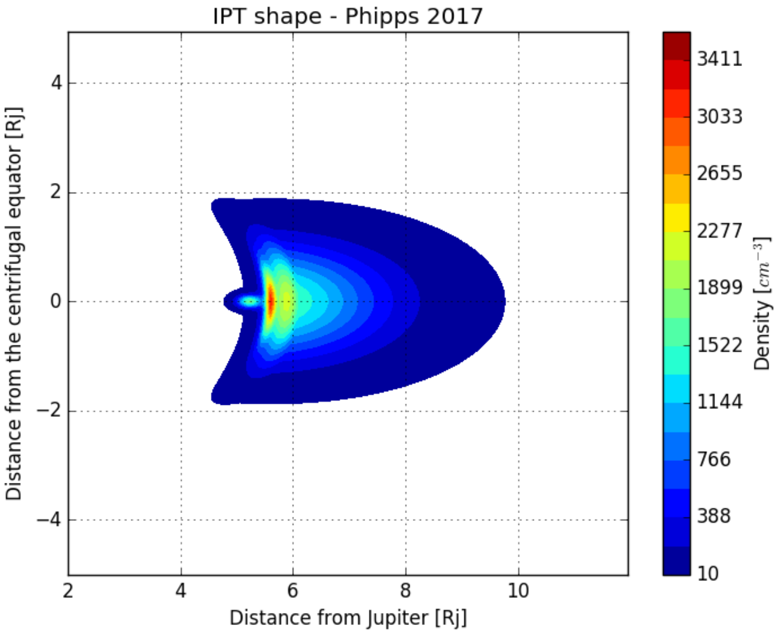

Figure 5.1 – Radial section of the Io plasma torus generated using the values of [80]. In the plot the four different zones of the IPT can be easily identified.

The first perijove pass, PJ1, procured a unique opportunity to study the IPT. A direct measurement of the downlink plasma contribution was possible by transmitting downlink signals at X and Ka-band coherent with a common X-band uplink [66]. This particular configuration has been encountered again during PJ13, when the DSS-25 was down for maintenance an the Ka band in uplink was not available.

For the other perijoves, the dual-frequency calibration has been applied extracting the dispersive contribution. While for PJ01 the IPT shape is really clear, during the other perijoves the path delay signal is not returning to zero, and more over, in some perijoves the calibration was not able to reduce the noise, see table 5.1, suggesting that there is an unknown dispersive effect different on X/X and Ka/Ka that is displayed using the dual-frequency calibrations. Most likely, this effect is an uplink station delay in the Ka band in the DSS-25. Currently, more investigations on the origin of this problem are ongoing.

In order to determine how accurate is the correspondence between the extracted path delay of the different perijoves and the expected path delay due to the IPT model defined by equation 5.4, we followed the next steps:

The electron density computed using the model described by 5.4, has been integrated along the line-of-sight of the S/C in order to extract the total electron content (TEC).

$$TEC = \int N dl \tag{5.5}$$

Once the TEC was obtained, the path delay follows:

$$\Delta l = -k\frac{TEC}{f^2} \tag{5.6}$$

Where $k = 40.3\ m^3/s^2$ and f, in Hz, is the transmitted frequency. Finally, we computed the dispersive effect of the IPT in terms of Doppler-shift as:

$$\Delta F = (1 + \frac{1}{M_2^2})M_2\frac{f_0\dot{\Delta l}}{c} \tag{5.7}$$

Where M_2 represents the turn-around ratio of the S/C and c the velocity of the light.

Figure 5.2 shows the comparison between the extracted path delay and the computed path delay using the IPT model. The obtained path delay in PJ1 and PJ13, extracted using the single-calibration link, seems to follow approximately the IPT model computed by means of [80]. This suggests that the IPT can be effectively calibrated removing the residuals signatures, and therefore, the model can be improved. In the other perijoves we do not see a clear correspondence between the model and the obtained path delay, implying an already cited unexplained dispersive effect.

Estimation technique

With the objective of obtaining a better estimation of the IPT shape and density for each perijove and study its variability in time, an estimation procedure using MONTE capable to tune the parametric model of [80] has been developed. To do that, we used a batch weighted least squares estimation technique, introduced in section 2.2, that minimizes the sum of squares of the residuals, computed as the difference between the measured plasma in downlink, extracted using the single-frequency-link technique during PJ1 and PJ13, and the plasma computed using the model defined in [80].

The solve-for parameters are:

- Electron central density of the cold torus, the ribbon, the warm and the extended torus.
- Peak locations of the central density for the four zones that conform the model.
- Widths of the torus zones.
- Scale heights.
- Right ascension and declination of the centrifugal equator frame.

The results are summarized in the table 5.2, while figures 5.3, 5.5, 5.4 and 5.6 report the results obtained for PJ1 and PJ13 respectively. However, the associated uncertainties, not shown, are pretty large mostly due to the large non-linearity of the reference model and the large number of the estimated parameters. Further studies could improve the obtained results using better models and applying constraints between the estimated parameters.

PJ1 The tuned model seems to follow the extracted plasma better than the original model. In the path delay plot, we see an increasing trend starting from 0 mm and finishing about 120 mm superposed to the IPT signature, that can be explained by the solar plasma.

Using the best estimated values of the IPT parameters and introducing them in equation 5.4 we can generate a radial profile of the IPT. When comparing the estimated profile, figure 5.5, with figure 5.1 that corresponds to the original model, computed with data obtained by Voyager 1 in 1979, a major difference is displayed, pointing that during PJ1 the cold torus got merged with the ribbon. Also we noticed a slightly electron density increase in the warm torus.

PJ13 For PJ13, the agreement between the tuned model and the extracted plasma is slightly worse than in the PJ1 case, see figure 5.4. The extracted plasma shows a collapse that cannot be absorbed by the model.

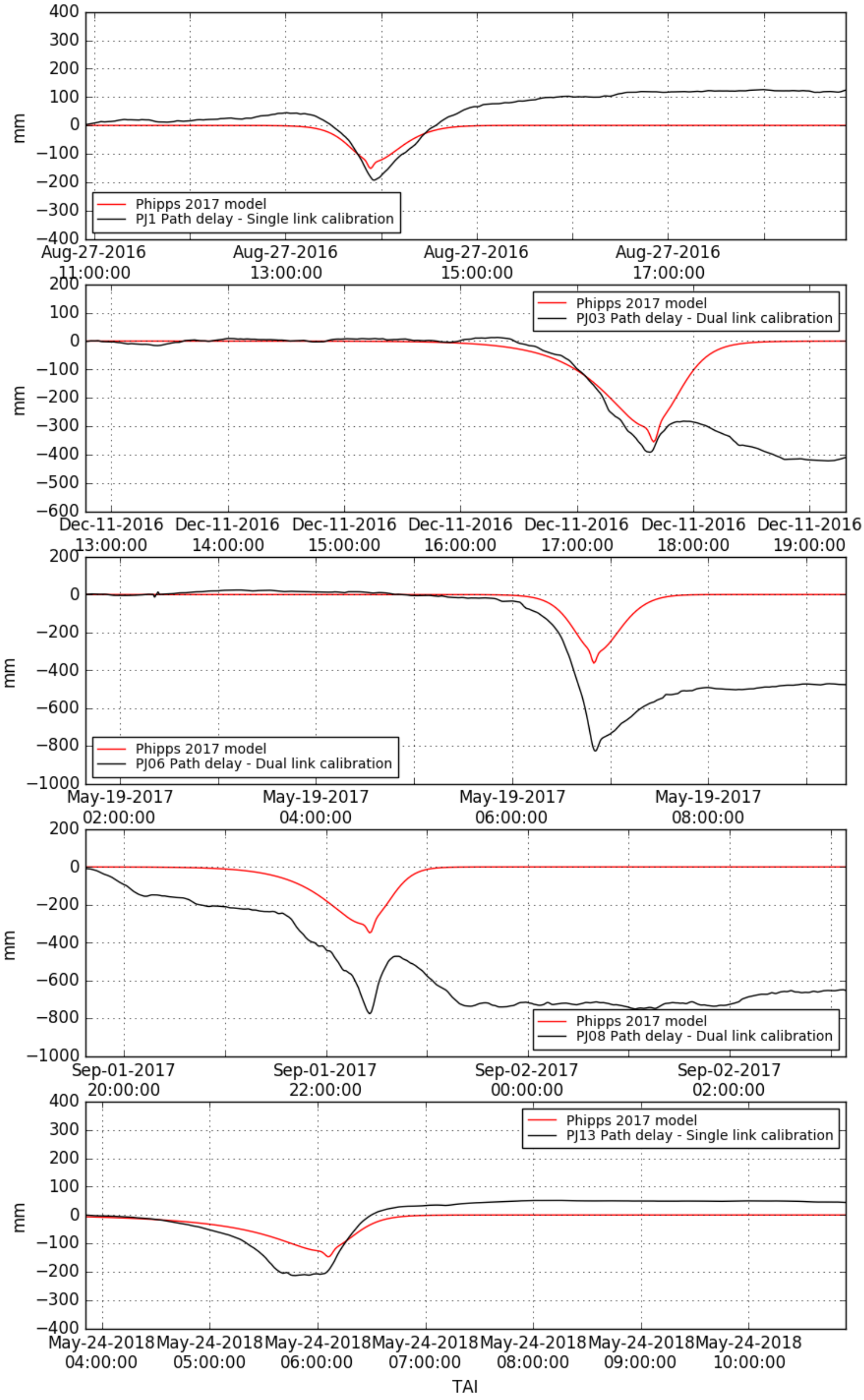

Figure 5.2 – Path delay of the different PJ's obtained using the multi-frequency link calibration. The red line corresponds to the model defined by equation 5.4

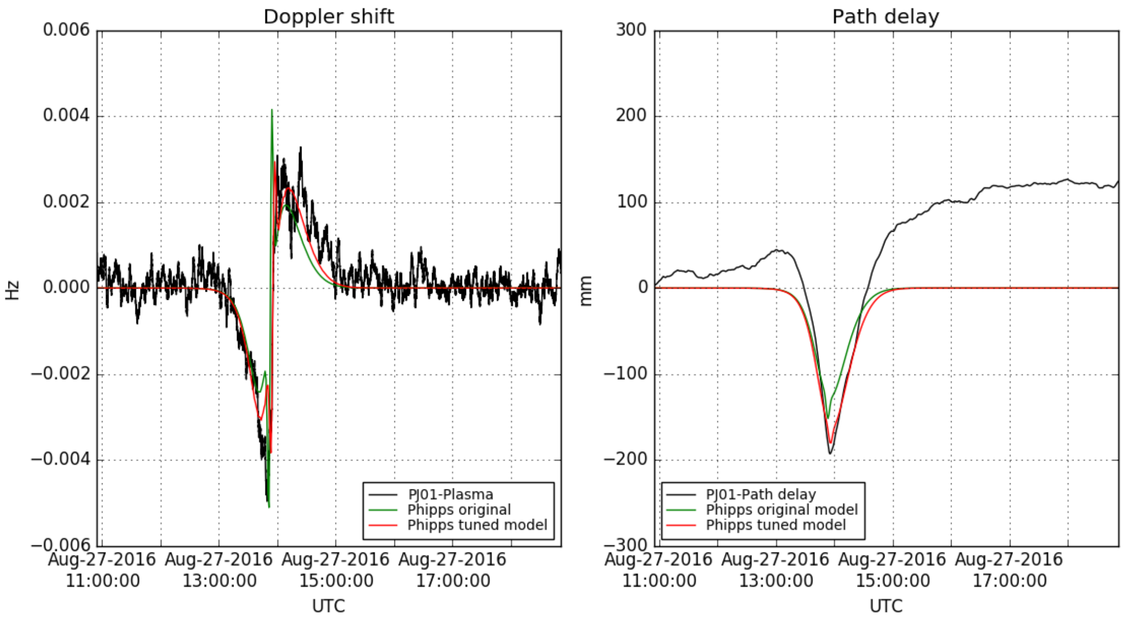

Figure 5.3 – Plasma noise and path delay extracted during PJ1 (black) compared against the expected values using the reference model (red) and the computed ones using the estimation technique (green).

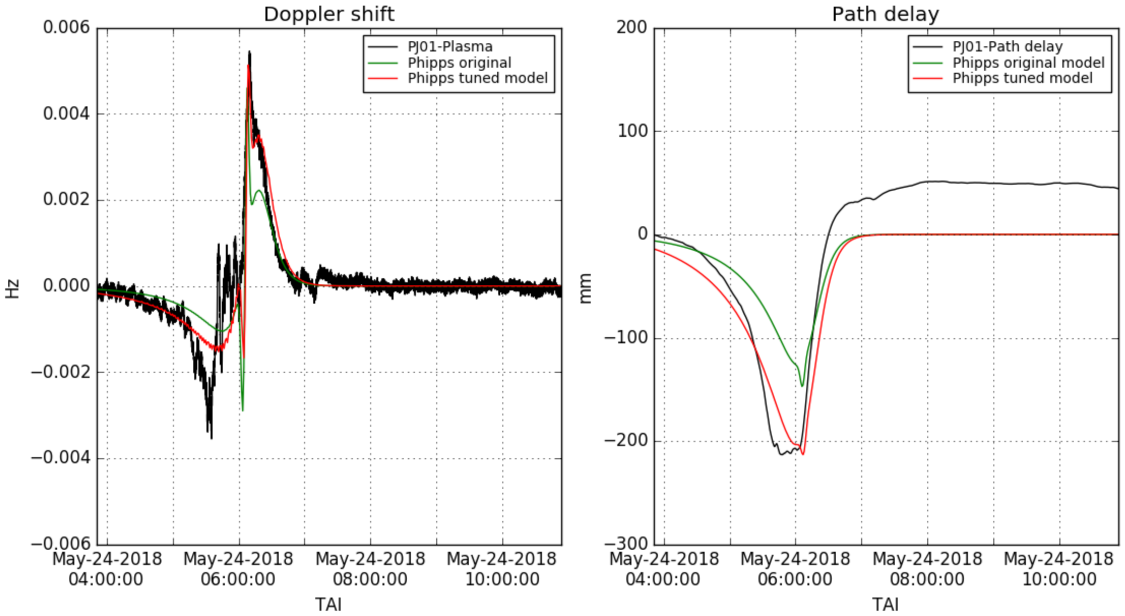

Figure 5.4 – Plasma noise and path delay extracted during PJ13 (black) compared against the expected values using the reference model (red) and the computed ones using the estimation technique (green).

In the extracted path delay, we see a strange plateau close to the minimum, not predicted by the model. The path delay remains at 40 mm after the signature caused by the IPT, this last effect could be also explained by the solar plasma.

The IPT shape, shown in figure 5.6, is not only different with respect to the original model profile but strong differences stand out when compared against the IPT shape generated with the estimated coefficients during PJ1. The four regions of the torus are clearly differentiated, the cold torus can be identified, the warm torus is 1 R_J larger than in the PJ1 case and the electron densities of the different torus zones are more diffuse.

Table 5.2 – IPT, nominal and estimated parameters. i=1 indicates the cold torus, i=2 the ribbon, i=3 the warm torus and i=4 the extended torus.

Parameter	Phipps-2017	Juno-PJ1	Juno-PJ13
Data acquisition	March 1979	August 2016	May 2018
C_1 (Rj)	5.23	5.84	5.15
C_2 (Rj)	5.60	5.62	5.61
C_3 (Rj)	5.80	5.93	5.98
C_4 (Rj)	5.53	5.70	7.09
N_1 (Rj)	1710	1297.19	1505.52
N_2 (Rj)	2180	2249.68	2143.24
N_3 (Rj)	2160	2312.38	2137.87
N_4 (Rj)	1601	2059.80	1545.76
H_1 (Rj)	0.1	0.111	0.107
H_2 (Rj)	0.6	0.555	0.601
H_3 (Rj)	1.0	1.012	1.00
H_4 (Rj)	1.0	1.134	0.85
W_1 (Rj)	0.2	0.199	0.199
W_2 (Rj)	0.08	0.08	0.080
W_3 (Rj)	0.32	0.320	0.320
W_4 (Rj)	1.88	1.887	1.877
Ra_{ceq} (deg)	159.2	159.2	159.1
Dec_{ceq} (deg)	83.6	82.95	83.99

This seems to evidence the variability of the IPT and suggests that the model developed by Phipps works well as a first approximation, but could be improved taking into account the time and the longitudinal variability. Another major input will be data from other close encounters with Jupiter, that will be available once the issue of the dual-link calibration, in the gravity perijoves, will be figured out.

5.2.4 Juno data analysis, multi-arc setup

Juno is currently orbiting Jupiter in a highly eccentric, 53.5-day orbit, with a perijove altitude of about 4000 km, after 5 years of cruise from the Earth. During each perijove pass, Doppler measurements between Juno and the Earth are acquired at the DSN for about eight hours centred around Jupiter's closest approach. Reconstructing Juno's trajectory during its close encounters with Jupiter, allowed us to retrieve a measure of the gravity field of the gas giant.

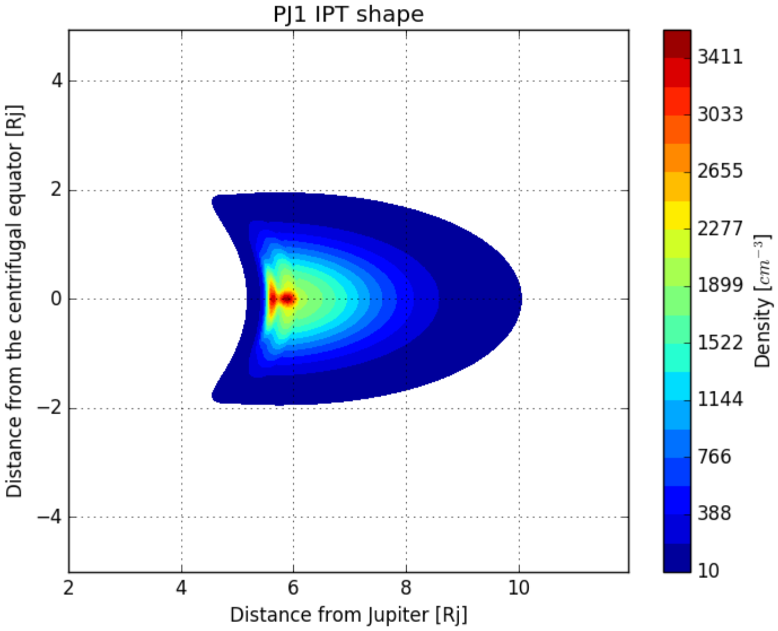

Figure 5.5 – Io plasma torus radial section shape using the estimated values for PJ01.

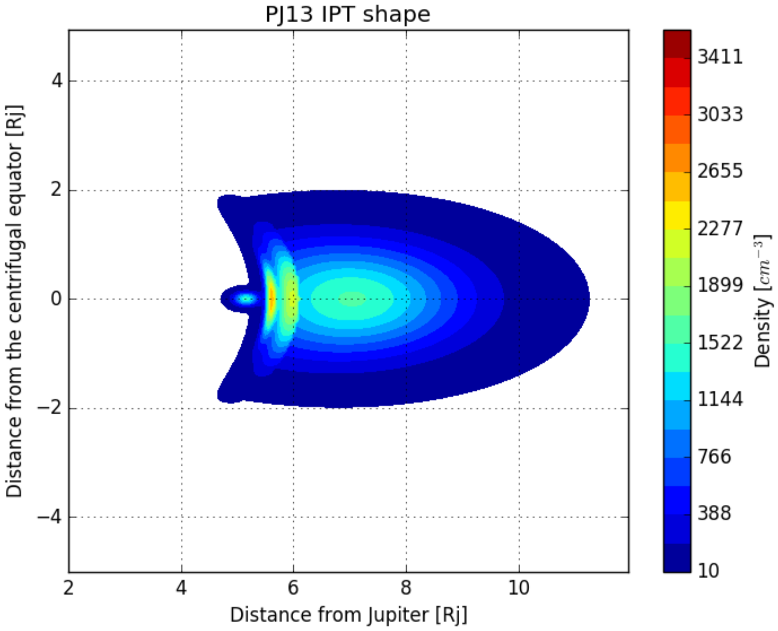

Figure 5.6 – Io plasma torus radial section shape using the estimated values for PJ13.

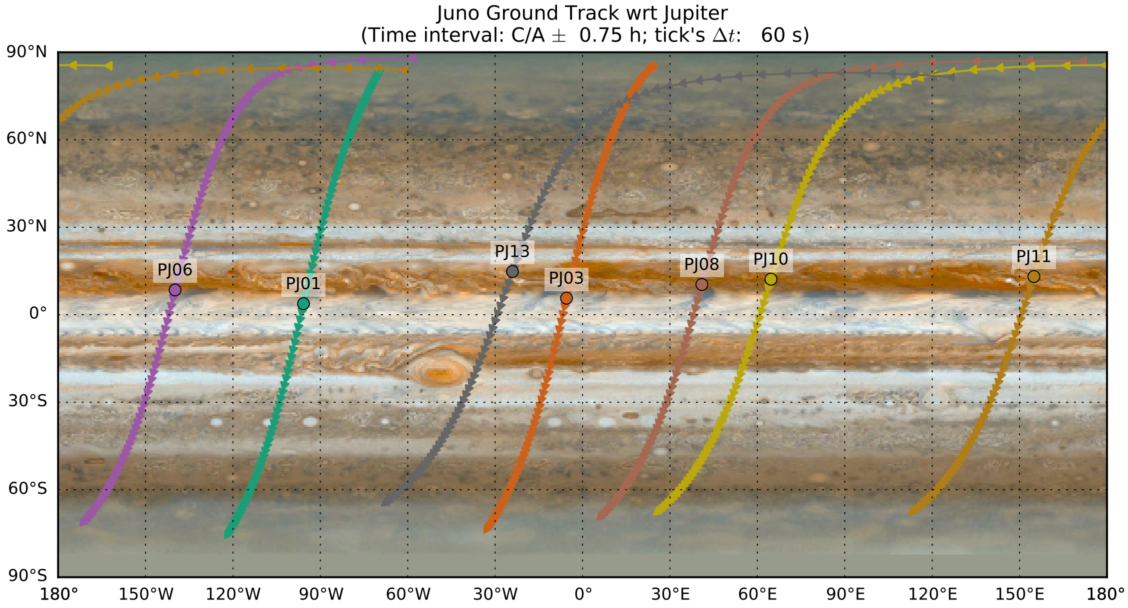

Figure 5.7 – Ground tracks of the flybys performed by Juno over Jupiter.

Multi-arc setup

The radio tracking data of PJ1, PJ3, PJ6 and PJ8 were pre-processed, multi-frequency link calibrations were applied to prevent for the plasma noise, and the residuals were weighted on a pass-by-pass strategy using the RMS of the residuals themselves.

The least-squares information filter solved for:

- Initial state of Juno at the beginning of each arc.
- Initial state of Jupiter barycentre at the beginning of the first arc (PJ1).
- GM of the Jupiter barycentre.
- Jupiter's zonal harmonics up to degree 24th.
- Jupiter's quadrupole.
- Jupiter's tidal response ($Re(k_{22})$).
- Jupiter's pole position and rate.
- Additionaly, the solar radiation preassure was considered at 20%.

Initial state of Juno The state vector of Juno at the beginning of each arc, approximately one day prior to the C/A, is a local parameter of the multi-arc approach. The a-priori values are obtained from the trajectory reconstructed by the Juno Navigation team. In order to obtain an unconstrained solution we set the a-priori uncertainties for position and velocity to 1000 km and 0.01 km/sec, respectively.

Initial state of Jupiter Barycentre Given the high accuracy of the Doppler observables, we integrated, and updated, the Jupiter planetary ephemerides to take into account possible errors on Jupiter's position. The a-priori values were taken from the planetary ephemerides DE435 and as a-priori uncertainty we used 1000 km in every direction and 1 km/s respectively.

GM of the Jupiter barycentre The GM of Jupiter's barycentre is retrieved from the JUP310 ephemerides set, estimated, mainly, by the study of the orbit evolution of the Galilean satellites, with a large a-priori uncertainty of 2.8 km^3/sec^2.

Jupiter gravity field coefficients The gravity field of a gas-giant is expected to be dominated by the even zonal harmonics. In our multi-arc setup, we included all even and odd zonal harmonics up to the 24th degree, to take into account for the possible zonal winds. The a-priori uncertainties were set using large values in order to not constraint the solution. The quadrupole coefficients ($C_{21}, S_{21}, C_{22}, S_{22}$) were set to zero with large a-priori uncertainties. These parameters were added to take into account possible deviations between the rotation axis and the principal axis of inertia.

Jupiter's tidal response Jupiter's tidal response was estimated, with an a-priori uncertainty of 0.8. Higher order Love numbers were set to the values reported in [88]. The imaginary parts of the love numbers were set to zero due to the low number of passes, subsequent perijoves might report information about the imaginary part of the k_{22}.

Table 5.3 – Main orbital, geometrical and quality data characteristics of the Juno flybys used in the gravity experiment. These values are referred to the C/A.

		PJ1	**PJ3**	**PJ6**	**PJ8**
Date (ERT)	(ET)	27-08-16, 12:51	11-12-16, 17:04	19-05-17, 06:01	01-09-17, 21:49
Altitude	(km)	4140.73	4103.89	3385.52	3334.89
Relative Velocity	(km/s)	59.27	59.36	59.88	60.17
Latitude	(deg)	3.78	5.66	8.49	10.38
Longitude	(deg)	−95.77	−5.50	−139.84	40.95
SEP Angle	(deg)	22.63	61.57	135.41	42.53
Inclination	(deg)	102.77	103.03	104.00	105.09
Number of points		441	661	658	487
RMS	(μm/s)	112.2	19	31.5	20.9

Pole position and rate The pole position, right ascension and declination and its variation in time, has been estimated at a reference epoch (J2000) with large a-priori uncertainties.

5.2.5 Results

Solving the orbit determination problem using range-rate data from four different encounters, PJ1, PJ3, PJ6 and PJ8 allowed us to measure the gravitational coefficients of Jupiter up to the 10th degree. Nevertheless, the quadrupole and zonal coefficients up to the 24th degree, both statistically zero, were added to the estimation process in order to obtain a satisfactory fit without signatures in the vicinity of the C/A.

Figure 5.8 report the obtained Doppler residuals at an integration time of 60s, evidencing the low RMS of the solution, being $19\mu m/s$ the lowest RMS obtained in PJ3 and $112\mu m/s$ the highest RMS obtained during PJ1. This RMS value during PJ1 can be explained due to the low SEP of the pass, in addition to the lack of Ka-band in uplink. Table 5.3 summarizes the characteristics, both data and geometry, of the different flybys used during our analysis. The estimated gravity coefficients along with their associated uncertainty can be found in table 5.4.

The integration of the planetary ephemerides allowed to take into account possible errors in Jupiter's position. This iterative process allowed to retrieve a quadrupole field compatible with zero within 2-σ, as expected for a gas giant. In addition, the estimation of the Love number k_{22} retrieved a value compatible with the theoretical values [88].

The solution confirms that, as expected, the gas giant gravity field is dominated by the even zonal coefficients. The analysis allowed to measure, for the first time, the odd zonal coefficients, being an indication of the hemispherical gravity field asymmetry, probably due to the dynamical signatures of the zonal winds. The measured odd zonal coefficients suggest that the zonal winds extend down to 3000 km [52]. In addition, an analysis of the even zonal harmonics indicate that the interior of Jupiter rotates nearly as a rigid body [37].

Figure 5.10 reports the gravity spectra of the solution, showing the value of the different coefficients and its 1-σ associated uncertainty, showing the great accuracy obtained in the estimated low degree harmonics, up to the 10th degree.

To assess the stability of the solution, the final multi-arc solution has been compared

Table 5.4 – Jupiter gravity field estimated from PJ01+PJ03+PJ06+PJ08 compared against [45].

		Apriori	Iess-2018 PJ3+PJ6	This work PJ1+PJ3+PJ6+PJ8
GM	(km^3/s^2)	126712764.1±2.8	126712764.14±2.8	126712764.2±2.8
J_2	$(\times 10^6)$	14697±30	14696.5722±0.0047	14696.5664±0.0017
J_3	$(\times 10^6)$	−0±18	−0.0424±0.0032	−0.0480±0.0018
J_4	$(\times 10^6)$	−587±41	−586.6092±0.0013	−586.60748±0.00078
J_5	$(\times 10^6)$	−0±23	−0.0690±0.0027	−0.0717±0.0015
J_6	$(\times 10^6)$	34±49	34.1980±0.0030	34.2002±0.0020
J_7	$(\times 10^6)$	0±27	0.1239±0.0056	0.1192±0.0037
J_8	$(\times 10^6)$	−2±56	−2.4258±0.0082	−2.4230±0.0061
J_9	$(\times 10^6)$	−0±30	−0.106±0.015	−0.108±0.011
J_{10}	$(\times 10^6)$	0±62	0.172±0.023	0.171±0.018
J_{11}	$(\times 10^6)$	−0±33	0.033±0.037	0.043±0.030
J_{12}	$(\times 10^6)$	0±68	0.047±0.059	0.018±0.049
J_{13}	$(\times 10^6)$	−0±36	−0.005±0.087	0.045±0.072
J_{14}	$(\times 10^6)$	−0±73	−0.02±0.13	−0.12±0.11
J_{15}	$(\times 10^6)$	−0±38	0.01±0.17	0.14±0.14
C_{21}	$(\times 10^6)$	0±100	−0.0127±0.0050	−0.0064±0.0031
S_{21}	$(\times 10^6)$	0±100	−0.0027±0.0086	−0.0004±0.0018
C_{22}	$(\times 10^6)$	0±50	−0.0004±0.0027	0.0027±0.0013
S_{22}	$(\times 10^6)$	0±50	−0.0002±0.0036	0.00104±0.00071
k_{22}		0.559±0.8	0.625±0.021	0.57610±0.0149

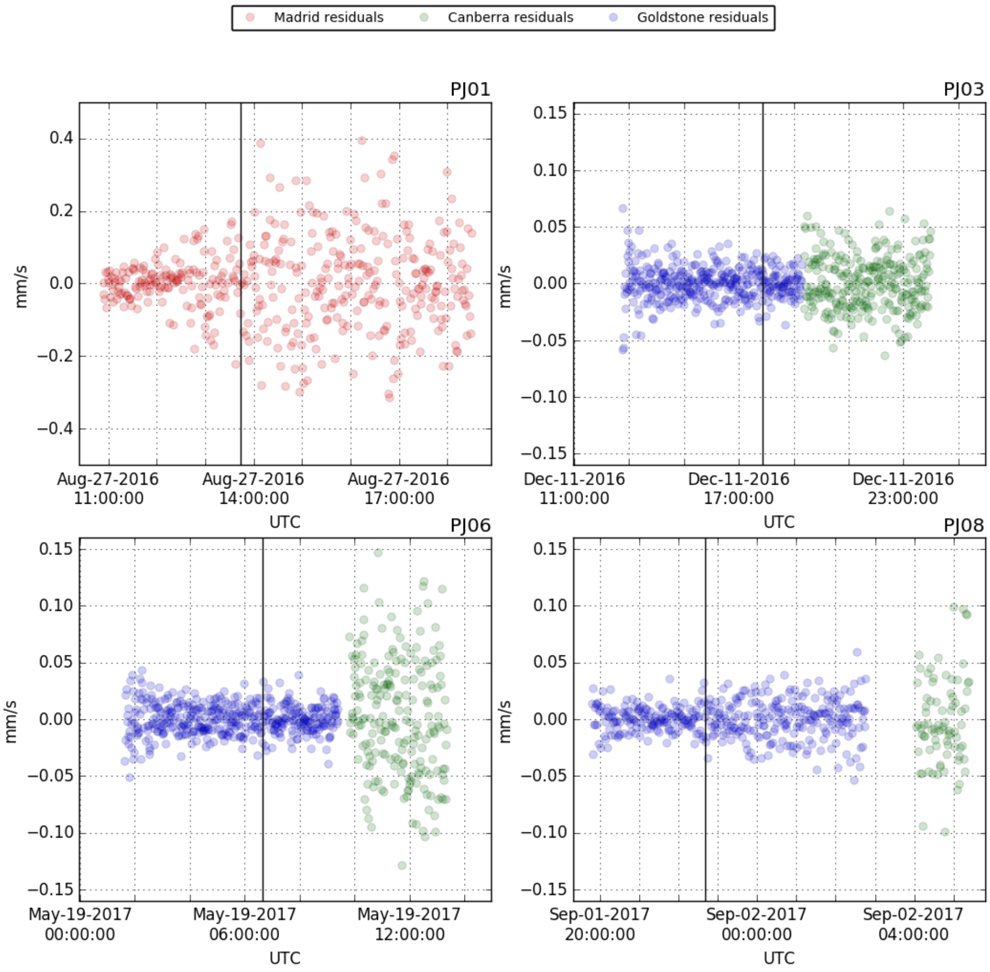

Figure 5.8 – Calibrated X-band Doppler residuals of PJ1, PJ3, PJ6 and PJ8. The vertical line corresponds to the closest approach.

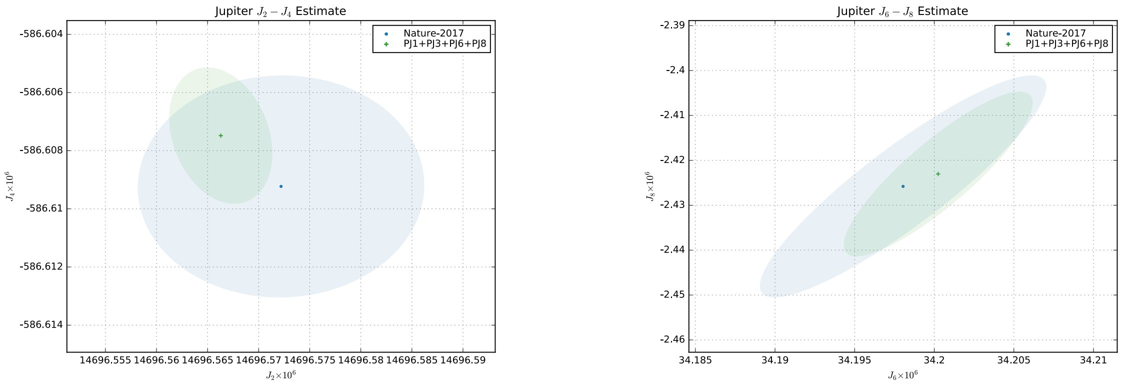

(a) Jupiter $J_2 - J_4$ estimate (b) Jupiter $J_3 - J_5$ estimate

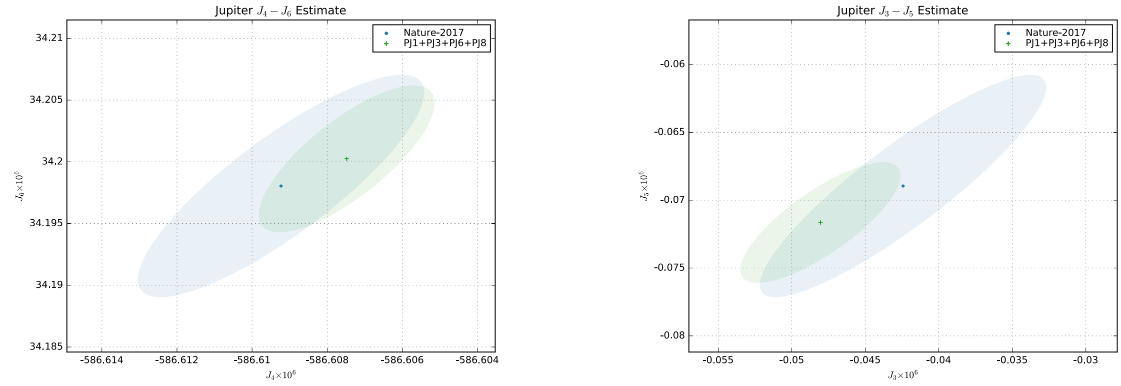

(c) Jupiter $J_4 - J_6$ estimate (d) Jupiter $J_5 - J_7$ estimate

Figure 5.9 – Multi-arc solution (PJ1+PJ3+PJ6+PJ8) compared against the last published solution [45] with the 3-σ error ellipses for the different pairs of the low degree gravity harmonics.

against the single-arc solutions, obtaining gravity coefficients compatible with them with less than 1-σ. Further more, we compared the obtained results against the last published result [45], as displayed in figure 5.9, evidencing the full agreement between the obtained results. As expected, the solution presents smaller uncertainties due to the addition of data of two more perijoves.

5.3 The Galilean satellites - Galileo data analysis

5.3.1 Why?

Galileo was an old mission that studied the Jupiter system for 8 years. The mission experienced several problems, as explained in [11] and [68], and despite that, it overcame them and provided a lot of new information of the Jupiter system that was unveiled by then, like the evidence of an ocean deep inside in Europa [25], the discovery of Ganymede's magnetic field [57] or the active volcanism in Io [63].

One of the questions that the reader may ask is, why would anyone want to do a

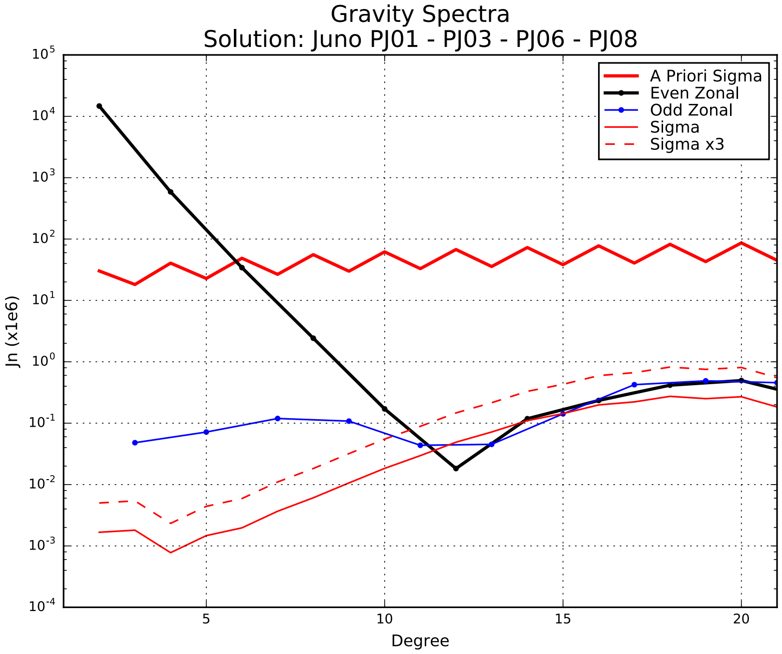

Figure 5.10 – Estimated non normalized zonal harmonics, both even and zonal, showing the great accuracy obtained for the low-degree harmonics.

re-analysis of the entire radio tracking data set of the Galileo mission?

There are several reasons that redeemed this analysis necessary:

New knowledge of the gravity field of Jupiter As made clear before, the gravity field of a central body defines the orbits of its satellites. An updated gravity field, potentially, constrains better the ephemerides of the satellite system. Thanks to the gravity science experiment of the Juno mission, a new updated gravity field solution is available. See section 5.2.4, [32], and [45].

Hydrostatic equilibrium In the published analyses of the gravity field of the Galilean satellites [4], [7], [3], [48] the hydrostatic equilibrium constraint, $J_2/C_{22} = 10/3$, was imposed due to the geometry of the flybys and the low data quality. Subsequent flybys, not analysed in the original analyses, may improve the global coverage allowing to retrieve a not-constraint gravity field.

Multi-arc method In some of the previous analysis of the gravity field of the Galilean satellites, the authors did not adopt a multi-arc method, but they provided a simple weighted mean of the single-arc results of the different flybys. This approach provides larger uncertainties because it doesn't take into account correlations between different parameters. The multi-arc method offers a new way to analyse the data and provide updates in the gravity solutions.

New models of the Io plasma torus Recently, re-analysis of the voyager data provided new models of the Io plasma torus, a source of dispersive noise that can potentially introduce a bias in the orbit determination results [80], [14].

All together conform a weighty reason to do a reanalysis and study the Jovian system.

This study, was carried out during a six-months research sojourn in the Jet Propulsion Laboratory, NASA, Pasadena, USA, under the supervision of Kamal Oudrhiri, group supervisor of the Radio Science group.

5.3.2 Galileo Dynamical Model

Gravitational accelerations

In our dynamical model, the sources of the gravitational forces are all the main bodies of the solar system, the sun, the solar system planets, the Saturn satellites and the rings of Saturn. In particular, the following effects were activated:

- Relativistic point-mass gravity acceleration from the Sun, the planets, the Moon and Pluto. The state vectors were obtained from JPL planetary ephemerides DE435.
- Relativistic point-mass gravity acceleration from Jupiter. The state vector was obtained from JPL's Jupiter ephemerides JUP310.
- Newtonian point-mass gravity acceleration from the Jupiter's satellites Amalthea, Io, Ganymede, Europa and Callisto. The state vectors were obtained from the JPL Saturn's system ephemerides JUP310.
- The gravity field of Jupiter, represented by the standard spherical harmonic expansion of its gravitational potential up to the twentieth degree. Result from the gravity analysis of Juno. See section 5.2.
- The gravity field of the main Galilean satellites, represented by means of the spherical harmonic expansion, retrieved from the last publications of the RS Team.
- Tides risen on Jupiter by its satellites.
- The self-oblateness of Jupiter's satellites.

Rotational models Just as we did for the satellites of the Saturn system, we adopted a dynamically defined, perfectly synchronous, rotational model pointing to the empty focus of the orbit. For Jupiter we used the rotational model of the ephemerides set JUP310, defined by 5.1, 5.2 and 5.3.

Non gravitational accelerations

As explained before, the non-gravitational forces acting on the S/C are forces that only affect the propagation of the trajectory of the spacecraft. The following accelerations were active in our setup:

- The solar radiation pressure, function of the thermo-optical coefficients of the S/C.
- The acceleration product of the radioisotope thermal generators (RTG's).

Missing data

While doing our analysis, we encountered several data availability problems and a general lack of information on the models used almost two decades ago to perform the navigation of the Galileo S/C. Specifically:

- Atmospheric calibrations.
- OTM's, SMFDV and mass history.
- Details of the S/C shape and the thermo-optical properties of their surfaces.
- Information on the RTG's non-gravitational acceleration.
- Some C/A missing data due to the S/C entering in safe modes.
- Ranging data.
- Missing data in the Galileo attitude kernels.
- IPT calibrations used during the original analysis.

Missing atmospheric calibrations The ionospheric calibrations, S/C dependent, generated by dual frequency GPS measurements, were not available during the time period between October of 1999 and December of 2002, potentially introducing dispersive noise in the results affecting the following flybys: I24, I25, I27, I31, I32, and I33, E4 and E6, G28 and G29, and C30.

Missing OTM, SMFDV, and mass history To perform the navigation of Galileo, three OTM were planned for each orbit around Jupiter, to account for small adjustments of the orbit. The manoeuvres were designed to be executed three days before and after each C/A and covered by eight hours of continuous F2 tracking data [11]. Due to the HGA failure and the need of science data return, this optimal situation was not consistently available. Data of the performed manoeuvres were only available up to the 10th flyby of the mission [39]. To overcome this issue, we cut all the data around 30 hours before and after the C/A of each encounter looking for sudden steps in the pre-fit data, which could indicate the presence of a SMFDV. Given that the Galileo S/C did not have reaction wheels, all the attitude manoeuvres were performed using the thrusters, so some of them could be retrieved looking at the attitude data, when it was available.

The absence of a mass history was overcome using a linear interpolation between the estimated mass that the S/C had after the Jupiter orbiter insertion (1612kg) and the final mission mass (1298kg) [18], [68].

S/C shape The lack of general input navigation file (GINFILE/GINLOCK) entailed the issue of not having a precise S/C model. We developed our own S/C model using photos and schemes found in the literature [68]. The adopted model, summarized in the figure 5.11, is the following:

- S/C Dish of 2.37 m of radius and 0.99 m of depth.
- The main body and the scan platform was modelled using a cylinder of 3.8 m of length and 1 m of radius.

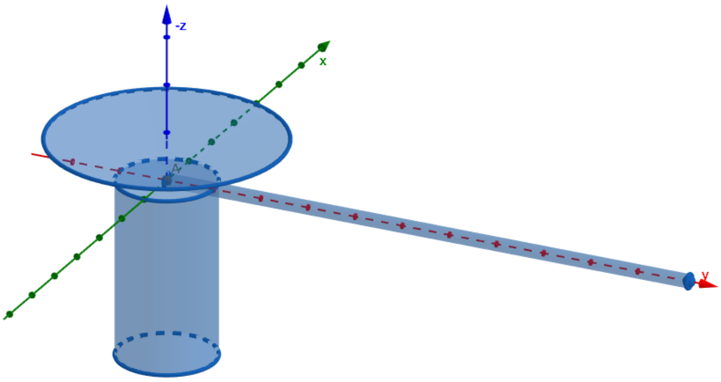

Figure 5.11 – Schematic diagram of the S/C shape in the S/C frame used in our analysis. The Y direction is coincident with the magnetometer boom while the -Z direction coincides with the antenna pointing to the earth.

- The magnetometer boom was modelled using a cylinder of 11.678 m of length and 0.14 m of radius.

For all the components we considered a specular reflection of 0.00245 and a diffusive reflection of 0.0258, [11].

RTG Not having a GINFILE implied that we did not have an a-priori estimation of the RTG non-gravitational acceleration that affected the S/C during its mission. [11] reports that the Galileo navigation-team detected the RTG acceleration induced on Galileo, to be consistent with 0.4 nm/s^2, before the tour began. The problem was surpassed adding to the estimation filter the acceleration on the three components X,Y,Z in the S/C frame, modelled using the exponential model 4.4.

Range data After the HGA deployment failure, it was found that the S-Band signal was not able to support ranging data, so range data was not available during the whole mission [84].

Missing data in the attitude kernels While checking the coverage of the Galileo attitude kernels, numerous intervals without data were found. No more information about this issue were available, but it was probably caused by the reduced downlink data-rate caused by the HGA failure. This issue was resolved interpolating the data of the attitude files with a step capable to cover the missing-data intervals. The following flybys were affected by this issue: G1, G7, G28 and G29, E4, E6, E11, E12, E14, E16 and E19, C3, C9, C20, C22 and C30 and I24, I25, and I31.

Io plasma torus original corrections During our analysis we found that the Io plasma torus can potentially bias the OD solution, see section 5.3.4. The original calibrations of the IPT, that the NAV team used (personal communication of R.Haw, former navigator of Galileo), were not available. As we explain in the section 5.3.4, this fact became an issue in some encounters with Io.

5.3.3 Data-Selection and Calibration

During the flybys of Galileo of the natural satellites of the Jupiter system, Doppler data at S band (2.3 Ghz) were acquired by the 70-m antennas of the DSN at the three complexes of Madrid, Goldstone and Canberra. Just as we did with Cassini, we used all the available data, up to 30 hours before and after the close encounter. For the same reasons explained in section 4.3, we preferred F2 over F3, when available. When F3 were used, we added a bias in the estimation filter to take into account the possible inter-station clock offset. All the data were compressed to 60s and we only used data above 15 degrees of elevation. When available, calibrations of the ionosphere and troposphere effect were used. As explained before, ionospheric calibrations were not available for all the close encounters. In addition to the Earth ionosphere and troposphere, and the solar plasma, the Galileo tracking data were highly affected by a huge source of dispersive error, the IPT. Unfortunately, the original IPT corrections were not available and due to the HGA-deployment failure, the multi-frequency link technique could not be applied. To overcome this issue a numerical simulation has been carried out to unveil the potential effect of the IPT during the Galileo mission. (See the following section 5.3.4).

5.3.4 Io Plasma Torus during the Galileo mission

While doing the pre-processing of the Galileo data, we found non-modelled signatures in the flyby residuals, which could be explained by the IPT. To validate our hypothesis, we generated the expected frequency shift in the Doppler data, acquired during the close encounters with the Galilean satellites, due to the induced dispersive signature of the IPT, as previously explained in section 5.2.3. Then, the predicted signatures were compared against the un-modelled artifacts found in the residuals.

As can be seen in the figures 5.12, 5.13, 5.14, 5.15, 5.16, 5.17, 5.18 and 5.19, the signatures follow approximately the parametric model of the IPT, but not precisely. In some flybys the model follows better the signatures, just like I31 and I32. Instead, others encounters present a less accurate correspondence between the model and the signatures, like I24. For the sake of understanding better the geometry that the Galileo S/C followed during the encounter, the figures also show the trajectory of Galileo in the centrifugal frame, a projection in the centrifugal equator and in a radial section of the IPT, together with the tracking passes of the S/C.

The fact that the signatures do not follow exactly the model can be explained by errors in the parametric model. The model is a simplification and assumes a longitude-symmetry in the electron density distribution. Could also be explained by the IPT time variability, in density and ion composition, due to the highly variable volcanic activity of Io [76], [85]. It is reported in [13] that during the first Io encounter, the plasma densities observed by Galileo were approximately a factor of two higher than the voyager values, indeed the model used was built fitting the data acquired by Voyager 1 in March of 1979 [17].

However, the residuals of the Io encounters might be partially explained by the lack of ionospheric calibrations, another dispersive noise that affect especially the data at low-elevations.

We conclude that the un-modelled signatures found in the arcs are caused mainly by the non-dynamical dispersive signature of the IPT and that the model limitations prevent us from generating corrections of the IPT in order to complete the gravity analysis.

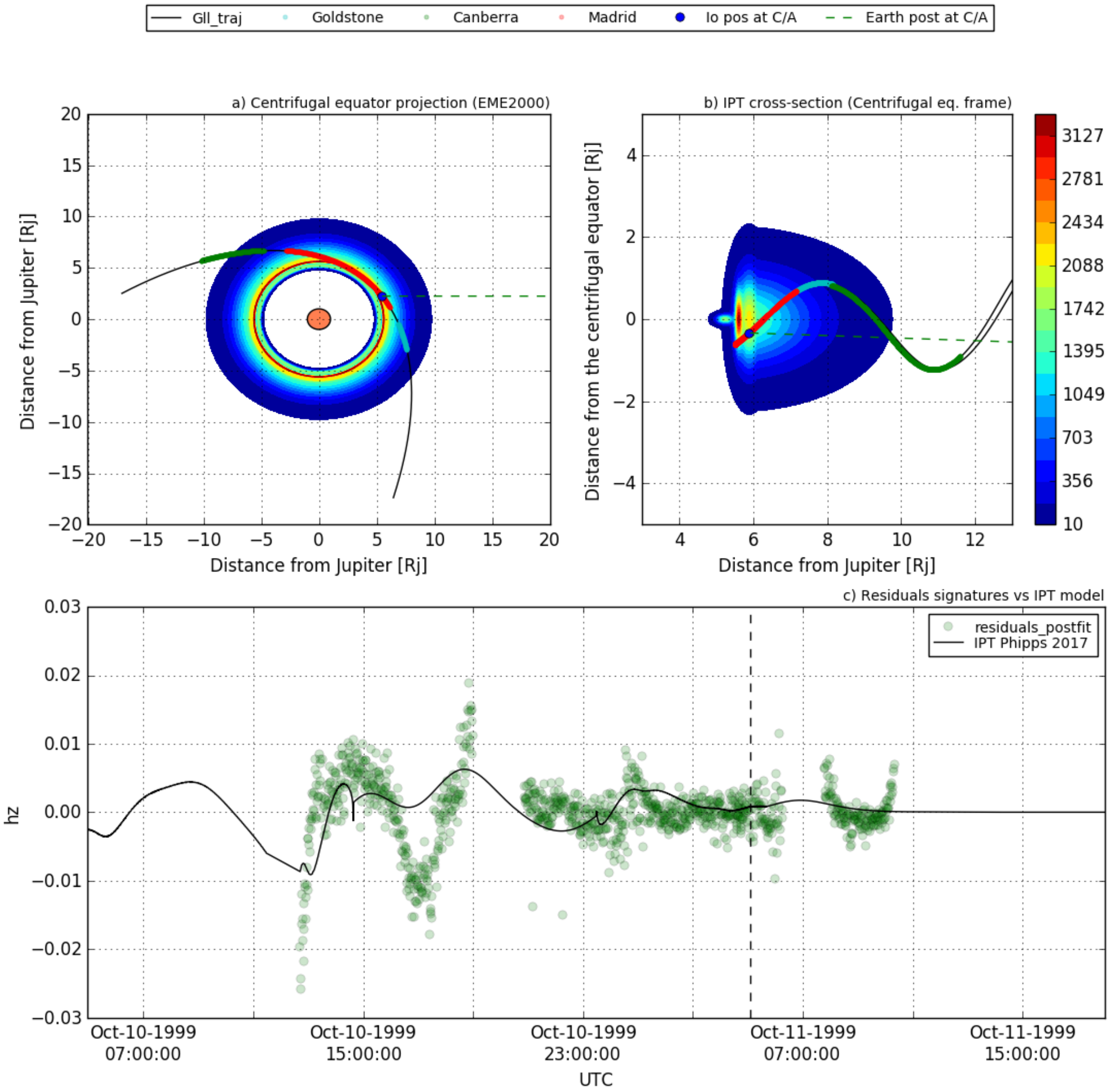

Figure 5.12 – IPT during I24: a) Centrifugal equator projection in EME2000. b) Radial section of the IPT. c) Found signatures against the expected Doppler-shift induced by the IPT, evidencing a poor agreement between the model and the retrieved signatures.

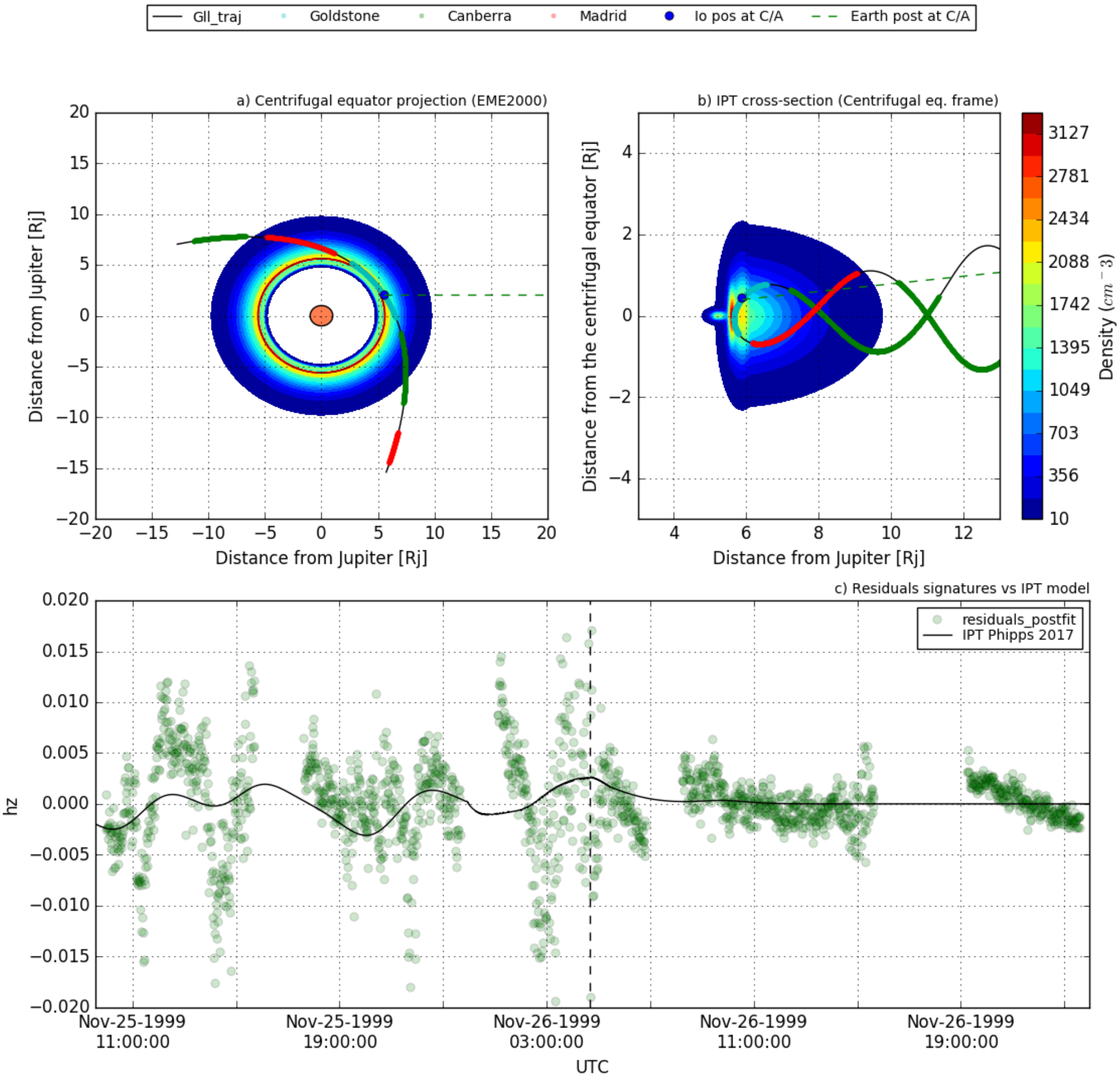

Figure 5.13 – IPT during I25: a) Centrifugal equator projection in EME2000. b) Radial section of the IPT. c) Found signatures against the expected Doppler-shift induced by the IPT, evidencing a poor agreement between the model and the retrieved signatures.

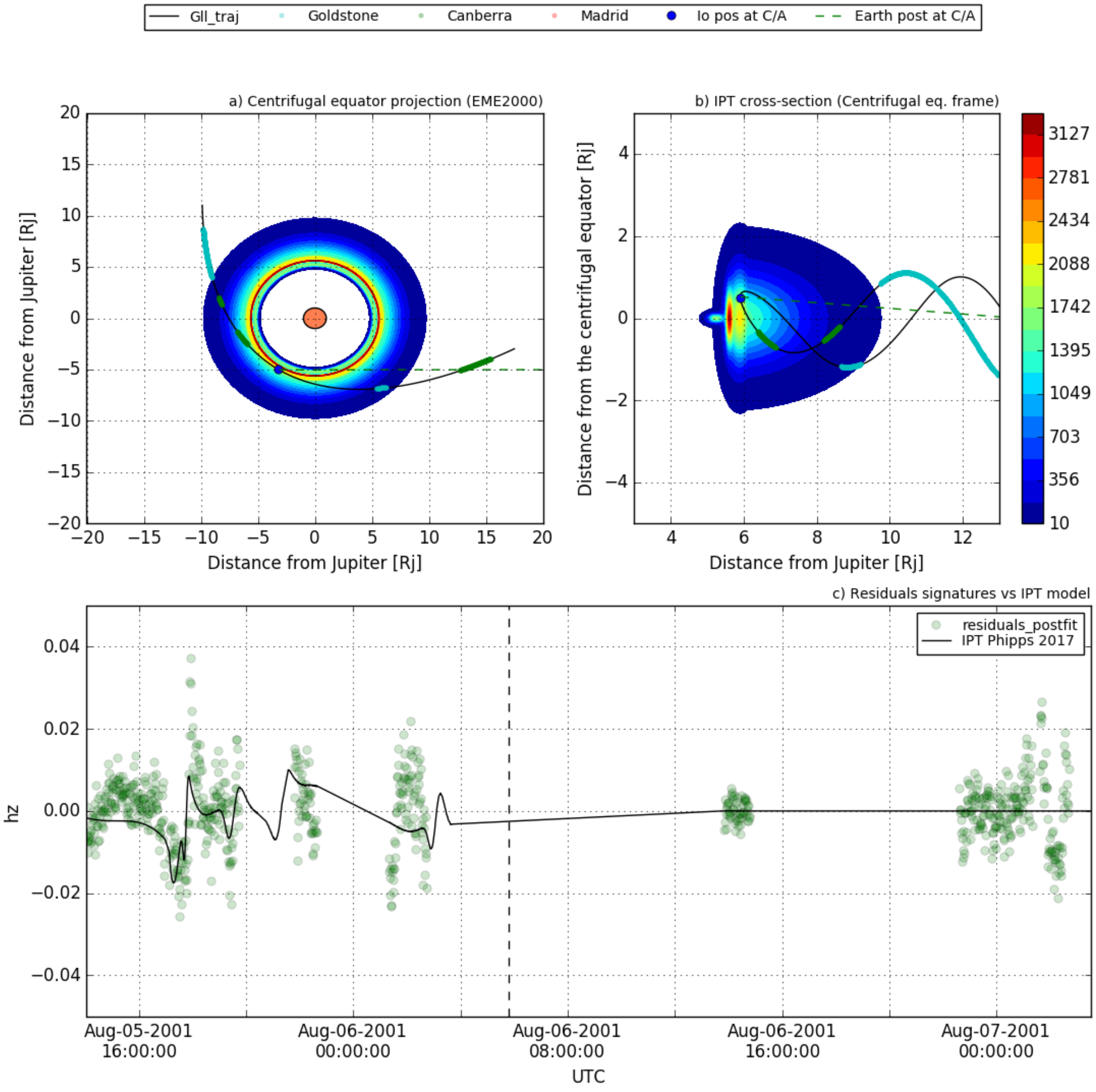

Figure 5.14 – IPT during I31: a) Centrifugal equator projection in EME2000. b) Radial section of the IPT. c) Found signatures against the expected Doppler-shift induced by the IPT, evidencing a good agreement between the model and the retrieved signatures.

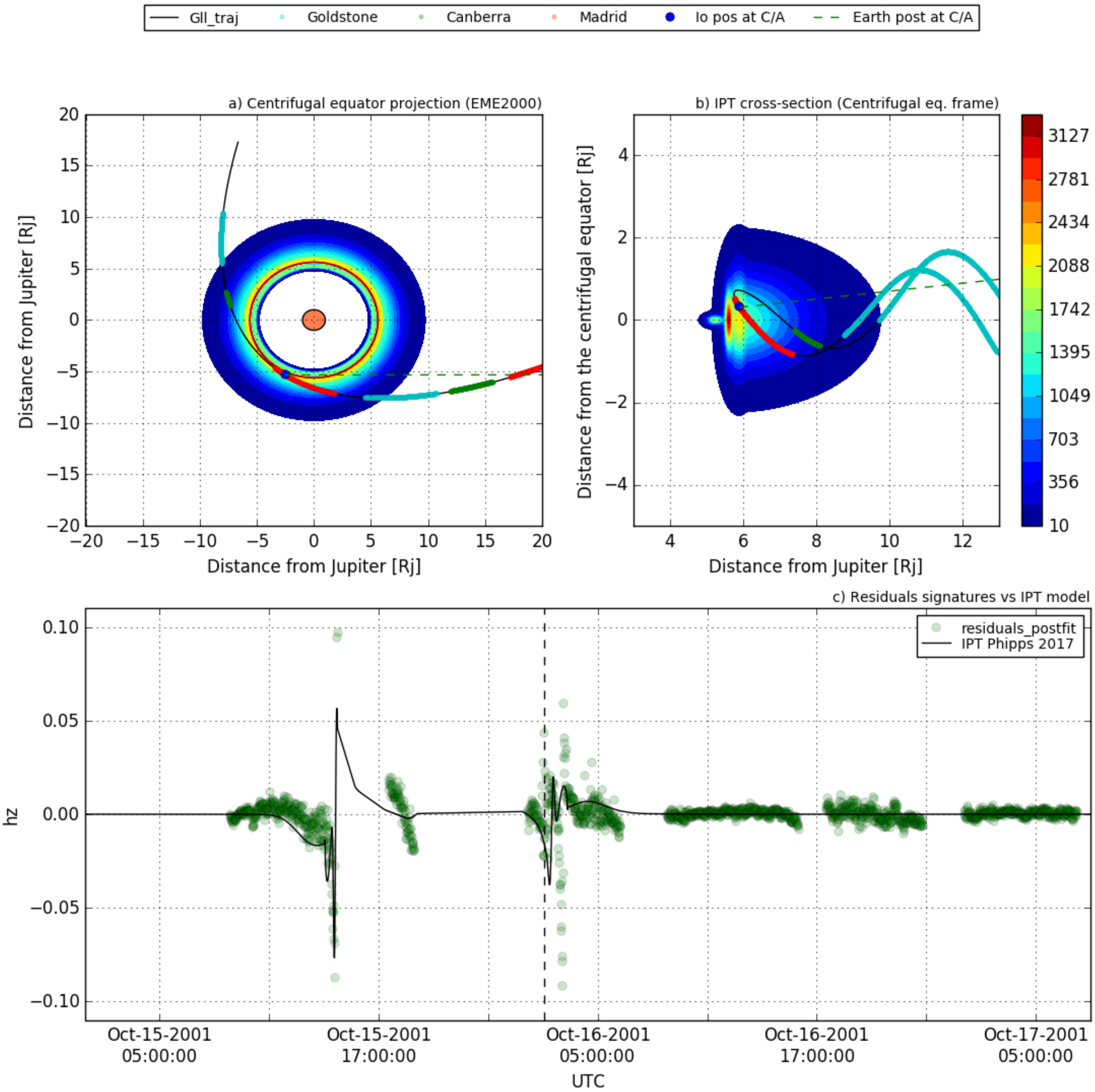

Figure 5.15 – IPT during I32: a) Centrifugal equator projection in EME2000. b) Radial section of the IPT. c) Found signatures against the expected Doppler-shift induced by the IPT, evidencing a great agreement between the model and the retrieved signatures.

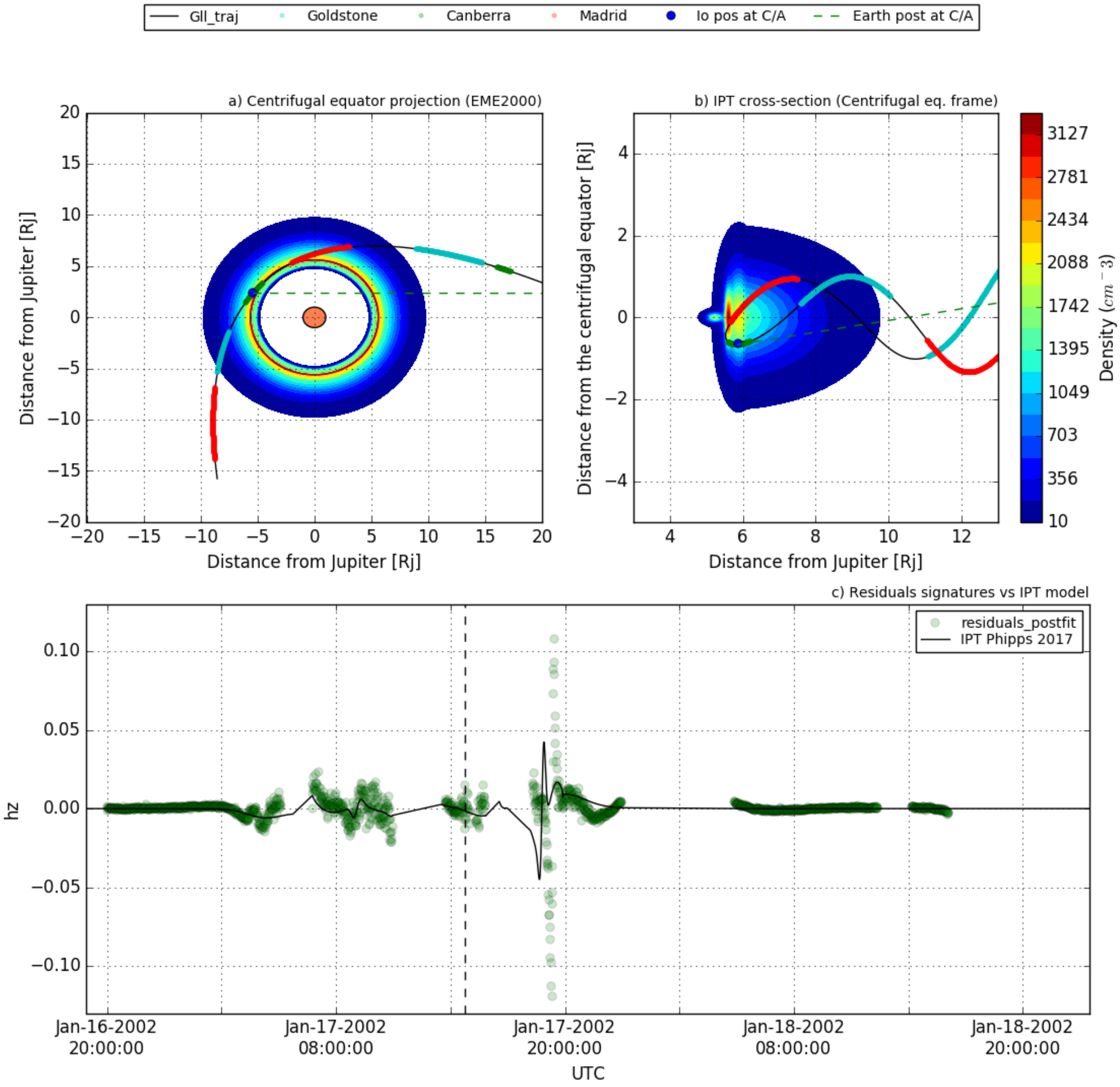

Figure 5.16 – IPT during I33: a) Centrifugal equator projection in EME2000. b) Radial section of the IPT. c) Found signatures against the expected Doppler-shift induced by the IPT, evidencing a great agreement between the model and the retrieved signatures.

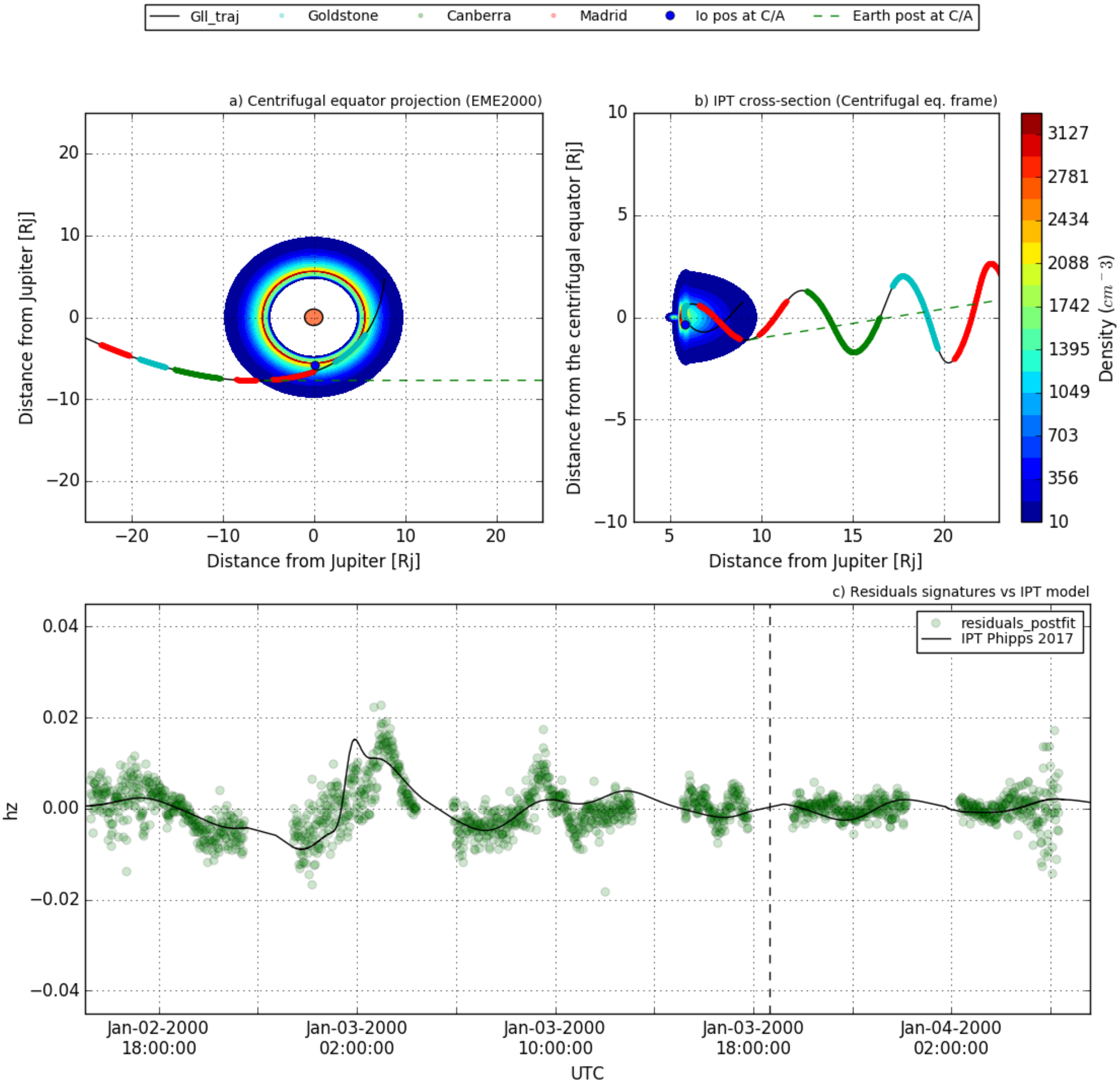

Figure 5.17 – IPT during E26: a) Centrifugal equator projection in EME2000. b) Radial section of the IPT. c) Found signatures against the expected Doppler-shift induced by the IPT, evidencing a good agreement between the model and the retrieved signatures.

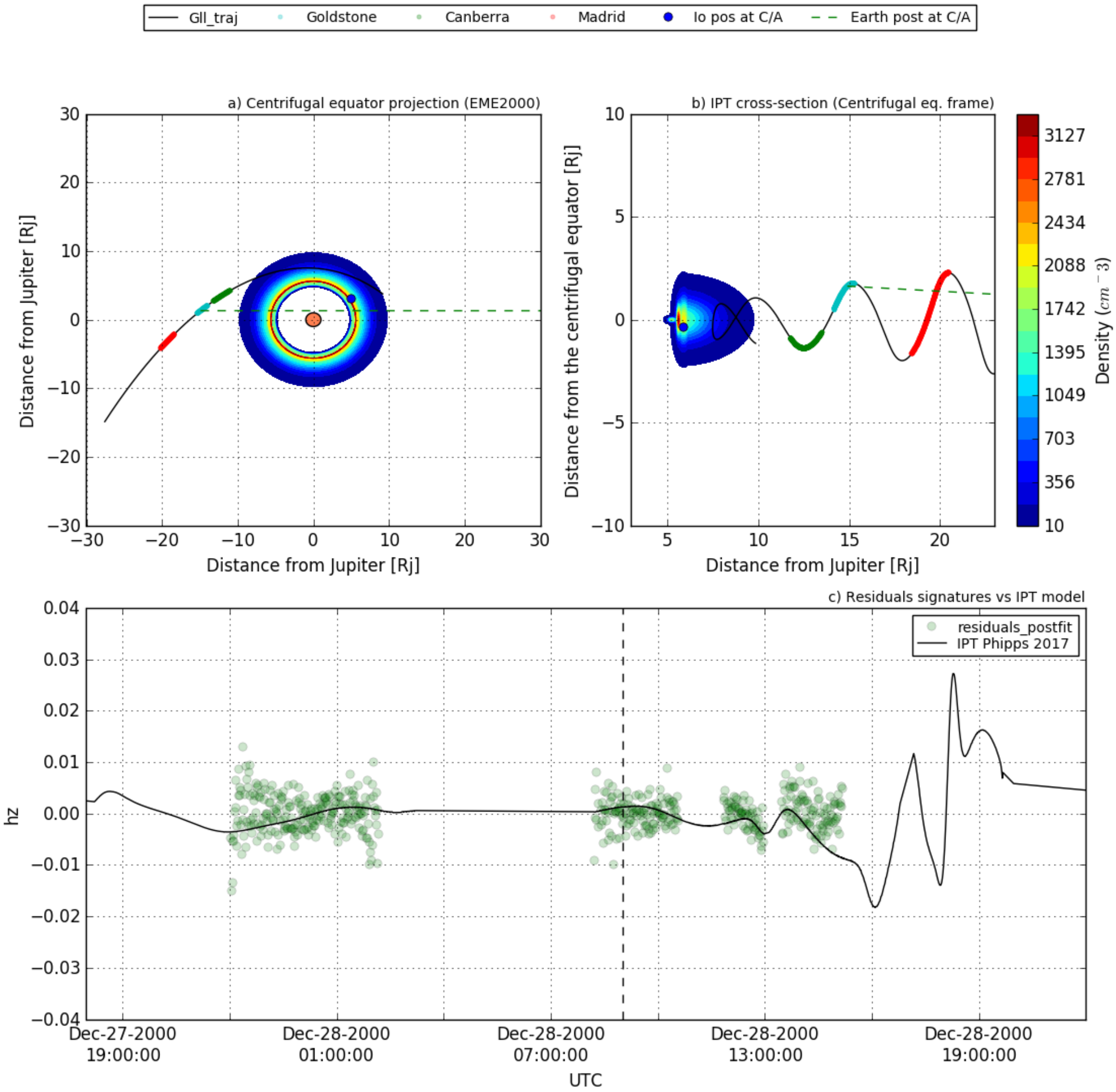

Figure 5.18 – IPT during G29: a) Centrifugal equator projection in EME2000. b) Radial section of the IPT. c) Found signatures against the expected Doppler-shift induced by the IPT, evidencing a good agreement between the model and the retrieved signatures.

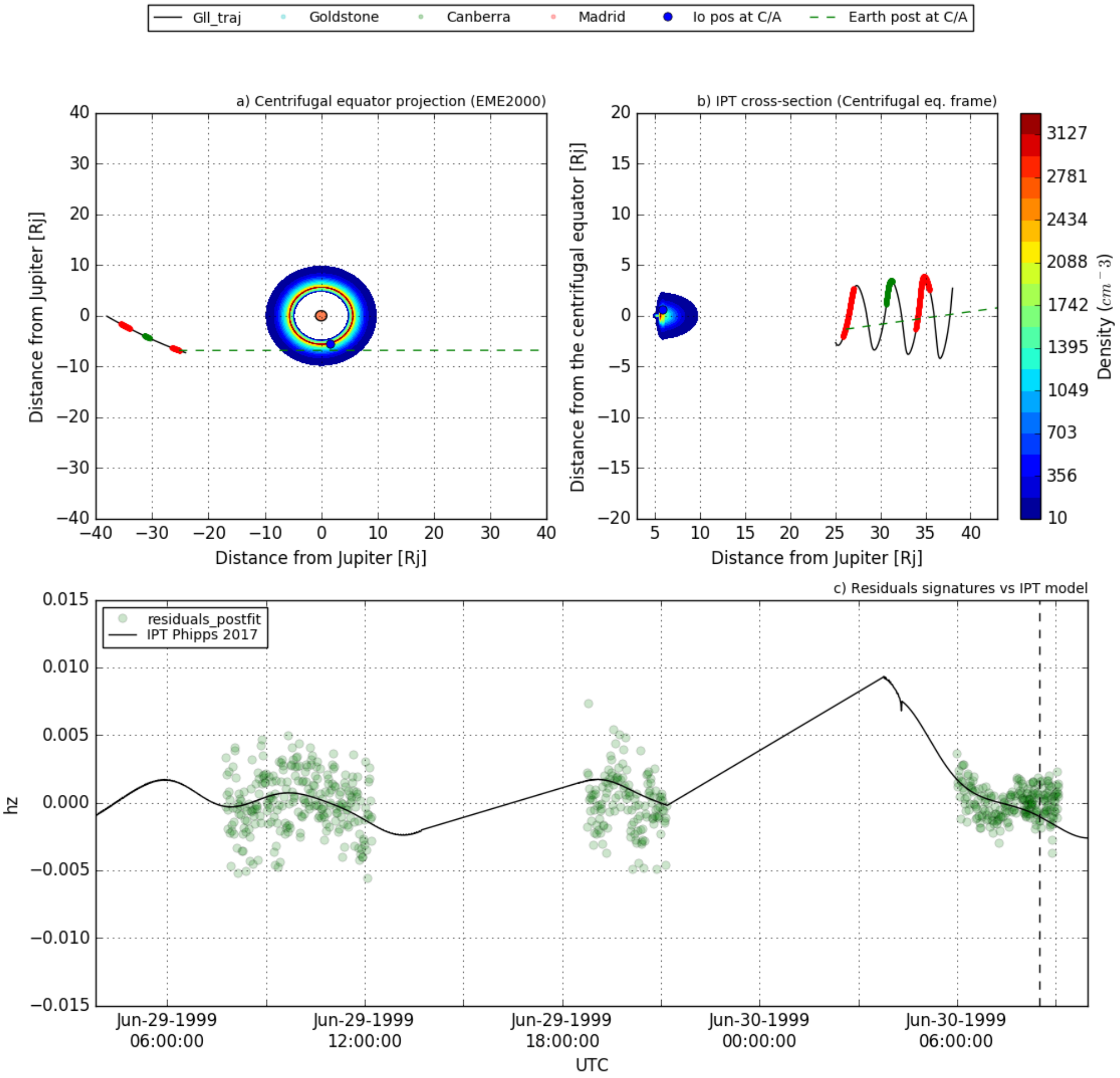

Figure 5.19 – IPT during C21: a) Centrifugal equator projection in EME2000. b) Radial section of the IPT. c) Found signatures against the expected Doppler-shift induced by the IPT, evidencing a good agreement between the model and the retrieved signatures.

Effects of the IPT on Galileo gravity experiments

The parametric model doesn't fit perfectly the signatures but it gives us an idea of the effect that this phenomena can cause on our data. Following this idea and knowing that the HGA deployment failure prevented any dual-frequency calibration of the radio link, that could have corrected or reduced the dispersive signal induced by the IPT, we ran numerical simulations to evaluate the potential effect that the torus could have had on the radio science experiment results. The following steps were ensued to perform numerical simulations of the Galileo gravity science experiment:

- Simulated Doppler observables were generated starting from a-priori values of the solve-for-parameters.
- Gaussian noise with a realistic standard deviation was added to the data. The realistic standard deviation was obtained from the real data post-fit residuals, in which the IPT signatures were treated as outliers.
- A deterministic signature of the IPT, computed using the IPT model [80], was implemented on the simulated observables.
- The data were analysed in a local multi-arc fit, see section 2.4.
- We evaluated the estimation bias with respect to the a-priori values.

The results of the simulations are summarized in figure 5.20, that shows the error caused in the un-normalized gravity coefficients by the IPT, with respect to the reference solution. The error is compared against the obtained formal uncertainty. We conclude that, the effects of the non dynamical Doppler shift induced by the IPT, in the gravity analysis of Europa, Ganymede and Callisto are negligible. However, the dispersive signature caused by the IPT creates unbridgeable biases in the analysis of Io, not only in the gravity coefficients but also on the S/C and Io ephemerides. Moreover, despite the biases induced in the solution, big signatures remain in the data, being the state-parameters not able to fully absorb the Doppler shift caused by the IPT. This remains the case even including the gravity coefficients up to the full 5-degree. The biases found in the gravity coefficients are summarized in the table 5.5, which shows the potential effect of the IPT in the gravity analysis of the different Galilean satellites, in terms of how many σ's the solution is biased.

Table 5.5 – Bias induced in the gravity coefficients, in terms of σ, due to the dispersive signature induced by the IPT.

Parameter	Io	Europa	Ganymede	Callisto
GM (Δ/σ)	48.77	0.0	0.13	0.0
J_2 (Δ/σ)	11.27	0.01	0.23	0.04
C_{21} (Δ/σ)	0.05	0.02	0.25	0.02
S_{21} (Δ/σ)	14.47	0.01	0.24	0.0
C_{22} (Δ/σ)	18.63	0.0	0.22	0.04
S_{22} (Δ/σ)	5.59	0.01	0.31	0.02

Given the negligible effect of the IPT on the Ganymede, Europa and Callisto gravity experiments, we will proceed to re-analyse the radio tracking data of the Galileo encounters, using a local multi-arc approach.

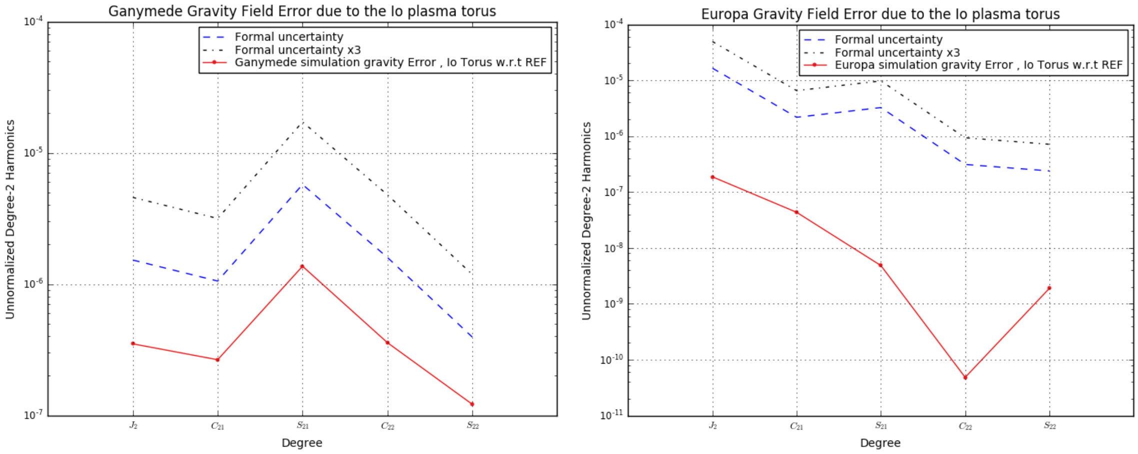

(a) Ganymede gravity experiment.

(b) Europa gravity experiment.

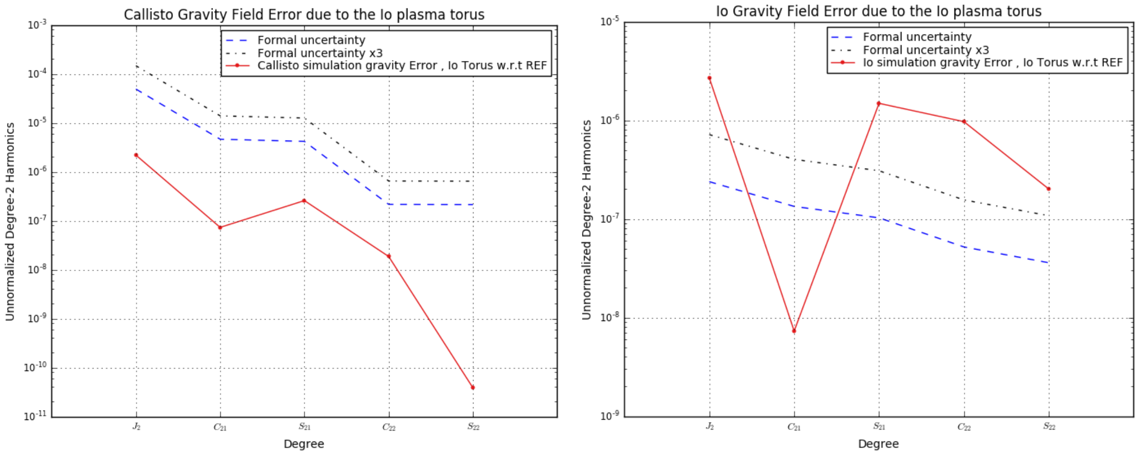

(c) Callisto gravity experiment.

(d) Io gravity experiment.

Figure 5.20 – Results of the IPT simulations for the different satellites. evidencing the negligible effect of the IPT in the Galileo gravity experiment of Ganymede, Europa and Callisto and the non-avoidable errors induced in the gravity coefficients, up to 18-σ in the C_{22}.

Regarding the Io gravity analysis, all the data corrupted by the IPT will be treated as an outlier and cut out of the filter. We will proceed with a preliminary analysis, leaving the final analysis by when we will have proper calibrations for the IPT.

5.3.5 Ganymede data analysis

Introduction

Ganymede, the biggest satellite of the entire solar system, was discovered by Galileo Galilei in 1610. Before the Galileo mission, apart from its mean density discovered from the analysis of Pioneer 10 and Voyager data [24], we did not know much about its interior. The Galileo mission, between other things, brought to light that the Jovian moon is one of the few solid bodies in the solar system that has an internal magnetic field [57] and that Ganymede is differentiated in a metallic core surrounded by a silicate mantle [4], [3], and probably contains a subsurface ocean [58].

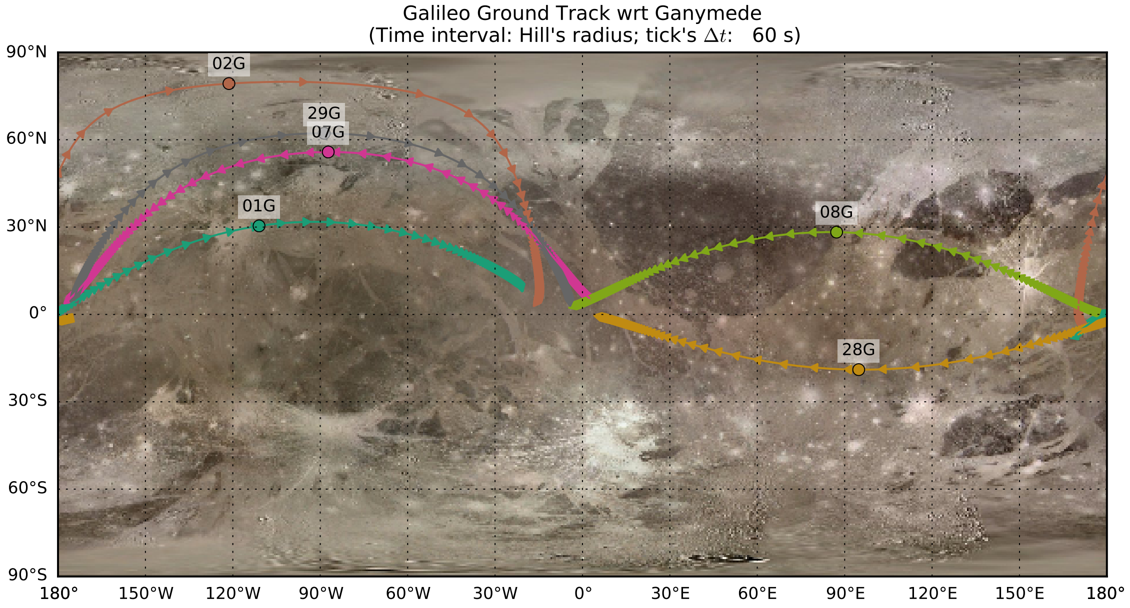

Figure 5.21 – Ground tracks of the flybys performed by Galileo over Ganymede.

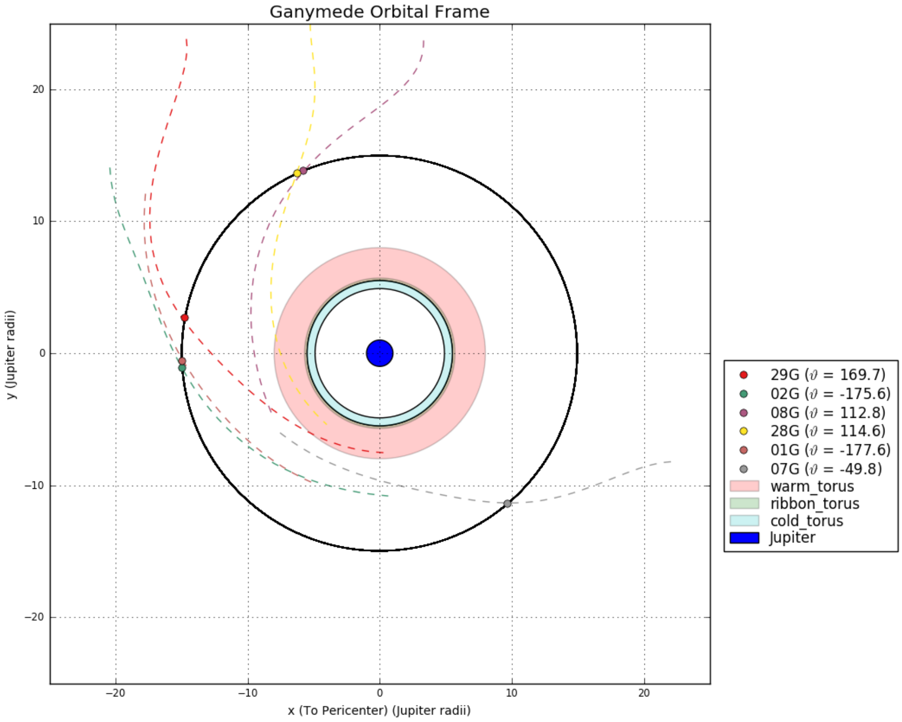

Figure 5.22 – Flybys performed by the Galileo S/C over Ganymede in Ganymede's orbital frame, indicating the mean anomaly and the different zones of the IPT.

The Galileo RS team [4] analysed, independently, data from the two first Ganymede flybys G1 (June, 1996) and G2 (September, 1996) applying the hydrostatic constraint ($J_2/C_{22} = 10/3$) and providing a weighted mean. Subsequently, two more flybys with C/A were added to the analysis G7 (April, 1997) and G29 (December, 2000) finding that a gravity field of degree and order 4 was needed to fit the data to the noise level [3], obtaining non-physical coefficients. This issue was overcame with the interpretation of a gravity anomaly in the vicinity of the G2 closest approach [10], [78].

Alternatively, [48] fitted data from G1, G2, G7, G8, G9 and G12, being the last two flybys almost cruise passes at more than 14000 km of altitude, using a 4x4 gravity field, applying the hydrostatic constraint and obtaining values that differ from the results published by the Galileo RS team.

The global coverage of the data, as seen in figure 5.21, was optimized to provide a good gravity field recovery. Table 5.6 summarizes the characteristics of the flybys and the Doppler-data quality. The poor distribution of Ganymede's flybys along its orbital frame, figure 5.22, together with the low eccentricity of its orbit (0.0015) makes impossible to detect the tidal variations of the satellite.

Multi-arc setup

In order to provide an update on the gravity field of Ganymede, we decided to adopt a local multi-arc approach.

We pre-processed the data and weighted the residuals on a pass-by-pass basis using the RMS of the residuals themselves. The a-priori weights were chosen on the basis of past analysis and mathematical models of the expected noise. The least-squares information filter solved for:

- Initial state of Galileo at the beginning of each arc.
- Initial state of the Satellite at the beginning of each arc.
- Galileo's RTG accelerations.
- Scale factor for the solar radiation pressure.
- Ganymede's gravity field.

Initial state of Galileo The state vector of the Galileo S/C was estimated at the beginning of each arc, approximately one day prior to the C/A. The a-priori values were obtained from the trajectory reconstructed by the Galileo navigation Team, that can be found in the Planetary Data System archive. For a-priori uncertainty we used a conservative approach, using a diagonal covariance matrix with $1-\sigma$ of 300 km for the X and Y direction, while 600 km was used for the Z direction. As for the velocity we used 0.03, 0.03 and 0.06 km/s respectively.

Initial state of the Satellites The state vector of the satellite was estimated at the beginning of each arc. The a-priori values of the state vector of the Galilean satellites were retrieved from the latest Jupiter ephemerides set released by the JPL, JUP310. The a-priori uncertainties were set using a conservative approach, 2000 km for the X, and Y directions in position and 3000 km in Z. For the velocity 0.2, 0.2 and 0.3 km/s were used, respectively.

Table 5.6 – Main orbital, geometrical and quality data characteristics of the Gallileo flybys over Ganymede. These values are referred to the C/A.

		G01	**G02**	**G07**	**G08**	**G28**	**G29**
Date (ERT)	(ET)	27-06-96, 06:30	06-09-96, 19:00	05-04-97, 07:11	07-05-97, 15:57	20-05-00, 10:11	28-12-00, 08:26
Altitude	(km)	836.71	263.01	3103.89	1604.78	810.7	2339
Relative Velocity	(km/s)	7.77	7.95	8.54	8.68	11.33	10.51
Latitude	(deg)	30.41	79.29	55.79	28.26	−18.96	62.2
Longitude	(deg)	−113.38	−123.73	−89.6	84.79	92.43	−91.06
SEP Angle	(deg)	172	113	60	87	9	146
Inclination	(deg)	31.82	79.9	124.2	151	161	62.21
Number of points		1022	918	1048	1218	1246	555
RMS	(mm/s)	0.081	0.059	0.169	0.092	1.83	0.23
C/A Data		*Y*	*Y*	*Y*	*N*	*N*	*Y*
IPT		*N*	*N*	*N*	*N*	*N*	*Y*

RTG's accelerations As explained before, soon after the JOI, the navigation team of Galileo detected an acceleration of 0.4 nm/sec^2 corresponding to the thermal acceleration of the RTG's. We set the a-priori uncertainty at 100% of this value in every direction. During the baseline solutions the RTG's acceleration was a consider parameter.

Solar radiation preassure Galileo's solar radiation pressure scaling factor was set to 1.0 with an uncertainty of the 20%.

Ganymede's gravity field The a-priori values of the GM were retrieved from the JUP310 ephemerides set and J_2, C_{22} from [16]. The a-priori uncertainty of the GM was set large enough in order to not constrain the solution. The a-priori uncertainties for the second degree coefficients were on average two orders of magnitude larger than the formal uncertainties at the end of the estimation process. Higher coefficients were all set to zero, with their corresponding a-priori uncertainty scaled by Kaula's rule using two different scaling factors. The first case $K = 10^{-5}$ while the second $K = 10^{-4}$. To assess the retrieved values, different solutions were generated. The most relevant approaches were:

- MA3: Multi-arc local solution estimating the full degree 3 gravity field.
- MA3-heq: Multi-arc local solution estimating the full degree 3 gravity field, where the ratio between J_2/C_{22} was imposed to the hydrostatic equilibrium value 10/3.
- MA3-W: Multi-arc local solution estimating the full 3-degree gravity field applying the whitening algorithm, to take into account the effect of the coloured noise due to solar plasma in the Doppler tracking data.
- MA4: Multi-arc local solution estimating the full 4-degree gravity field.
- MA5: Multi-arc local solution estimating the full 5-degree gravity field.

The G02 signature

The second close encounter of Galileo over Ganymede, took place the 6th of September, 1996. This second flyby was a gravity science dedicated encounter that followed a near-polar trajectory with a really low altitude, the lowest of all the Ganymede flybys, making G2 really important in the gravity field experiment of Ganymede. In August 2004, [4] reported the discovery of mass anomalies on Ganymede. Two surface mass anomalies, one at high latitude and another at low latitude were necessary to successfully fit the Doppler data, while no geological features that could explain the data could be identified.

Subsequently, another more detailed analysis characterized the size and distribution of the mass anomalies [78] building two different scenarios with four anomalies, two positive and two negative, buried or laying in the surface. In this case, only one of the positive mass anomalies could correspond to a geological feature, the Galileo Regio.

While performing the analysis, we found the reported signature around the C/A of G2 when trying to fit the data using a 2x2 gravity field, see figure 5.23. This artifact in the data disappeared when estimating a full 3rd degree and order gravity field, one degree less than the reported in [3]. We conclude that, the local analysis can bypass this localized signature and that there is no need to add mascons to fit properly the data.

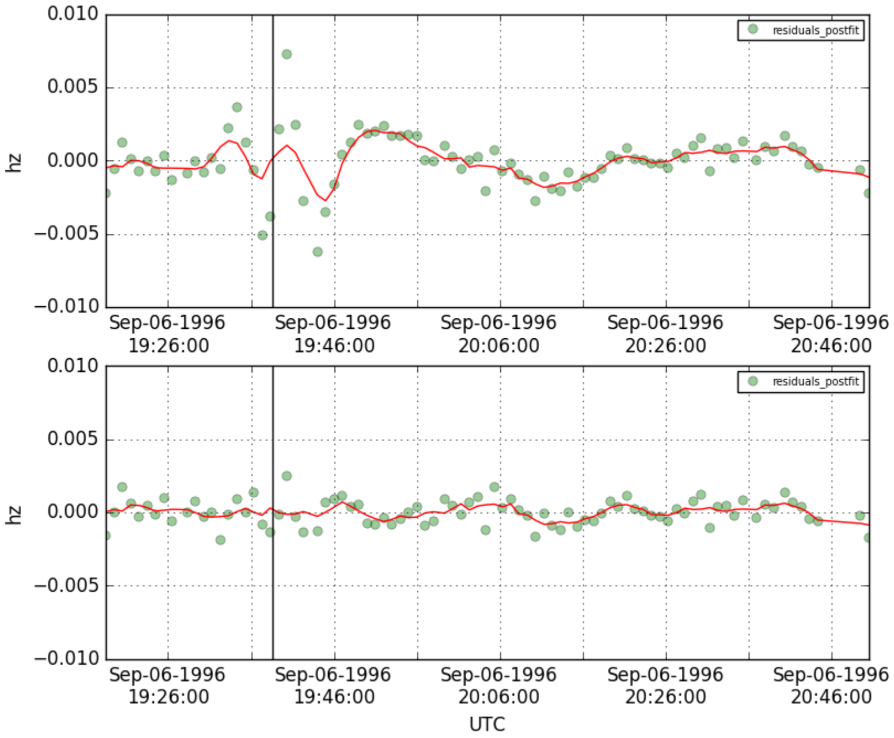

Figure 5.23 – a) Post-fit residuals evidencing the signature in the vicinity of the C/A when estimating a full 2-degree gravity field. b) Post-fit residuals obtained when estimating a full 3-degree gravity field. The signature is absorbed at the noise level.

Results

We combined radio tracking data from all the available flybys, G1, G2, G7, G8, G28 and G29, to retrieve a new estimation of the gravity field of Ganymede. To obtain a satisfactory solution a full degree and order 3 was necessary. Convergence was obtained after a few iterations, but we performed six iterations to ensure the stability of the single solution. Figure 5.24 shows the residuals of the baseline solution. To test the stability of the obtained solutions we performed different estimations that showed similar residuals, without any signature around the C/A that could indicate any inconsistency.

The main stability solutions are plotted in the figure 5.25, which shows the solutions in the 1-σ, $J2 - C_{22}$ plane, showing a big agreement between them. As reported in section 5.3.5, the G2 signature disappeared when estimating a 3x3 gravity field, being $6.5 \cdot 10^{-5}$, the minimum scaling Kaula factor able to absorb the data-artifact.

Figure 5.26 shows Ganymede's gravity anomalies, with respect to the reference ellipsoid defined by the gravity coefficients J_2, C_{22} and its rotation, and its uncertainty in mGals, evidencing a clear zone in the north-west quadrant of the geoid where the uncertainty decreases, this region is coincident with the ground-track of G1 and G2 flybys, being both flybys the ones that provide most information to the solution.

When comparing the second degree values with respect to the reference solution, [4], we find differences in the order of 2.4-σ in the C_{22} coefficient, while J_2 is still compatible at 1-σ. Table 5.7 report the estimated gravity coefficients of the baseline solution, showing a clear C_{31} coefficient not compatible with zero at 3.3-σ.

Given that the pole orientation of the moons is not perfectly known, additional test to check the stability of the gravity solution and the influence of the polar orientation on

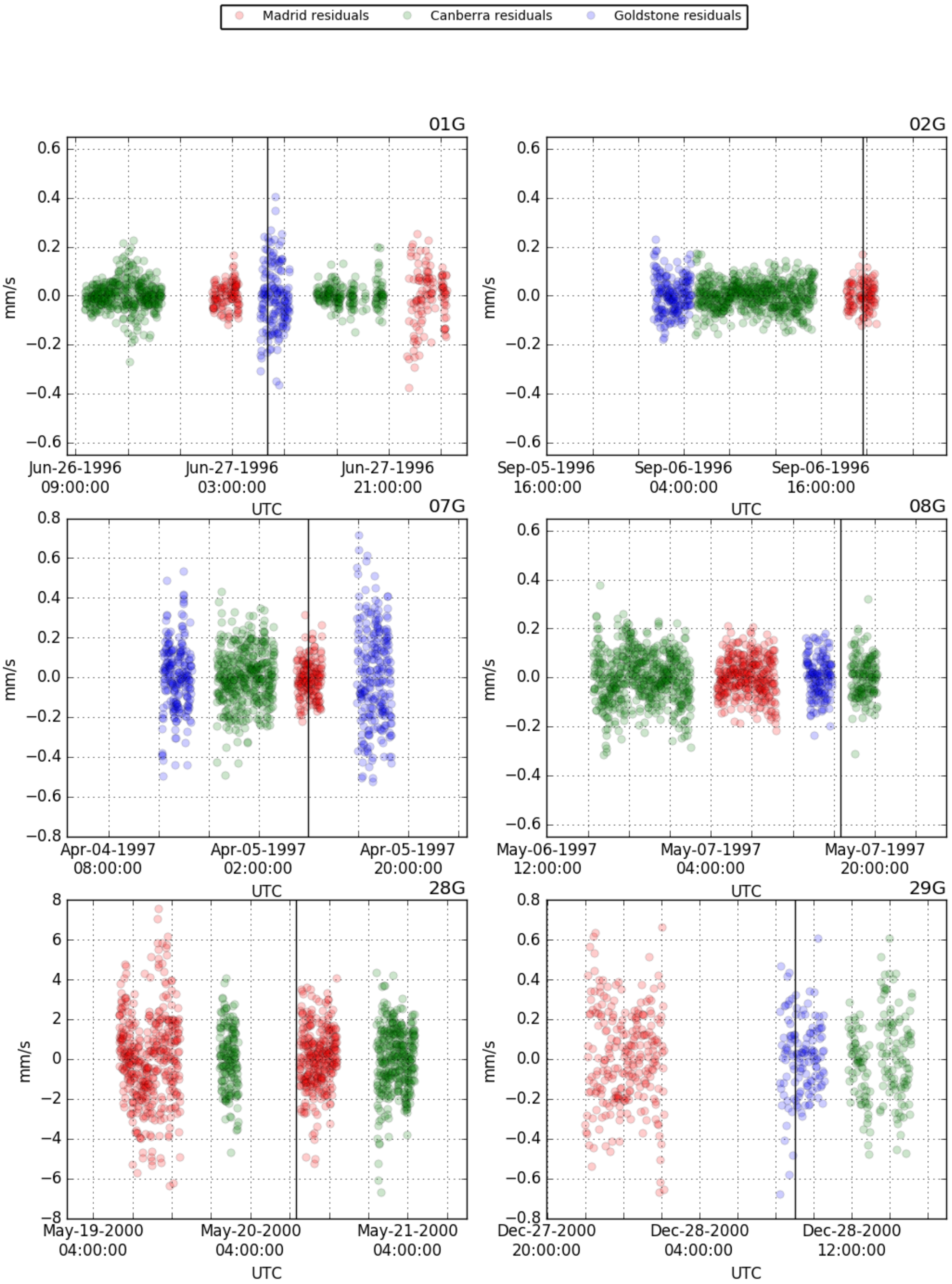

Figure 5.24 – S Band posf-fit residuals of G1, G2, G7, G8, G28 and G29. The vertical line corresponds to the closest approach with Ganymede.

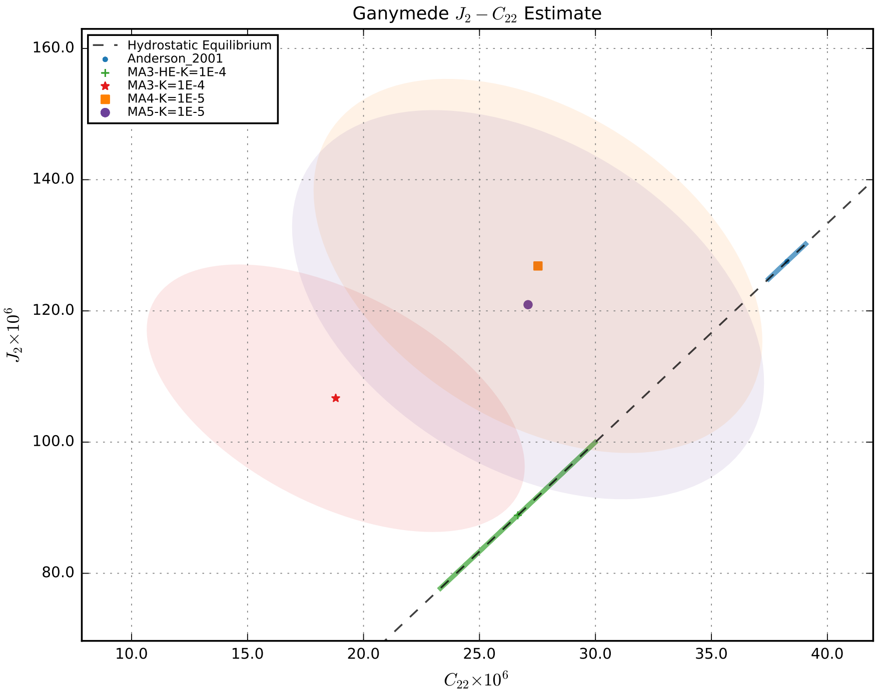

Figure 5.25 – Ganymede multi-arc solutions in the $J_2 - C_{22}, 1 - \sigma$ plane.

Table 5.7 – Ganymede estimated gravity field.

		Apriori	MA-3	MA-3-h.eq
GM	(km^3/s^2)	9888±50	9871.0±1.8	9871.4±1.7
J_2	$(\times 10^6)$	140±100	107±20	89±11
J_3	$(\times 10^6)$	0±29	7±16	13±15
C_{21}	$(\times 10^6)$	0±500	−13.3±7.5	−17.5±6.4
S_{21}	$(\times 10^6)$	0±500	49±28	31±23
C_{22}	$(\times 10^6)$	40±100	18.8±8.1	26.7±3.4
S_{22}	$(\times 10^6)$	0±500	−10.0±4.4	−11.7±4.2
C_{31}	$(\times 10^6)$	0±12	8.3±2.5	9.3±2.3
S_{31}	$(\times 10^6)$	0±12	1±11	7.2±9.2
C_{32}	$(\times 10^6)$	0.0±3.8	1.1±2.9	−0.3±2.6
S_{32}	$(\times 10^6)$	0.0±3.8	1.2±3.0	1.4±3.0
C_{33}	$(\times 10^6)$	0.0±1.5	−0.71±0.85	−0.67±0.85
S_{33}	$(\times 10^6)$	0.0±1.5	0.54±0.80	0.59±0.80
J_2/C_{22}		3.3±8.6	5.7±3.1	10.0/3.0±0.0
corr J_2-C_{22}		+0.00	−0.51	+1.00

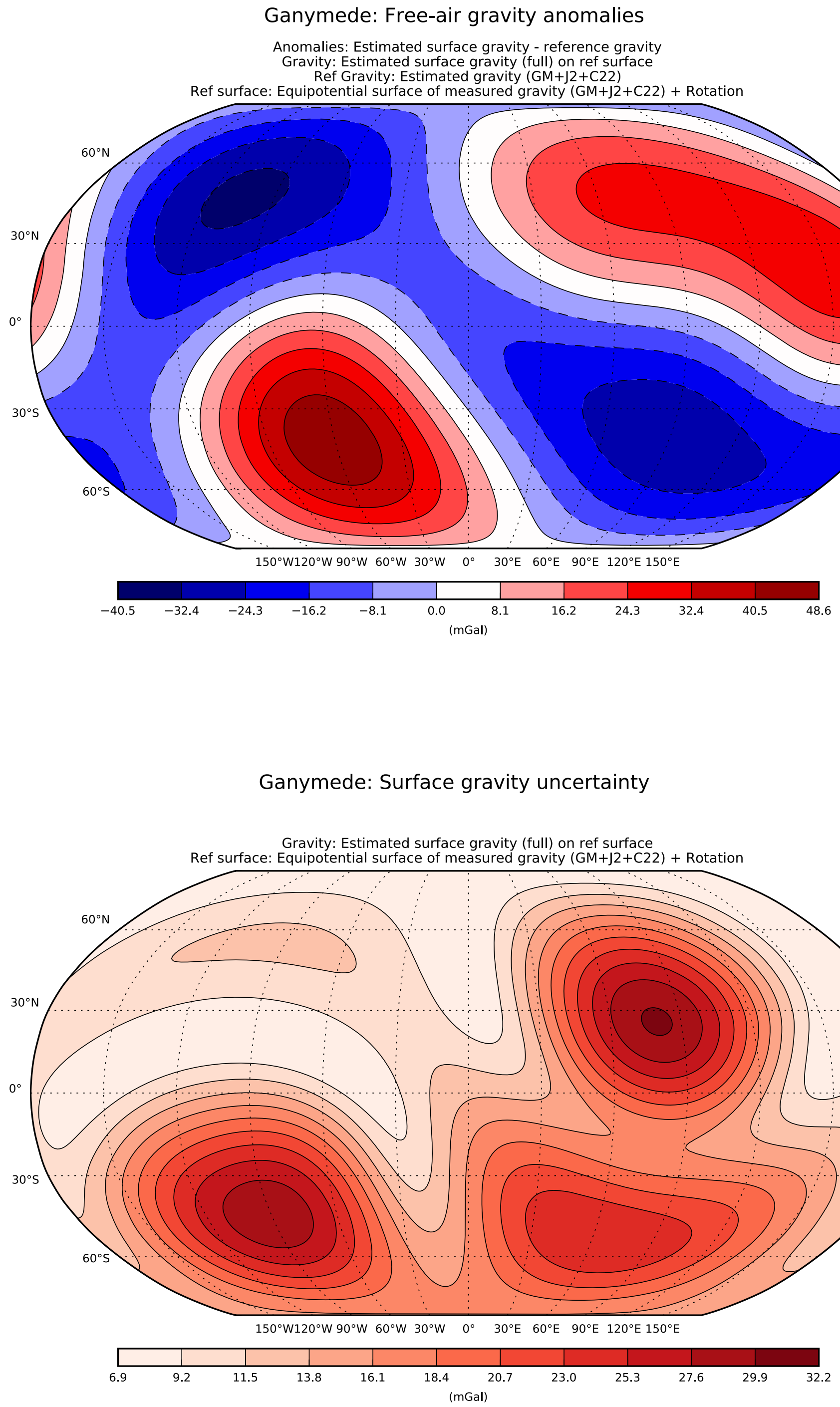

Figure 5.26 – Ganymede's gravity anomalies and uncertainties with respect to the ellipsoid of reference.

the gravity field uncertainties were run. Instead of using a dynamical frame pointing to the empty focus of the orbit we used IAU2015 pole and prime meridian [12] finding that both J_2 and C_{22} remained compatible within 0.72 and 0.1-σ respectively. The lack of more tracking data prevented from estimating a more accurate frame.

5.3.6 Europa data analysis

Introduction

Europa is the smallest moon discovered by Galileo Galilei in 1610. Before the Galileo mission, there was little information about the moon, only its mean density ($3018 \pm 35 kg/m^3$) was known [77]. It is believed to have a global ocean below its ice crust.

The Galileo mission provided plenty of new data that resulted in three different analysis of its gravity field, two of them done by the radio science team of the Galileo project and another one carried by R.Jacobson and the navigation team of Galileo.

The first study, [5], analysed independently the radiometric data acquired during two Europa encounters, E4 (December, 1996) and E6 (February, 1997), providing a weighted mean of the gravity coefficients, concluding that the retrieved gravity was compatible with a metallic core surrounded by an ice-liquid outer shell. Due to the geometry of both flybys, see figure 5.27, the J_2 and C_{22} coefficients were highly correlated, so the hydrostatic a-priori constraint was applied. Additionally, J_3 and C_{33} gravity coefficients were added due to an inconsistency in the independent results for E4 and E6.

The second publication, [7], analysed four flybys, adding E11 (November, 1997) and E12 (December, 1997) to the previous E4 and E6, along with ground-based astrometric data and optical navigation observables from both Voyager and Galileo. The data were fit estimating the coefficients of the standard spherical harmonics expansion up the third degree, constraining the J_2 to an a-priori of 10/3 of C_{22}. In addition, due to the low altitude of the E12 flyby, the possibility of an atmospheric drag that could have affected the motion of Galileo, was introduced. Again, just like in the previous analysis, a discrepancy between the C_{22} coefficient, retrieved in the single-arc estimation of the E4 flyby and the rest of the flybys, was found. The inconsistency was attributed to the non-coherent Doppler data recorded during the C/A of this pass. The analysis concluded that Europa is most likely differentiated into a metallic core surrounded by a rock mantle and a water outer shell in liquid or solid state. This possibility comes from the fact that the gravity experiment cannot resolve between both, due to the similar values in the density.

Finally, [48] reports on a reconstruction of Galileo's orbit during the prime mission and the construction of a Jupiter's system ephemerides set by means of a global-fit. The analysis used radiometric data up to E19 (February 1999) and estimated a full 3-degree gravity field, applying the hydrostatic constrain, finding relevant differences with both previous analyses.

During the Galileo mission in the Jupiter system, Galileo encountered Europa eleven times, from all of them only four had two-way Doppler data during the close encounter. In addition to the gravity flybys, we also used data from other flybys not explicitly dedicated to gravity science. The main orbital, geometrical and quality indicators of the flybys are summarized in table 5.8. Figure 5.27 presents the ground track of all the eight flybys used in the following analysis. Unfortunately, all of them were nearly equatorial so we don't expect high accuracy on the determination of the J_2 coefficient. On the other hand as seen in figure 5.28, these flybys were favourably distributed along Europa's orbit suggesting the possibility of inferring the tidal variations of the moon.

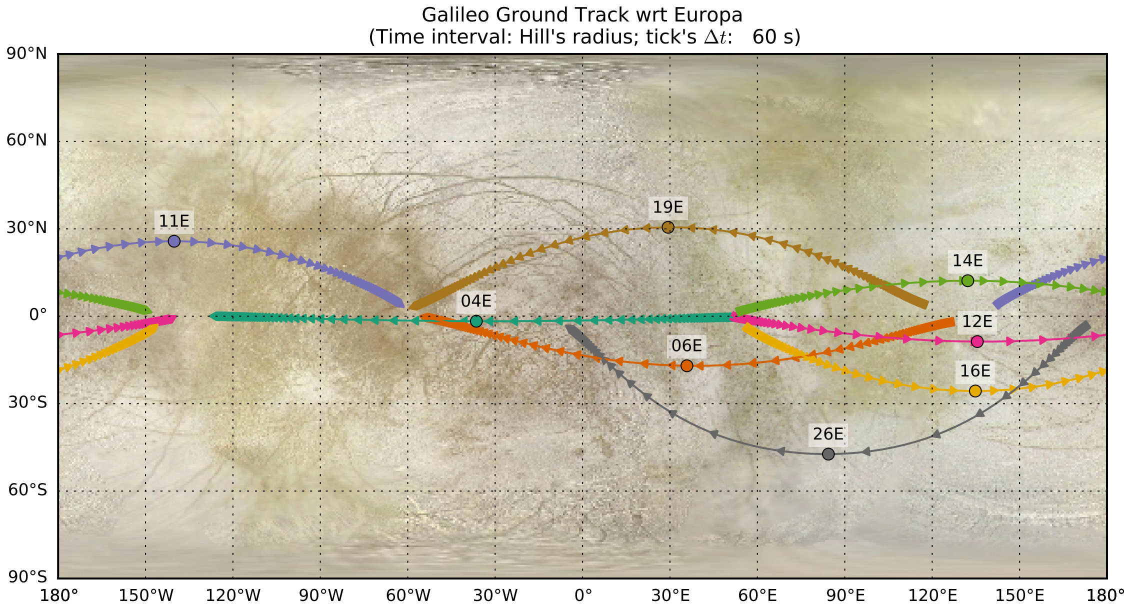

Figure 5.27 – Ground tracks of the flybys performed by Galileo over Europa.

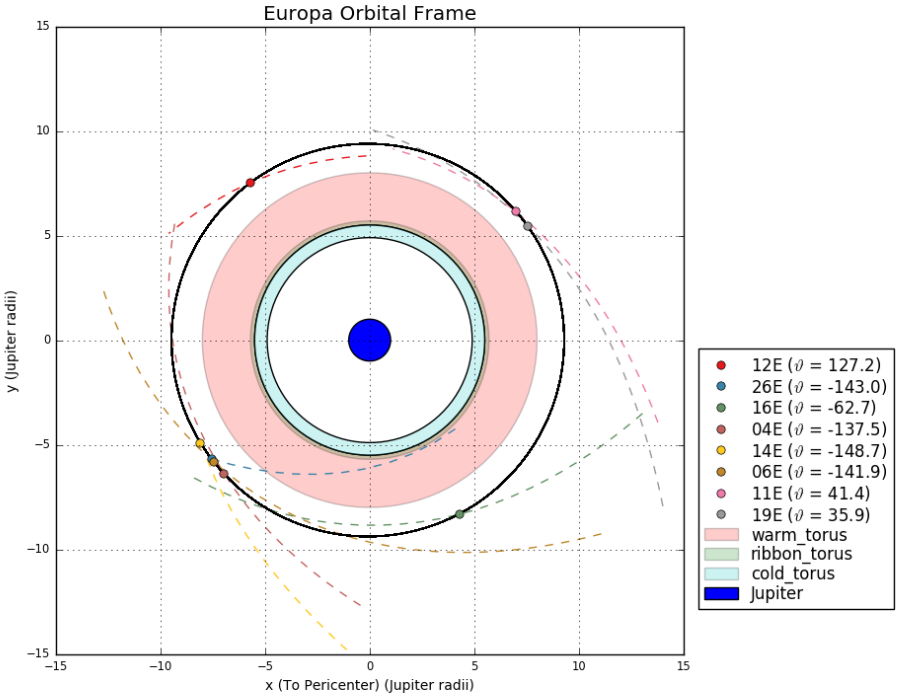

Figure 5.28 – Flybys performed by the Galileo S/C over Europa in Europa's orbital frame, indicating the mean anomaly and the different IPT zones.

Plume on Europa

During the last years, several authors reported evidences of water plumes erupting from Europa, discovered analysing the data acquired by the Hubble Space Telescope [81], [83]. More recently, a new study, [51], showed evidence of a plume on Europa from the magnetic field and plasma wave observations recorded during Galileo's E12 flyby of Europa. This plume, localized around $245°W$ and $5°S$ in a region with high surface temperature, could have affected the motion of the Galileo S/C during its close encounter with Europa. In our analysis, we will include the potential perturbation due to the discovered plume in order to determine if this phenomena could be detected by means of the orbit determination of Galileo, and if this is the case, how much can it bias the gravity results.

Multi-arc setup

After pre-processing the data, the residuals were weighted on a pass-by-pass basis using the RMS of the residuals itself. The a-priori weights were chosen on the basis of past analysis and mathematical models of the expected noise. The least-squares information filter solved for:

- Initial state of Galileo at the beginning of each arc.
- Initial state of the Satellite at the beginning of each arc.
- Galileo's RTG accelerations.
- SRP scale factor.
- F3 bias.
- Plume during E12.
- Europa's gravity field.

Initial state of Galileo The state vector of the Galileo S/C was estimated at the beginning of each arc, approximately one day prior to the C/A. The a-priori values were obtained from the trajectory reconstructed by the Galileo navigation Team. For a-priori uncertainty we used a conservative approach, using a diagonal covariance matrix with $1-\sigma$ of 300 km for the X and Y direction, while 600 km was used for the Z direction. As for the velocity we used 0.03, 0.03 and 0.06 km/s respectively.

Initial state of the Satellites The state vector of the satellite was estimated at the beginning of each arc. The a-priori values of the state vector of the Galilean satellites were retrieved from the latest Jupiter ephemerides set released by the JPL, JUP310. The a-priori uncertainties were set using a conservative approach, 2000 km for the X, and Y directions in position and 3000 km in Z. For the velocity 0.2, 0.2 and 0.3 km/s were used respectively.

RTG's accelerations As explained before, soon after the JOI, the navigation team of Galileo detected an acceleration of $0.4nm/sec^2$. We set the a-priori uncertainty at 100% of this value in every direction. In the baseline solution the RTG's acceleration was a consider parameter. In addition it was estimated to test the stability of the solution.

Table 5.8 – Main orbital, geometrical and quality data characteristics of the Gallileo flybys over Europa. These values are referred to the C/A.

		E04	**E06**	**E11**	**E12**	**E14**	**E16**	**E19**	**E26**
Date (ERT)	(ET)	19-09-96, 06:54	20-02-97, 17:07	06-11-97, 20:32	16-12-97, 12:04	29-03-98, 13:22	21-07-98, 05:04	01-02-99, 02:20	03-01-00, 18:00
Altitude	(km)	693.03	587.00	2044.57	201.86	1644.88	1835.21	1440.5	351.32
Relative Velocity	(km/s)	5.75	5.77	5.72	6.27	6.42	6.22	5.83	11.31
Latitude	(deg)	−1.70	−16.99	25.74	−8.69	12.19	−25.66	30.52	−47.31
Longitude	(deg)	−36.45	35.83	−140.16	135.5	132.22	−134.82	29.36	84.38
SEP Angle	(deg)	25	25.15	89	55	26	120	46	102
Inclination	(deg)	178.29	162.98	25.74	8.70	12.19	25.66	149.47	132.68
Number of points		601	1001	1407	903	2034	1552	1006	352
RMS	(mm/s)	0.583	0.455	0.159	0.216	0.389	0.078	0.162	0.118
C/A Data		*N*	*Y*	*Y*	*Y*	*Y*	*Y*	*N*	*N*
IPT		*N*	*N*	*N*	*N*	*N*	*N*	*N*	*Y*

Solar radiation preassure Galileo's solar radiation pressure scaling factor was set to 1.0 with an uncertainty of the 20%.

F3 biases Added during E11 in the DSS-14 and E12 in the DSS-63, to prevent for the possible DSN inter-station clock offset. The value was set to zero with an a-priori sigma of 0.1 Hz.

Europa plume We modelled E12 plume, detected by recent analysis, as a small impulse burn during the C/A. The value was set to zero with a large uncertainty of 5 mm/sec.

Europa's gravity field The a priori values of the GM were retrieved from the JUP310 ephemerides while J_2, C_{22} from [7]. Higher coefficients were all set to zero. The a-priori uncertainty for the GM was set to 10 times the formal uncertainty found in [7]. We used large a-priori values for the second degree in order to avoid any constraint on the final solution. The a-priori uncertainty of higher gravity coefficients scaled with Kaula's rule using two different scaling factors K. The first case $K = 10^{-6}$ while the second $K = 10^{-5}$. To assess the retrieved values, different solutions were generated. The most relevant approaches were:

- SA: Single-arc, local solution for each arc with C/A data.
- MA2: Multi-arc local solution estimating the full 2-degree gravity field.
- MA2-pl: Multi-arc local solution estimating the full 2-degree gravity field, adding the plume during E-12.
- MA2-k_2: Multi-arc local solution estimating the full 2-degree gravity field and the tidal variations of Europa.
- MA2-heq: Multi-arc local solution estimating the full 2-degree gravity field. where the ratio between J_2/C_{22} was imposed to the hydrostatic equilibrium value 10/3.
- MA2-W: Multi-arc local solution estimating the full 2-degree gravity field applying the whitening algorithm, to take into account the effect of the coloured noise due to solar plasma in the Doppler tracking data.
- MA3: Multi-arc local solution estimating the full 3-degree gravity field.
- MA4: Multi-arc local solution estimating the full 4-degree gravity field.

Results

Data from E6, E11, E12, E14, E16 and E26, were combined to retrieve a gravity field capable to fit the data. E6, E12, E14 and E16, were the flybys that provided more information about the gravity field of Europa, given that radio tracking data during the close encounter with the satellite were recorded. The data were successfully fit to the noise level using the local multi-arc strategy estimating a second degree and order gravity field. In any case, different solutions were produced to assess the stability of the estimated values. Table 5.9 collects the estimated gravity field coefficients for the baseline solutions. The solutions found were all compatible with them, with no big deviations, moreover, the results are compatible with an hydrostatic Europa within 1-σ without applying the hydrostatic constraint.

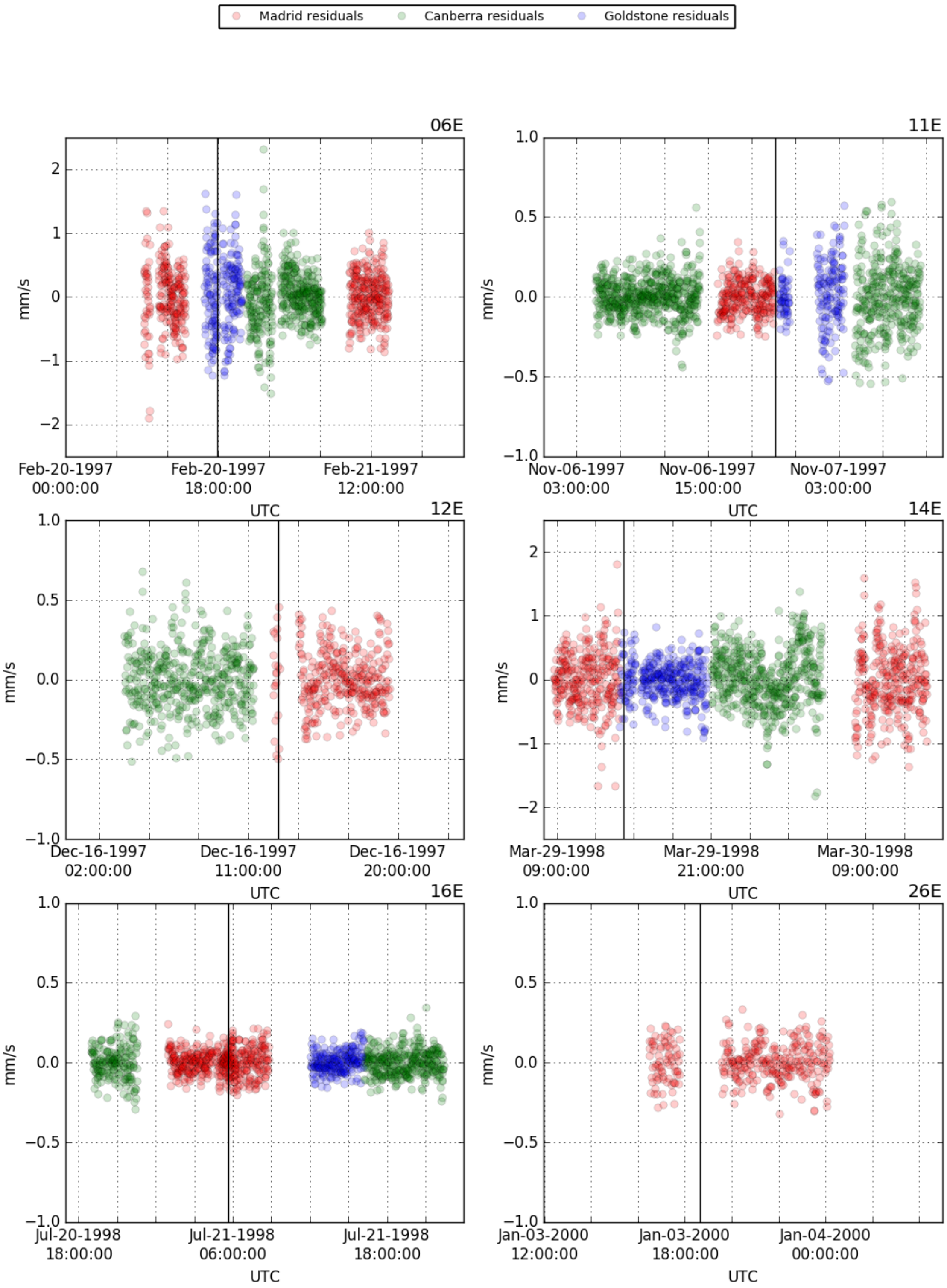

Figure 5.29 – S Band posf-fit residuals of E6, E11, E12, E16 and E26. The vertical line corresponds to the closest approach with Europa.

Figure 5.29 report the post-fit residuals of the baseline solution described above (MA-2). For all the solutions, the residuals do not show any evident signature around the closest approach, obtaining almost the same RMS value for each arc. The flybys E4 and E16 show higher noise due to their low SEP.

Figure 5.30 displays the different single-arc solutions against the best solutions (MA-2 and MA-2-pl) in the $J_2 - C_{22}$ plane showing that all the solutions are compatible within 1-σ.

Finally, figure 5.31 shows the main solutions against the two last published results, [7] and [48], evidencing differences with respect the old analysis. While the differences in the J_2 coefficient are within 1.5-σ, the differences in C_{22} grows up to 4.9-σ with respect to the last analysis of the RS team and 8.5-σ if we compare it against the reference value of R.A. Jacobson.

Europa E12 plume The MA2-pl solution retrieved an impulse burn equal to $\Delta V_x = -1.75 \pm 0.83$ mm/s, compatible with zero within 2-σ. In addition, to check the stability of the obtained value, all the previous solution were ran with the addition of the E12 plume as an estimation parameter. We retrieved a very stable value, in all the cases, compatible with the estimated value within less than 1-σ.

Moreover, these values were compatible with the drag deceleration (0± 3 mm/sec) estimated in [7], without providing big changes on the estimated gravity coefficients. More investigation will be carried out in the next months.

Tidal parameters Despite the good coverage of Galileo's flybys along Europa's orbital frame, the low value of its eccentricity (0.009) makes difficult to provide a reliable estimate of the tidal Love number $Re(k_2)$. We found that $Re(k_2) = -0.149 \pm 0.165$. In any case, the analysis is useful to provide a higher limit for the value. Considering the $3 - \sigma$, it provides a higher limit of 0.3465 at 3-σ, which is compatible with the assumed value of 0.2 that can be found in literature [90].

A future global multi-arc approach might provide more interesting results due to smaller size of the parameter-size compared against the local multi-arc approach.

Table 5.9 – Europa estimated gravity fields.

		Apriori	MA2	MA2-pl	MA2+k2
GM	(km^3/s^2)	3202.74±0.20	3202.72±0.20	3202.71±0.20	3202.72±0.20
J_2	$(\times 10^6)$	400±1000	524±84	448±92	497±90
C_{21}	$(\times 10^6)$	0±500	9±13	5±13	8±13
S_{21}	$(\times 10^6)$	0±100	−18±16	−4±17	−14±17
C_{22}	$(\times 10^6)$	130±100	140.3±1.8	138.1±2.1	139.9±1.9
S_{22}	$(\times 10^6)$	0±100	−9.9±1.7	−7.7±2.0	−9.6±1.7
J_2/C_{22}		3.3±8.0	3.74±0.59	3.24±0.65	3.55±0.63
corr J_2-C_{22}		+0.00	+0.25	+0.40	+0.32

Following the same approach done in Ganymede, we used the IAU2015 rotational frame [12] instead of using a dynamical frame to check the stability of the gravity solution against a different rotational model. We found that both J_2 and C_{22} remained compatible within 0.02 and 0.28-σ respectively.

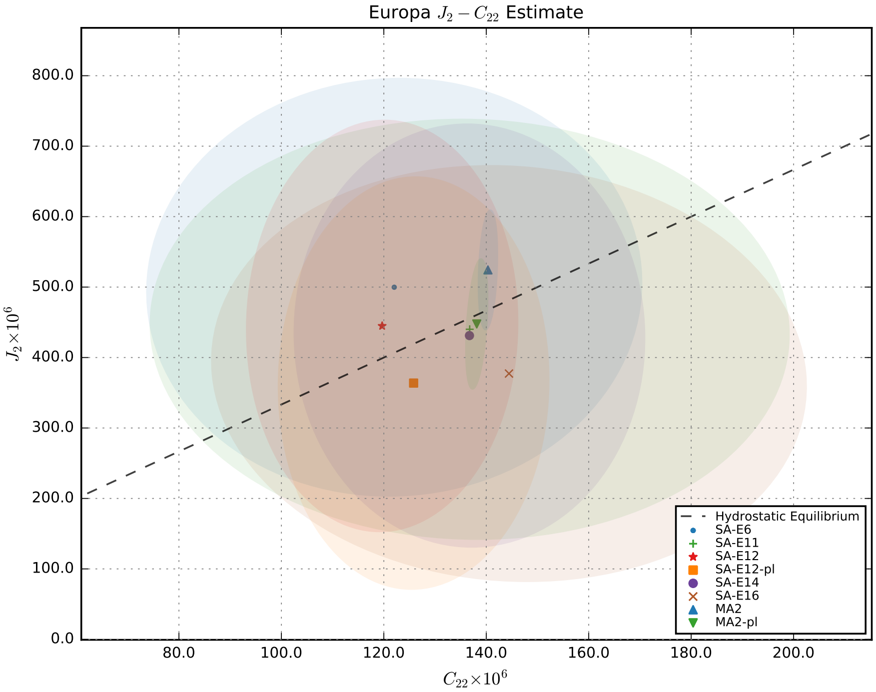

Figure 5.30 – Europa single-arc solutions in the $J_2 - C_{22}, 1 - \sigma$ plane.

5.3.7 Callisto data analysis

Introduction

Discovered by Galileo Galilei in 1610, Callisto is the third largest moon in the entire solar system. Previous to this analysis, two different results of Callisto's gravity field were published by the RS team. The first of them, used data acquired during the flybys C3 (November, 1996), C9 (June, 1997) and C10 (September, 1997) [6]. The second one [3], added data of two more close encounters: C20 (May, 1999) and C21 (June, 1999). Both analysis were carried out assuming the hydrostatic equilibrium constraint, due to the poor quality coverage of the flybys. The analysis concluded that Callisto cannot be entirely differentiated, pointing to the hypothesis of a mixed rock and ice region, possibly extending to the center of the satellite. This result is unexpected, given that the magnetic field perturbations measured by the Galileo S/C were used to infer a global sub-surface ocean [92].

The determination of Callisto's gravity field was carried out using data from seven flybys. With respect to the last published result [3], we added two more flybys, C22 (August, 1999) and C23 (September, 1999), leaving outside of the analysis C20 and C30, given their low SEP angle. However, from all the used encounters, only two of them had data during the closest approach, C10 and C21. All of the performed flybys were equatorial, see figure 5.33. That means that we don't expect Galileo to be sensitive to Callisto's J_2 variations along its trajectory, hence, an independent determination of the rotational and tidal gravity field components will be impossible. Also, given the low eccentricity value of Callisto's orbit (0.007) plus the poor distribution of Galileo's flybys along Callisto's orbital frame, makes us disbelieve in the detection of Callisto's tidal variations. Table 5.10 provides a summary of the characteristics of the flybys. Between all the encounters,

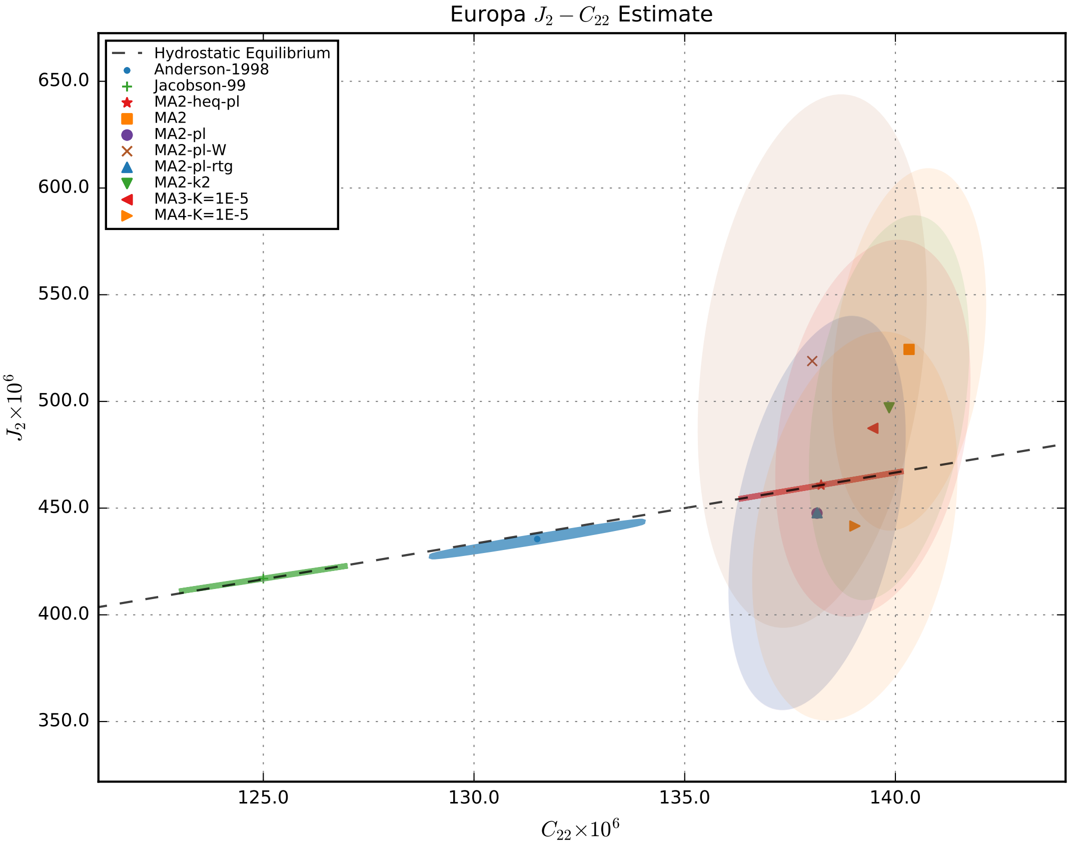

Figure 5.31 – Europa most relevant multi-arc solutions in the $J_2 - C_{22}, 1 - \sigma$ plane, against the reference values published in [7] and [48].

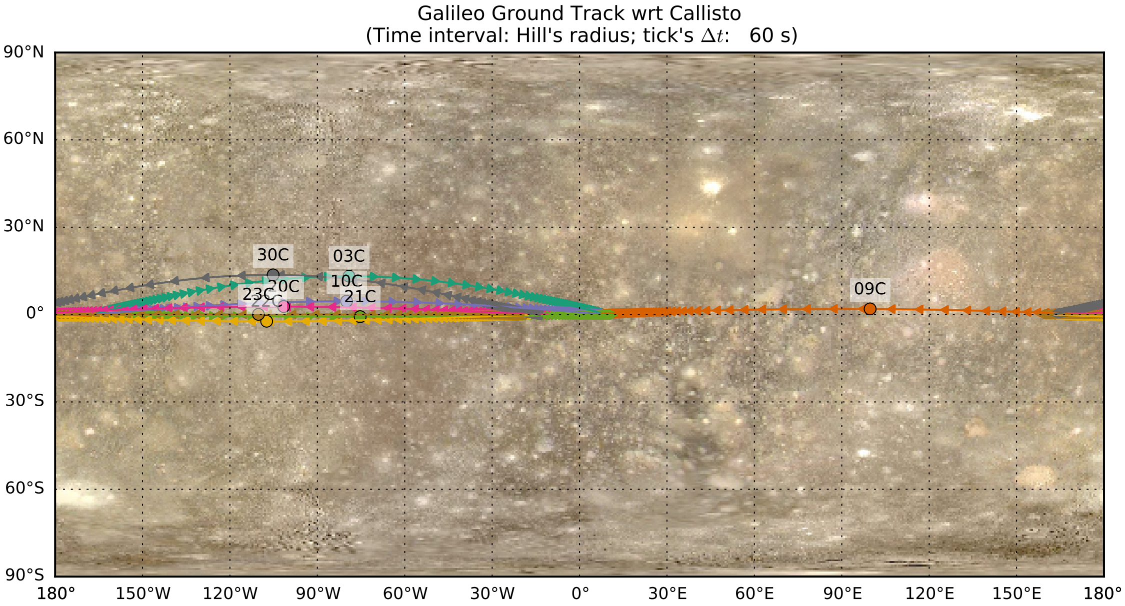

Figure 5.32 – Ground tracks of the flybys performed by Galileo over Callisto.

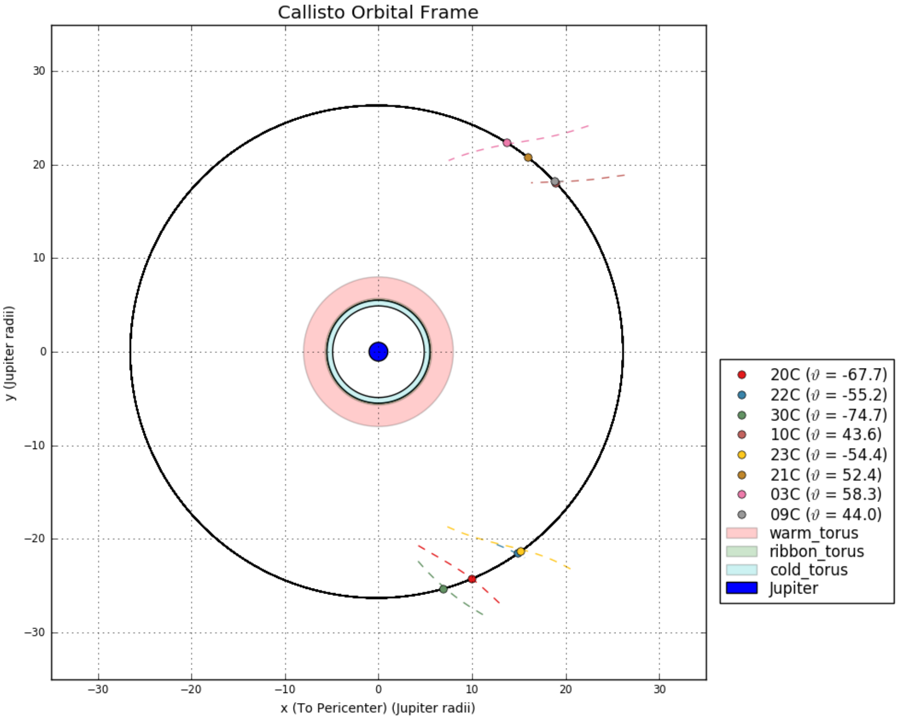

Figure 5.33 – Flybys performed by the Galileo S/C over Callisto in Callisto's orbital frame, indicating the mean anomaly and the different IPT regions.

Table 5.10 – Main orbital, geometrical and quality data characteristics of the Gallileo flybys over Callisto. These values are referred to the C/A.

		C03	**C09**	**C10**	**C21**	**C22**	**C23**	**C30**
Date (ERT)	(ET)	04-11-96, 13:35	25-06-97, 13:48	17-09-97 00:19	30-06-99 07:47	14-08-99, 08:31	16-09-99 17:28	25-05-01 11:25
Altitude	(km)	1129.35	411.73	528.82	1041.82	2292.81	1045.85	131.08
Relative Velocity	(km/s)	7.94	8.23	8.21	8.62	8.53	8.58	9.72
Latitude	(deg)	13.18	1.94	4.58	−0.72	−2.29	0.06	13.62
Longitude	(deg)	−77.5	101.2	−78.48	−73.7	107.25	−110.07	−105.16
SEP Angle	(deg)	61	132.31	139	67	106	139	15
Inclination	(deg)	13.18	178.03	4.58	0.72	177.71	179.9	166.37
Number of points		1174	433	1160	223	661	1470	694
RMS	(mm/s)	0.142	0.068	0.041	0.068	0.088	0.054	3.64
C/A Data		*N*	*N*	*Y*	*Y*	*N*	*N*	*N*
IPT		*N*	*N*	*N*	*Y*	*N*	*N*	*N*

the one with the lowest pericenter altitude was C30 (May 2001). Unfortunately, data were not acquired during the close encounter and the approach was too close to the solar conjunction increasing several times the expected noise.

Multi-arc setup

As for Europa and Ganymede, we used a local multi-arc approach in order to retrieve the gravity coefficients. After pre-processing the data, the residuals were weighted on a pass-by-pass basis using the RMS of the residuals themselves. The a-priori weights were chosen on the basis of past analysis and mathematical models of the expected noise. The least-squares information filter solved for:

- Initial state of Galileo at the beginning of each arc.
- Initial state of the Satellite at the beginning of each arc.
- Galileo's RTG accelerations.
- SRP scale factor.
- Callisto's gravity field.

Initial state of Galileo The state vector of the Galileo S/C was estimated at the beginning of each arc, approximately one day prior to the CA. The a-priori values were obtained from the trajectory reconstructed by the Galileo navigation Team. For a-priori uncertainty we used a conservative approach, using a diagonal covariance matrix with $1-\sigma$ of 300 km for the X and Y direction, while 600 km was used for the Z direction. As for the velocity we used 0.03, 0.03 and 0.06 km/s respectively.

Initial state of the Satellites The state vector of the satellite was estimated at the beginning of each arc. The a-priori values of the state vector of the Galilean satellites were retrieved from the latest Jupiter ephemerides released by the JPL, JUP310. The a-priori uncertainties were set using a conservative approach, 2000 km for the X, and Y directions in position and 3000 km in Z. For the velocity 0.2, 0.2 and 0.3 km/s respectively.

RTG's accelerations As explained before, soon after the JOI, the navigation team of Galileo detected an acceleration of $0.4nm/sec^2$. We set the a-priori uncertainty as 100% of its value in every direction. In the baseline solution the RTG's acceleration was a consider parameter.

Solar radiation preassure Galileo's solar radiation pressure scaling factor was set to 1.0 with an uncertainty of the 20%.

Callisto's gravity field The a priori values of the GM were retrieved from the JUP310 ephemerides set. Both J_2 and C_{22} were retrieved from [3]. The a-priori uncertainty for the GM was set to 10 times the formal uncertainty found in [7]. To avoid any constraint on the final results we set a large value of 10^{-4} for all the five coefficients of the second degree and order.

To examine the solution we ran different robustness tests, of which the most relevant were:

- SA: Single-arc, local solution for each arc covered with radio tracking data during the C/A, (C-10 and C-21) estimating a full 2-degree.

- MA2: Multi-arc local solution estimating the full 2-degree gravity field.

- MA2-HE: Multi-arc local solution estimating the full 2-degree gravity field, where the ratio between J_2/C_{22} was imposed to the hydrostatic equilibrium value of 10/3.

Results

Combined data from six flybys, C3, C9, C10, C21, C22 and C23 were fit in order to found the gravity coefficients up to the 2nd degree and order. A pure quadrupole gravity field was adequate to obtain a good fit of the data. In addition, given the poor sensitivity of the J_2 coefficient, plus the fact that the equilibrium theory predicts that a satellite in synchronous rotation should be hydrostatic, we applied the hydrostatic constraint between the rotational and tidal parameter.

Post-fit residuals of the different flybys of the best solution are reported in figure 5.34, evidencing a proper fit without any signature in the vicinity of the C/A. Moreover, we obtained same fit qualities for both stability tests.

The addition of the C3, C9, C22 and C23, to C10 and C21, provided an improvement of 47% in the uncertainty of the GM estimation.

Figure 5.35 compares both single-arc solutions with the two multi-arc solutions in the $J_2 - C_{22}$ plane showing the compatibility between them and with the hydrostatic assumption. Estimated values of both solutions can be found in table 5.11. It is interesting to note that the correlation between the J_2 and C_{22} for the multi-arc solution is equal to -0.9, highlighting the expected high correlation between both coefficients.

Finally, figure 5.36 displays the multi-arc solutions against the reference values published in [3]. Both solutions are compatible, concluding that the local reanalysis of Callisto did not provide any new improvement with respect to the original one and more data is needed to unveil the interior of the icy satellite with more accuracy.

Table 5.11 – Callisto estimated gravity fields coefficients.

		Apriori	MA2	MA2-HE
GM	(km^3/s^2)	7179.30±0.10	7179.308±0.100	7179.308±0.100
J_2	$(\times 10^6)$	32±1000	250±580	34.0±2.2
C_{21}	$(\times 10^6)$	0±100	50±26	51±26
S_{21}	$(\times 10^6)$	0±100	−6±17	−4±17
C_{22}	$(\times 10^6)$	10±100	9.7±1.5	10.19±0.65
S_{22}	$(\times 10^6)$	0±100	0.9±1.2	1.1±1.0
J_2/C_{22}		0±100	26±63	10.0/3.0±0.0
corr J_2-C_{22}		+0.00	−0.90	+1.00

To asses the stability of the gravity coefficients to the pole orientation we used IAU2015 rotational frame [12] finding that both J_2 and C_{22} remained compatible within 0.01 and 0.04-σ respectively.

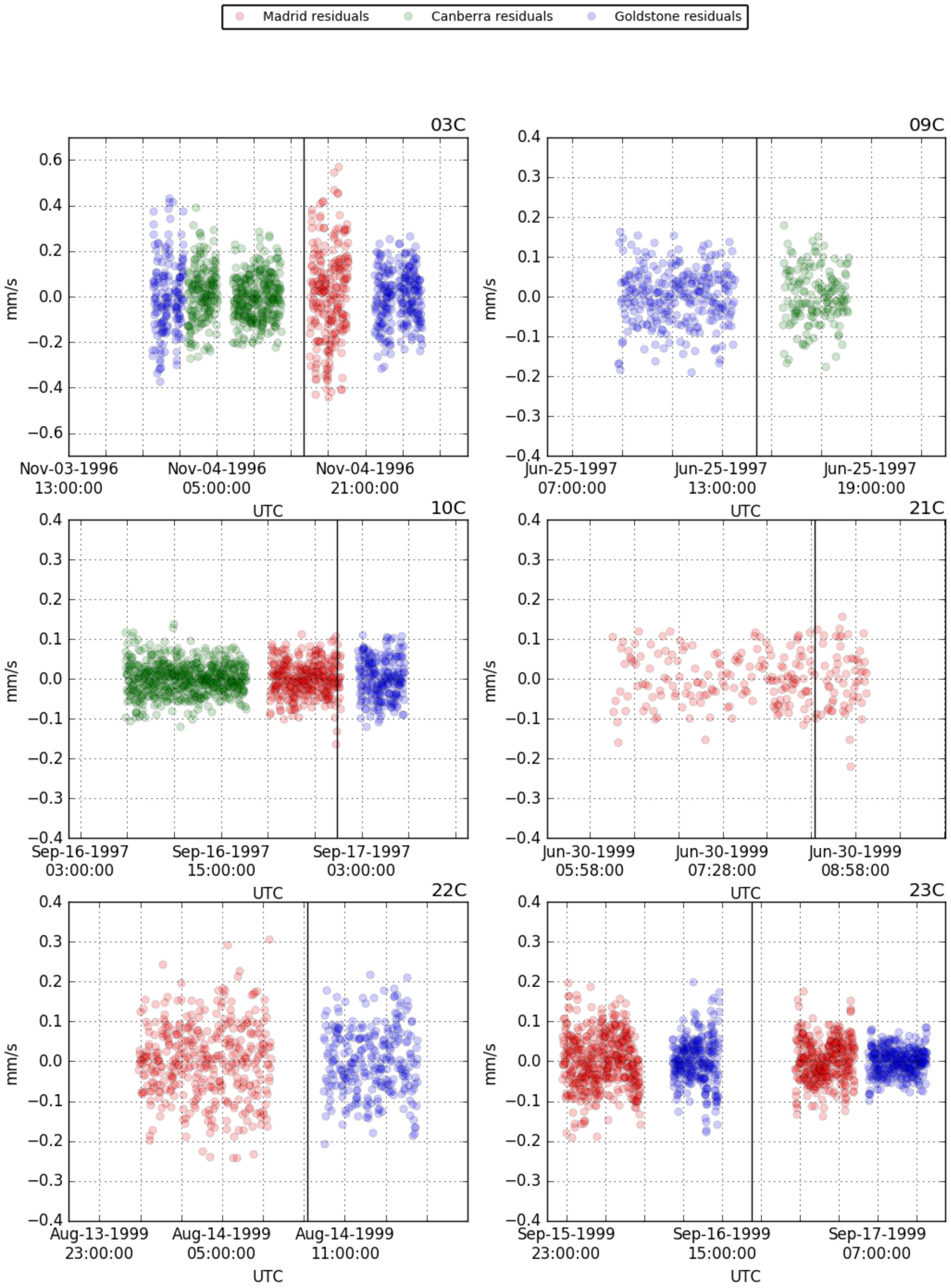

Figure 5.34 – S Band posf-fit residuals of C03, C09, C10, C21, C22 and C23. The vertical line corresponds to the closest approach with Callisto.

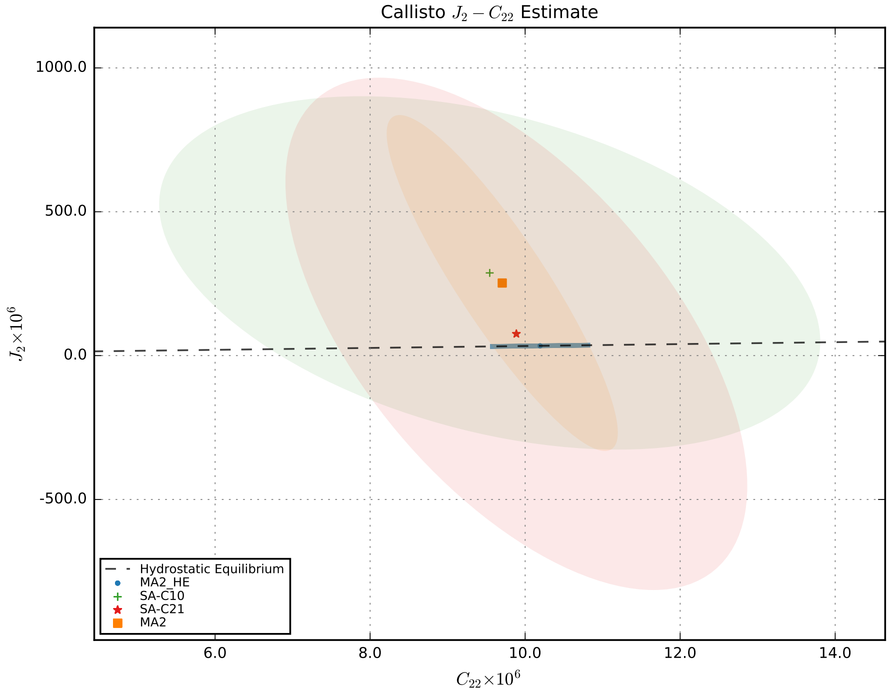

Figure 5.35 – Estimated quadrupole solutions, single-arc and multi-arc, in the $J_2 - C_{22}$ plane with their 1-σ error ellipses.

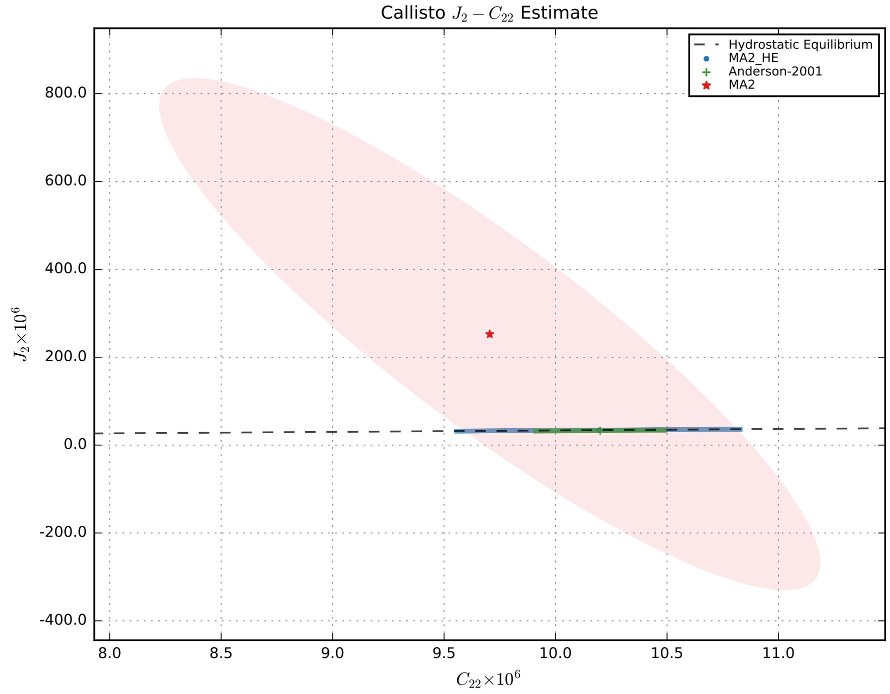

Figure 5.36 – Estimated multi-arc solution against the reference value, in the $J_2 - C_{22}$ plane, 1-σ error ellipses.

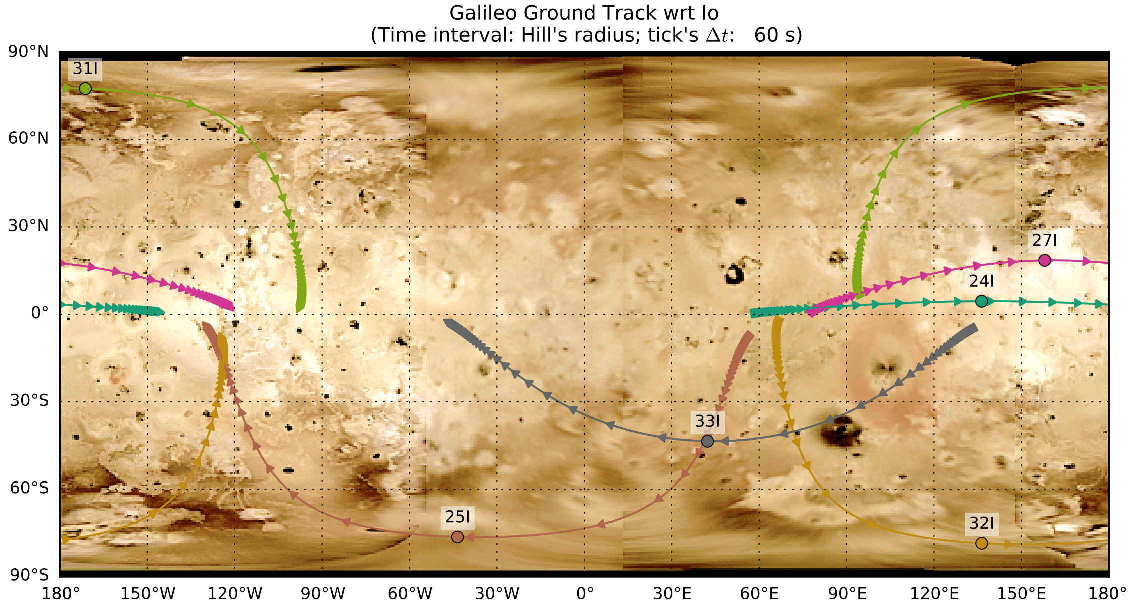

Figure 5.37 – Ground tracks of the flybys performed by Galileo over Io.

5.3.8 Io data analysis

Introduction

Io was disvovered by Galileo Galilei in 1610, is the innermost Galilean satellite and the most geologically active body in the entire solar system, with more than 400 active volcanoes, with many of them emitting plumes of dust and gas [34]. The geological activity is related to the frictional heating generated by the periodic deformation of the moon by Jupiter's gravitational pull.

The first gravity analysis, [8], used one-way Doppler data generated by the USO of the S/C, acquired during the first encounter of Galileo with Io soon before the JOI (I0). Due to the geometry of the flyby, the J_2 coefficient could not be determined independently from C_{22}, so the hydrostatic constraint was applied, concluding that the gravity field was compatible with a large metallic core.

In succession, [9], analized range-rate data from four flybys, I0, I24, I25 and I27, applying the hydrostatic constraint and estimating all the gravity coefficients up to the third degree to obtain a satisfactory fit, confirming the metallic core of Io.

Finally in [16] we see a subsequent analysis in which I33 was added. When adding the last flyby, an independent determination of both J_2 and C_{22} was possible, but it produced a bias of more than 4-σ in the C_{22} coefficient, stating that could be a problem in the satellite ephemerides of the system. The article suggests to use this last result as reference result of the Galileo gravity analysis.

None of the previous analyses mentioned any kind of IPT correction that could have

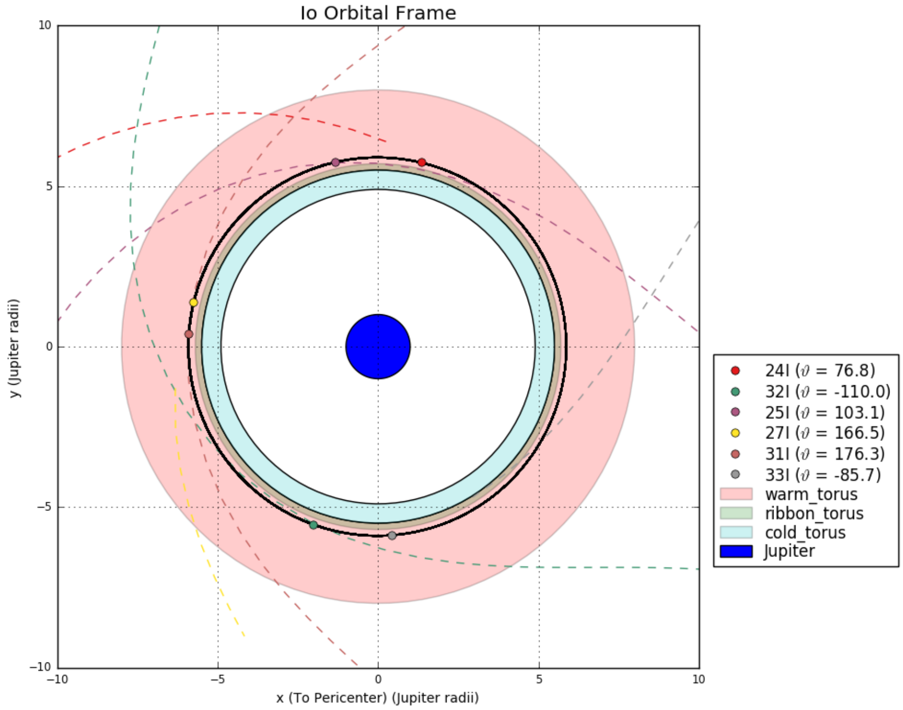

Figure 5.38 – Flybys performed by the Galileo S/C on Io in Io's orbital frame, indicating the mean anomaly and the different IPT regions.

taken into account the dispersive signature induced in the radio tracking data.

Figure 5.37 shows the ground track of all the flybys that the Galileo S/C performed over Io, showing an optimal global coverage to retrieve the gravity field of the volcanic moon. In addition, the sampling of the flybys in the orbital frame, figure 5.38, made Io a nice candidate to estimate its k_2 Love number. However, the data corruption, due to the IPT, and the low amount of usable data to perform the analysis, prevented the estimation of this interesting value.

Finally, table 5.12 summarizes all the geometrical parameters of all the encounters and their data quality. Note that the flybys that were severely corrupted by the IPT do not present the data-quality values.

Multi-arc setup

Given the potential effect of the IPT in the gravity coefficients estimation (see section 5.3.4), we only used the data acquired during the C/A of three encounters, I24, I27 and I33. Despite the interesting geometry of I25 and I32, low altitude and almost polar, both flybys were taken out of the analysis due to the IPT corruption (See figure 5.13 and 5.15).

Once the pre-processing of the data was done, besides the non-available ionospheric calibrations, the residuals were weighted on a pass-by pass strategy using the RMS of the residuals itself. As for the other Jovian bodies, the a-priori weights were chosen on the basis of past analysis and mathematical models of the expected noise.

The least-squares information filter solved for:

- Initial state of Galileo at the beginning of each arc.

- Initial state of the Satellite at the beginning of each arc.

Table 5.12 – Main orbital, geometrical and quality data characteristics of the Io flybys over Io. These values are referred to the C/A.

		I24	**I25**	**I27**	**I31**	**I32**	**I33**
Date (ERT)	(ET)	11-10-99, 04:34	26-11-99, 04:06	22-02-00, 13:47	06-08-01, 05:00	16-10-01, 01:24	17-01-02, 14:09
Altitude	(km)	603.18	292.18	189.86	185.22	176.41	93.56
Relative Velocity	(km/s)	8.0	7.89	7.27	7.08	7.72	8.91
Latitude	(deg)	4.51	−76.39	18.54	77.48	−78.54	−43.55
Longitude	(deg)	135.91	−43.98	−157.56	−171.65	136	41.86
SEP Angle	(deg)	166	143	58	39	98	161.21
Inclination	(deg)	4.52	103.5	18.56	77.7	78.93	136.43
Number of points		205	–	321	–	–	99
RMS	(mm/s)	0.136	–	0.303	–	–	0.229
C/A Data		*Y*	*Y*	*Y*	*N*	*Y*	*Y*
IPT		*Y*	*Y*	*Y*	*Y*	*Y*	*Y*

- Galileo's RTG accelerations.
- SRP scale factor.
- Io's gravity field.

Initial state of Galileo The state vector of the Galileo S/C was estimated at the beginning of each arc, approximately one day prior to the C/A. The a-priori values were obtained from the trajectory reconstructed by the Galileo navigation Team. For a-priori uncertainty we used a conservative approach, using a diagonal covariance matrix with 1-σ of 300 km for the X and Y direction, while 600 km was used for the Z direction. As for the velocity we used 0.03, 0.03 and 0.06 km/s respectively. For I33 we used the same values by a factor of three.

Initial state of the Satellites The state vector of Io was estimated at the beginning of each arc. The a-priori values of the state vector of the Galilean satellites were retrieved from the latest Jupiter ephemerides released by the JPL, JUP310. The a-priori uncertainties were set using a conservative approach, 2000 km for the X, and Y directions in position and 3000 km in Z. For the velocity 0.2, 0.2 and 0.3 km/s were used respectively. For I33 we used the same values by a factor of three.

RTG's accelerations As explained before, soon after the JOI, the navigation team of Galileo detected an acceleration of $0.4 nm/sec^2$. We set the a-priori uncertainty at 100% of its value in every direction. In the baseline solution the RTG's acceleration was a consider parameter.

Solar radiation preassure Galileo's solar radiation pressure scaling factor was set to 1.0 with an uncertainty of the 20%.

Io's gravity field The a priori values of the GM were retrieved from the JUP310 ephemerides set and J_2, C_{22} from [9]. The a-priori uncertainty of the GM was set to 10 times the formal uncertainty found in [9]. To avoid any constraint on the final results we set a large value of $5 \cdot 10^{-4}$ for all the five coefficients of the second degree and order. To examine the solution we ran different stability tests:

- SA : Single-arc, local solution for each arc with C/A data.
- MA2 : Multi-arc local solution estimating the full 2-degree gravity field.
- MA2-HE :Multi-arc local solution estimating the full 2-degree gravity field. where the ratio between J_2/C_{22} was imposed to the hydrostatic equilibrium value of 10/3.

Results

In order to obtain a conservative local multi-arc solution, we left out of the analysis all the data that could have been corrupted by the dispersive IPT. To do that, we treated as an outlier all the signatures that coincided with signatures in our IPT model, leaving us with radio tracking data of only three C/A, I24, I27 and I33.

Both I24 (September, 1996) and I27 (November, 1997) sampled an almost equatorial zone of Io, being I27 the closest encounter between them. Posteriorly, I33 (July-98),

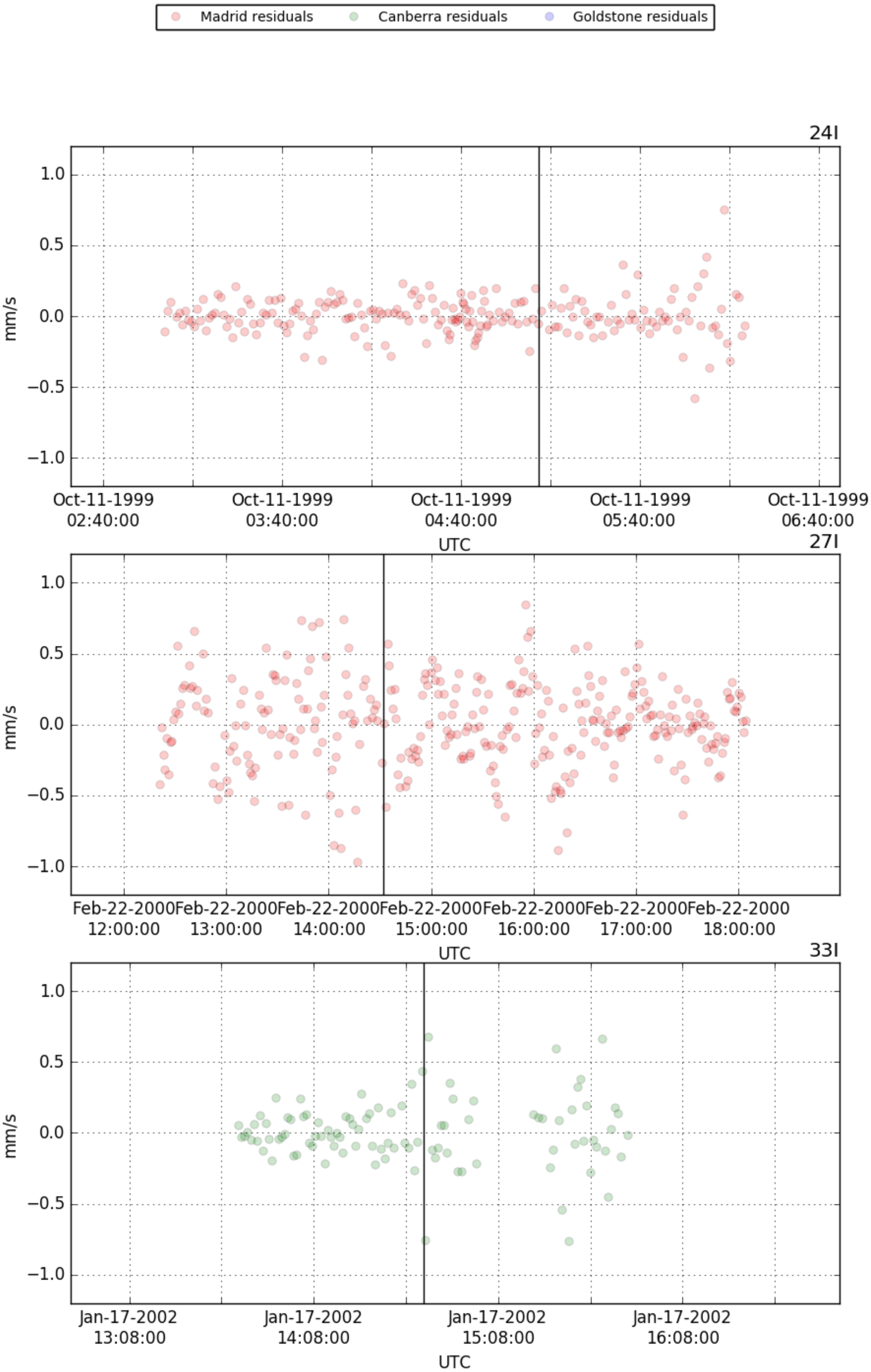

Figure 5.39 – S Band posf-fit residuals of I24, I27, I33. The vertical line corresponds to the closest approach with Io.

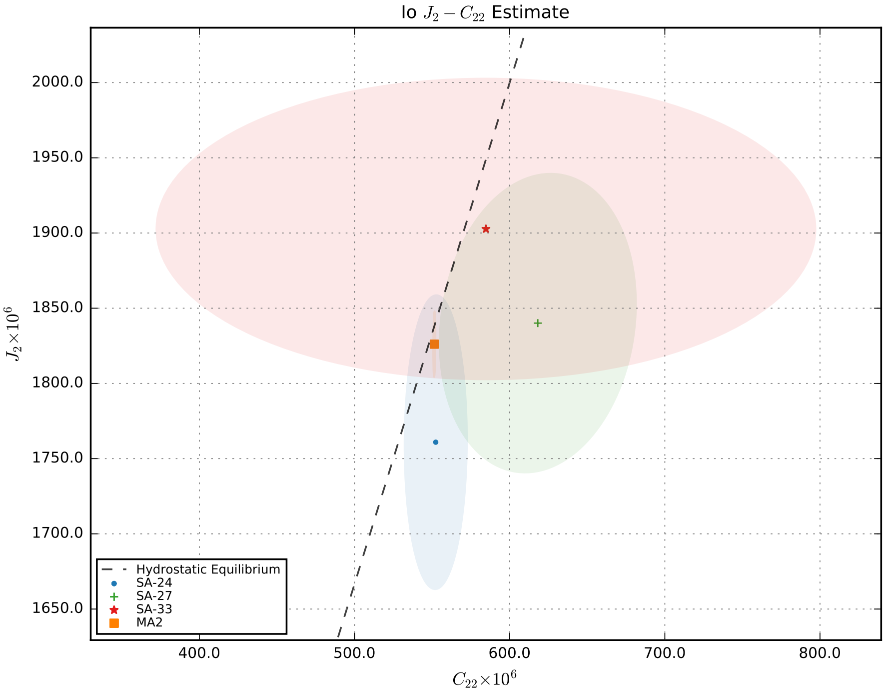

Figure 5.40 – Io single-arc solutions in the $J_2 - C_{22}, 1 - \sigma$ plane.

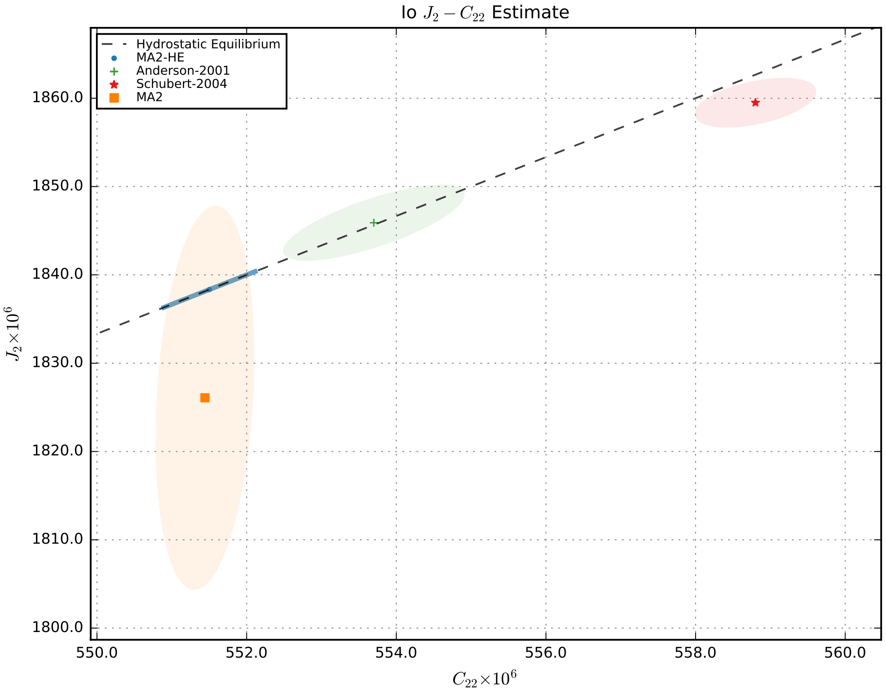

Figure 5.41 – Io multi-arc solutions in the $J_2 - C_{22}, 1 - \sigma$ plane.

sampled a different and lower latitude zone. During the last flyby of Io, Galileo entered in safe mode, shutting down all the science sequence but the radio tracking in S-band.

A pure quadrupole gravity field, was sufficient to fit the data to the noise level without signatures on the C/A. Figure 5.39 shows the obtained residuals of the single arcs, being I24 the flyby with the best data quality, and I33 the one with less usable data due to the IPT corruption.

Figure 5.40 compares the three single arc-solutions in the $J_2 - C_{22}$ plane against the multi-arc solution, showing the 1-σ compatibility with the multi-arc solution. Finally, the multi-arc solution is compared against the published reference solutions, see figure 5.41, evidencing an enormous difference of 10.14-σ in the C_{22} coefficient with respect to the reference value. Being our solution compatible within 3-σ with the precedent published result, [9], suggesting that the last Io gravity solution might be biased due to the IPT non-dynamical shift induced in the radio tracking data of I25 and I33.

Table 5.13 provides the estimated values of the baseline solutions. The MA2 solution is compatible within 1-σ with the hydrostatic equilibrium, as predicted by the theory. As stability test, the hydrostatic constraint was included between J_2 and C_{22} coefficients concluding that both solutions are statistically compatible.

Table 5.13 – Estimated gravity coefficients of Io.

		Apriori	MA2	MA2-HE
GM	(km^3/s^2)	5960±60	5956.0±4.0	5957.6±2.7
J_2	$(\times 10^6)$	1900±1000	1826±22	1838.3±2.1
C_{21}	$(\times 10^6)$	0±500	9.6±6.3	6.2±1.9
S_{21}	$(\times 10^6)$	0±500	−9.4±4.7	−11.7±2.3
C_{22}	$(\times 10^6)$	560±500	551.44±0.65	551.50±0.64
S_{22}	$(\times 10^6)$	0±500	3.11±0.37	3.09±0.36
J_2/C_{22}		3.3±3.5	3.311±0.039	10.0/3.0±0.0
corr J_2-C_{22}		+0.00	+0.22	+1.00

Just as we did for the other moons, we checked the influence of the pole position of the moon to the estimated gravity field coefficients J_2 and C_{22}, using IAU2015 rotational parameters [12], finding that both remained compatible within 0.72 and 1.66-σ respectively. More data would be needed to estimate a better pole position.

Chapter 6

Conclusions and future perspectives

The study of the gas giant satellite systems represents a challenging and currently active research field. Radio science allows us to study these complex dynamical systems, with multiple interactions happening between the different bodies involved, by means of the orbit determination of deep space probes. Radio science represents one of the key experiments of past, current and future deep space missions.

In this dissertation thesis we analysed the radio tracking data of all the deep space probes that have performed an orbit insertion manoeuvre at a gas giant satellite system so far, that is, the three unique orbiters of an outer planet, Galileo and Juno (orbiters of Jupiter) and Cassini (the unique Saturn's orbiter). One of the main objectives has been to retrieve the gravity field of both the gas giants, because gravity measurements can provide fundamental constraints on the interior of the celestial bodies and on the satellite system ephemerides, as a better gravity field restricts the motion of the satellites that orbit around it. Another objective has been to study the gravity field of the satellites and their orbital evolution, that holds, as well, information on the interior of the satellites and the evolution of the system.

With these objectives in mind, we analysed the radio tracking data, Doppler and range, of a past deep space mission, Galileo, and two current missions, Cassini that since its plunge in Saturn belongs to the past, and Juno that from now on belongs to the future as it is the only current orbiter of an outer planet.

During the last months of the Cassini mission, the Cassini S/C was set to a high eccentric, Juno-like orbit, passing through the gap between the D-ring and the cloud level, to study the interior of Saturn. The gravity analysis of the grand finale orbits provided interesting and unexpected results. A purely zonal field was not sufficient to fit the data, therefore we explored different strategies: a high degree tesseral field, with different rotation rates, and different combinations of acoustic modes. We concluded that the field can be expressed by a main zonal component, which remained stable in the different analyses, and a non-zonal or time dependent contribution. In this dissertation thesis, we explored two different hypothesis. However, the unique and definitive explanation to the anomalous contribution is still to be found.

The analysis of the Titan flybys by means of the single-satellite global approach provided a first estimation of the dissipation of Saturn at Titan's frequency, obtaining $Q_p = 115.35 \pm 36.15$. Such a present-day low Q_p value is not compatible with the classical tidal theory, which would imply a formation age smaller than the age of the solar system. Together with the recently obtained low Q_p value at Rhea's frequency, estimated using astrometric observables, the frequency-dependent nature of the gas giants dissipation has already been evidenced twice. Different theories must be explored to find an explanation to the retrieved Q_p values.

One promising explanation is the resonance locking theory, that provides plausible reasons to explain the low Q_p retrieved values, by the hypothesis that the tidal forces exerted by the moons enter in resonance with gravity modes or inertial modes that evolve with the time-scale of the Saturn's interior evolution.

As a future improvement, we will develop a global approach capable to study the orbital evolution of the main Saturn satellites, with the objective of estimating the different Q_p at different tidal forcing frequencies using all the available radio tracking data.

Regarding Juno, the gravity experiment provided the first accurate estimation of the zonal gravity coefficients up to J_{10}, improving by far the previous results and the knowledge of the interior structure of the gas giant. This was possible thanks to the high eccentric and low pericenter orbit that the S/C follows around Jupiter, together with the radio science instrumentation that allows to use the dual link calibration and remove to a large extent the dispersive effects, induced by the IPT and the solar plasma. The multi-frequency link calibration offered the opportunity to perform IPT occultations that, combined to a recent parametric model, can be used to study its time and longitudinal variability. However, we acknowledge that, so far, this technique is limited to the X/X-X/Ka passages. Most probably, this limitation is the result of a station delay in the uplink Ka-band, which itself induces an unexplained path delay shape. In any case, this unexpected trend in the path delay of the X/X-Ka/Ka passages does not induce bias in the Jupiter gravity measurements.

The subsequent encounters with Jupiter will help to single out the high order zonal harmonics, the tesseral field, and the gravity signature induced by the great red spot. Such a gravity field will provide crucial constraints on the interior of the gas giant. In addition, once the strange trend found on the path delay of the X/X-Ka/Ka encounters will be figured out, there will be available additional IPT occultations that will be useful to improve the torus shape and study its variability in longitude and time.

The re-analysis of the Galileo radio tracking data provided a new angle to the gravity experiment performed two decades ago. Analysing the old radio tracking data with the new knowledge of the Jupiter system, fed by the Juno S/C, has proven really useful.

The new gravity field constrained better the motion of the Galilean satellites and the Galileo orbiter. The new understanding of the Io plasma torus by means of new models and the study of its potential effect on the gravity experiments, due to the non-dynamical Doppler shift introduced in the radio signals, allowed us to discriminate between the different affected passes and sort out the ones that were corrupted. Also, the multi-arc technique provided a new way to process the radio tracking observables. Compared to the weighted mean, the multi-arc technique provided an improved estimation, because the new method takes into account the correlations between the estimated parameters. Finally, the local approach allowed to study the gravity of the Galilean satellites without taking into account their orbital evolution. This approach was really useful because, given the small amount of observables and all the data-availability problems, we were not able to follow properly the evolution of the satellites using the global approach.

Summarizing, the previous reasons allowed us to study the effect of the Io plasma torus during the Galileo mission, finding that the use of all the data acquired during most of the Io encounters could cause big trouble on the measurement of Io gravity coefficients. The four Galilean satellites proved to be compatible with the hydrostatic equilibrium even though we did not apply the hydrostaticity constraint on our baseline solutions.

The estimated gravity coefficients of Europa and Io are substantially different from the published estimation of the RS Team, result that can be useful to constrain their interior structure and also for the future navigation of both JUICE and Europa Clipper.

In the future, we would like to make improvements on the Io plasma torus model using the residuals signatures found in the Doppler data, highlighted earlier in this dissertation thesis. This would make usable some data that nowadays cannot be used for our analyses and almost certainly would improve the obtained results.

To conclude, the study of the gas giant satellite systems is a vast research subject. In this dissertation thesis we provided answers for some previously unknown questions, such as the dissipation in Saturn at Titan's frequency or the gravity of the gas giants. At the same time we discovered new research subjects, questions whose answer still remain veiled and will be discussed and looked into more thoroughly in the future, just like the unexplained contribution to the gravity field of Saturn. Mostly sure, the future missions to the gas giant satellite systems, like JUICE or Europa Clipper, or a forthcoming Saturn mission, or maybe an upcoming re-analysis of one of the missions studied in this thesis, like the one performed with Galileo, will provide answers to the open questions found during this study.

List of Figures

List of Tables

Bibliography

[1] Cassini diagrams. `https://solarsystem.nasa.gov/resources/all/?order=pub_date+desc&per_page=50&page=0&search=cassini+diagram&fs=&fc=&ft=&category=`. Accessed: 2018-09-01.

[2] Discovered planetary satellites. `https://ssd.jpl.nasa.gov/?sat_discovery`. Accessed: 2018-09-01.

[3] JD Anderson, RA Jacobson, TP McElrath, WB Moore, G Schubert, and PC Thomas. Shape, mean radius, gravity field, and interior structure of callisto. *Icarus*, 153(1):157–161, 2001.

[4] JD Anderson, EL Lau, WL Sjogren, G Schubert, and WB Moore. Gravitational constraints on the internal structure of ganymede. *Nature*, 384(6609):541, 1996.

[5] JD Anderson, EL Lau, WL Sjogren, G Schubert, and WB Moore. Europa's differentiated internal structure: Inferences from two galileo encounters. *Science*, 276(5316):1236–1239, 1997.

[6] JD Anderson, G Schubert, RA Jacobson, EL Lau, WB Moore, and WL Sjogren. Distribution of rock, metals, and ices in callisto. *Science*, 280(5369):1573–1576, 1998.

[7] JD Anderson, G Schubert, RA Jacobson, EL Lau, WB Moore, and WL Sjogren. Europa's differentiated internal structure: Inferences from four galileo encounters. *Science*, 281(5385):2019–2022, 1998.

[8] JD Anderson, WL Sjogren, and G Schubert. Galileo gravity results and the internal structure of io. *Science*, 272(5262):709–712, 1996.

[9] John D Anderson, Robert A Jacobson, Eunice L Lau, William B Moore, and Gerald Schubert. Io's gravity field and interior structure. *Journal of Geophysical Research: Planets*, 106(E12):32963–32969, 2001.

[10] John D Anderson, Gerald Schubert, Robert A Jacobson, Eunice L Lau, William B Moore, and Jennifer L Palguta. Discovery of mass anomalies on ganymede. *Science*, 305(5686):989–991, 2004.

[11] PG Antreasian, TP McElrath, RJ Haw, GD Lewis, and T Krisher. Galileo orbit determination results during the satellite tour. 1997.

[12] BA Archinal, CH Acton, MF A'Hearn, A Conrad, GJ Consolmagno, T Duxbury, D Hestroffer, JL Hilton, RL Kirk, SA Klioner, et al. Report of the iau working group on cartographic coordinates and rotational elements: 2015. *Celestial Mechanics and Dynamical Astronomy*, 130(3):22, 2018.

[13] F Bagenal, FJ Crary, AIF Stewart, NM Schneider, DA Gurnett, WS Kurth, LA Frank, and WR Paterson. Galileo measurements of plasma density in the io torus. *Geophysical research letters*, 24(17):2119–2122, 1997.

[14] F Bagenal, LP Dougherty, KM Bodisch, JD Richardson, and JM Belcher. Survey of voyager plasma science ions at jupiter: 1. analysis method. *Journal of Geophysical Research: Space Physics*, 122(8):8241–8256, 2017.

[15] Fran Bagenal. Empirical model of the io plasma torus: Voyager measurements. *Journal of Geophysical Research: Space Physics*, 99(A6):11043–11062, 1994.

[16] Fran Bagenal, Timothy E Dowling, and William B McKinnon. *Jupiter: the planet, satellites and magnetosphere*, volume 1. Cambridge University Press, 2007.

[17] Fran Bagenal and James D Sullivan. Direct plasma measurements in the io torus and inner magnetosphere of jupiter. *Journal of Geophysical Research: Space Physics*, 86(A10):8447–8466, 1981.

[18] Cesare Barbieri, Jürgen H Rahe, Torrence V Johnson, and Anita M Sohus. *The three Galileos: The man, the spacecraft, the telescope*, volume 220. Springer Science & Business Media, 2013.

[19] Julie Bellerose, Duane Roth, and Kevin Criddle. The cassini mission: Reconstructing thirteen years of the most complex gravity-assist trajectory flown to date. In *2018 SpaceOps Conference*, page 2646, 2018.

[20] B Bertotti, G Comoretto, and L Iess. Doppler tracking of spacecraft with multi-frequency links. *Astronomy and Astrophysics*, 269:608–616, 1993.

[21] Bruno Bertotti, Paolo Farinella, and David Vokrouhlicky. *Physics of the solar system: dynamics and evolution, space physics, and spacetime structure*, volume 293. Springer Science & Business Media, 2012.

[22] Gerald J Bierman. *Factorization methods for discrete sequential estimation.* Courier Corporation, 2006.

[23] SJ Bolton et al. The juno mission. *Proceedings of the International Astronomical Union*, 6(S269):92–100, 2010.

[24] JK Campbell and SP Synnott. Gravity field of the jovian system from pioneer and voyager tracking data. *The Astronomical Journal*, 90:364–372, 1985.

[25] Michael H Carr, Michael JS Belton, Clark R Chapman, Merton E Davies, Paul Geissler, Richard Greenberg, Alfred S McEwen, Bruce R Tufts, Ronald Greeley, Robert Sullivan, et al. Evidence for a subsurface ocean on europa. *Nature*, 391(6665):363, 1998.

[26] Sébastien Charnoz, Aurélien Crida, Julie C Castillo-Rogez, Valery Lainey, Luke Dones, Özgür Karatekin, Gabriel Tobie, Stephane Mathis, Christophe Le Poncin-Lafitte, and Julien Salmon. Accretion of saturn's mid-sized moons during the viscous spreading of young massive rings: Solving the paradox of silicate-poor rings versus silicate-rich moons. *Icarus*, 216(2):535–550, 2011.

[27] Louis A D'Amario, Larry E Bright, and Aron A Wolf. Galileo trajectory design. *Space science reviews*, 60(1-4):23–78, 1992.

[28] Michael D Desch and ML Kaiser. Voyager measurement of the rotation period of saturn's magnetic field. *Geophysical Research Letters*, 8(3):253–256, 1981.

[29] Michael Efroimsky and Valeri V Makarov. Tidal friction and tidal lagging. applicability limitations of a popular formula for the tidal torque. *The Astrophysical Journal*, 764(1):26, 2013.

[30] Esposito P. B. Ekelund, J. E. and R. Benson. Dptraj-dp user's reference manual. *NASA STI/Technical Report*, 1, 1996.

[31] Scott Evans, William Taber, Theodore Drain, Jonathon Smith, Hsi-Cheng Wu, Michelle Guevara, Richard Sunseri, and James Evans. Monte: the next generation of mission design and navigation software. *CEAS Space Journal*, 10(1):79–86, 2018.

[32] WM Folkner, L Iess, JD Anderson, SW Asmar, DR Buccino, D Durante, M Feldman, L Gomez Casajus, M Gregnanin, A Milani, et al. Jupiter gravity field estimated from the first two juno orbits. *Geophysical Research Letters*, 44(10):4694–4700, 2017.

[33] Jim Fuller, Jing Luan, and Eliot Quataert. Resonance locking as the source of rapid tidal migration in the jupiter and saturn moon systems. *Monthly Notices of the Royal Astronomical Society*, 458(4):3867–3879, 2016.

[34] PE Geissler and MT McMillan. Galileo observations of volcanic plumes on io. *Icarus*, 197(2):505–518, 2008.

[35] Giacomo Giampieri, MK Dougherty, EJ Smith, and CT Russell. A regular period for saturn's magnetic field that may track its internal rotation. *Nature*, 441(7089):62, 2006.

[36] TV Gudkova and VN Zharkov. Theoretical free oscillations spectrum for saturn interior models. *Advances in Space Research*, 38(4):764–769, 2006.

[37] Tristan Guillot, Y Miguel, B Militzer, WB Hubbard, Y Kaspi, E Galanti, H Cao, R Helled, SM Wahl, L Iess, et al. A suppression of differential rotation in jupiter's deep interior. *Nature*, 555(7695):227, 2018.

[38] DA Gurnett, WS Kurth, GB Hospodarsky, AM Persoon, TF Averkamp, B Cecconi, A Lecacheux, P Zarka, P Canu, N Cornilleau-Wehrlin, et al. Radio and plasma wave observations at saturn from cassini's approach and first orbit. *Science*, 307(5713):1255–1259, 2005.

[39] R Haw, P Antreasian, T McElrath, and G Lewis. Navigating galileo in the jovian system. 1999.

[40] MM Hedman and PD Nicholson. Kronoseismology: using density waves in saturn's c ring to probe the planet's interior. *The Astronomical Journal*, 146(1):12, 2013.

[41] Ravit Helled, Eli Galanti, and Yohai Kaspi. Saturn's fast spin determined from its gravitational field and oblateness. *Nature*, 520(7546):202, 2015.

[42] H Hussmann, Ch Sotin, and JI Lunine. Interiors and evolution of icy satellites. 2007.

[43] L. Iess, B. Militzer, Y. Kaspi, P. Nicholson, D. Durante, P. Racioppa, A. Anabtawi, E. Galanti, W. Hubbard, M. J. Mariani, P. Tortora, S. Wahl, and M. Zannoni. Measurement and implications of saturn's gravity field and ring mass. 2019.

[44] Luciano Iess, Mauro Di Benedetto, Nick James, Mattia Mercolino, Lorenzo Simone, and Paolo Tortora. Astra: Interdisciplinary study on enhancement of the end-to-end accuracy for spacecraft tracking techniques. *Acta Astronautica*, 94(2):699–707, 2014.

[45] Luciano Iess, WM Folkner, D Durante, M Parisi, Y Kaspi, E Galanti, T Guillot, WB Hubbard, DJ Stevenson, JD Anderson, et al. Measurement of jupiter's asymmetric gravity field. *Nature*, 555(7695):220, 2018.

[46] Luciano Iess, Robert A Jacobson, Marco Ducci, David J Stevenson, Jonathan I Lunine, John W Armstrong, Sami W Asmar, Paolo Racioppa, Nicole J Rappaport, and Paolo Tortora. The tides of titan. *Science*, page 1219631, 2012.

[47] Luciano Iess, Nicole J Rappaport, Robert A Jacobson, Paolo Racioppa, David J Stevenson, Paolo Tortora, John W Armstrong, and Sami W Asmar. Gravity field, shape, and moment of inertia of titan. *Science*, 327(5971):1367–1369, 2010.

[48] R Jacobson, R Haw, T Elrath, and P Antreasian. A comprehensive orbit reconstruction for the galileo prime mission in the j2000 system. 1999.

[49] RA Jacobson, PG Antreasian, JJ Bordi, KE Criddle, R Ionasescu, JB Jones, RA Mackenzie, MC Meek, D Parcher, FJ Pelletier, et al. The gravity field of the saturnian system from satellite observations and spacecraft tracking data. *The Astronomical Journal*, 132(6):2520, 2006.

[50] Robert Jacobson. Status of the post-cassini saturnian satellite ephemerides. In *42nd COSPAR Scientific Assembly*, volume 42, 2018.

[51] Xianzhe Jia, Margaret G Kivelson, Krishan K Khurana, and William S Kurth. Evidence of a plume on europa from galileo magnetic and plasma wave signatures. *Nature Astronomy*, page 1, 2018.

[52] Y Kaspi, E Galanti, WB Hubbard, DJ Stevenson, SJ Bolton, L Iess, T Guillot, J Bloxham, JEP Connerney, H Cao, et al. Jupiter's atmospheric jet streams extend thousands of kilometres deep. *Nature*, 555(7695):223, 2018.

[53] Yohai Kaspi, Eli Galanti, Luciano Iess, and Daniele Durante. Comparing the deep dynamics on jupiter and saturn in light of the juno and cassini gravity experiments. In *AAS/Division for Planetary Sciences Meeting Abstracts*, volume 50, 2018.

[54] William M Kaula. Tidal dissipation by solid friction and the resulting orbital evolution. *Reviews of Geophysics*, 2(4):661–685, 1964.

[55] William M Kaula. An introduction to planetary physics-the terrestrial planets. *Space Science Text Series, New York: Wiley, 1968*, 1968.

[56] WM Kaula. Theory of satellite geodesy: Applications of satellites to geodesy (mineola, ny, 2000.

[57] MG Kivelson, KK Khurana, CT Russell, RJ Walker, J Warnecke, FV Coroniti, C Polanskey, DJ Southwood, and G Schubert. Discovery of ganymede's magnetic field by the galileo spacecraft. *Nature*, 384(6609):537, 1996.

[58] MG Kivelson, KK Khurana, and M Volwerk. The permanent and inductive magnetic moments of ganymede. 2002.

[59] I Kupo, Yu Mekler, Y Mekler, and A Eviatar. Detection of ionized sulfur in the jovian magnetosphere. *The Astrophysical Journal*, 205:L51–L53, 1976.

[60] Valéry Lainey, Jean-Eudes Arlot, Özgür Karatekin, and Tim Van Hoolst. Strong tidal dissipation in io and jupiter from astrometric observations. *Nature*, 459(7249):957, 2009.

[61] Valéry Lainey, Robert A Jacobson, Radwan Tajeddine, Nicholas J Cooper, Carl Murray, Vincent Robert, Gabriel Tobie, Tristan Guillot, Stéphane Mathis, Françoise Remus, et al. New constraints on saturn's interior from cassini astrometric data. *Icarus*, 281:286–296, 2017.

[62] Valéry Lainey, Özgür Karatekin, Josselin Desmars, Sébastien Charnoz, Jean-Eudes Arlot, Nicolai Emelyanov, Christophe Le Poncin-Lafitte, Stéphane Mathis, Françoise Remus, Gabriel Tobie, et al. Strong tidal dissipation in saturn and constraints on enceladus'thermal state from astrometry. *The Astrophysical Journal*, 752(1):14, 2012.

[63] Rosaly Lopes-Gautier, Alfred S McEwen, William B Smythe, PE Geissler, L Kamp, AG Davies, JR Spencer, L Keszthelyi, R Carlson, FE Leader, et al. Active volcanism on io: Global distribution and variations in activity. *Icarus*, 140(2):243–264, 1999.

[64] Christopher Mankovich, Mark S Marley, Jonathan J Fortney, and Naor Movshovitz. Cassini ring seismology as a probe of saturn's interior i: Rigid rotation. *arXiv preprint arXiv:1805.10286*, 2018.

[65] John W Marini. Correction of satellite tracking data for an arbitrary tropospheric profile. *Radio Science*, 7(2):223–231, 1972.

[66] G Mariotti and P Tortora. Experimental validation of a dual uplink multifrequency dispersive noise calibration scheme for deep space tracking. *Radio Science*, 48(2):111–117, 2013.

[67] Dennis L Matson, Linda J Spilker, and Jean-Pierre Lebreton. The cassini/huygens mission to the saturnian system. In *The Cassini-Huygens Mission*, pages 1–58. Springer, 2003.

[68] Michael Meltzer. Mission to jupiter: a history of the galileo project. *NASA STI/Recon Technical Report N*, 7, 2007.

[69] Rachele Meriggiola, Luciano Iess, Bryan W Stiles, Jonathan I Lunine, and Giuseppe Mitri. The rotational dynamics of titan from cassini radar images. *Icarus*, 275:183–192, 2016.

[70] Andrea Milani and Giovanni Gronchi. *Theory of orbit determination.* Cambridge University Press, 2010.

[71] TD Moyer. Descanso book series deep space communications and navigation series, ed joseph h, 2000.

[72] Theodore D Moyer. Mathematical formulation of the double precision orbit determination program/dpodp. 1971.

[73] Carl D Murray and Stanley F Dermott. *Solar system dynamics.* Cambridge university press, 1999.

[74] Edward G Nerney, Fran Bagenal, and Andrew J Steffl. Io plasma torus ion composition: Voyager, galileo, and cassini. *Journal of Geophysical Research: Space Physics*, 122(1):727–744, 2017.

[75] Francis Nimmo, Amy C Barr, Marie Běhounková, and William B McKinnon. The thermal and orbital evolution of enceladus: observational constraints and models. *Enceladus and the Icy Moons of Saturn*, page 79, 2018.

[76] H Nozawa, H Misawa, S Takahashi, A Morioka, S Okano, and R Sood. Long-term variability of [sii] emissions from the io plasma torus between 1997 and 2000. *Journal of Geophysical Research: Space Physics*, 109(A7), 2004.

[77] GW Null. Gravity field of jupiter and its satellite from pioneer 10 and pioneer 11 tracking data. *The Astronomical Journal*, 81:1153–1161, 1976.

[78] Jennifer Palguta, John D Anderson, Gerald Schubert, and William B Moore. Mass anomalies on ganymede. *Icarus*, 180(2):428–441, 2006.

[79] SJ Peale and P Cassen. Contribution of tidal dissipation to lunar thermal history. *Icarus*, 36(2):245–269, 1978.

[80] Phillip H Phipps and Paul Withers. Radio occultations of the io plasma torus by juno are feasible. *Journal of Geophysical Research: Space Physics*, 122(2):1731–1750, 2017.

[81] Lorenz Roth, Joachim Saur, Kurt D Retherford, Darrell F Strobel, Paul D Feldman, Melissa A McGrath, and Francis Nimmo. Transient water vapor at europa's south pole. *Science*, page 1247051, 2013.

[82] Bob Schutz, Byron Tapley, and George H Born. *Statistical orbit determination*. Elsevier, 2004.

[83] WB Sparks, KP Hand, MA McGrath, E Bergeron, M Cracraft, and SE Deustua. Probing for evidence of plumes on europa with hst/stis. *The Astrophysical Journal*, 829(2):121, 2016.

[84] Jim Taylor, Kar-Ming Cheung, Dongae Seo, et al. Galileo telecommunications. *DESCANSO design and performance summary series*, 2002.

[85] Nicolas Thomas. The variability of the io plasma torus. *Journal of Geophysical Research: Planets*, 98(E10):18737–18750, 1993.

[86] Catherine L Thornton and James S Border. *Radiometric tracking techniques for deep-space navigation*. John Wiley & Sons, 2003.

[87] David A Vallado. *Fundamentals of astrodynamics and applications*, volume 12. Springer Science & Business Media, 2001.

[88] Sean M Wahl, William B Hubbard, and Burkhard Militzer. Tidal response of preliminary jupiter model. *The Astrophysical Journal*, 831(1):14, 2016.

[89] Sean M Wahl, William B Hubbard, and Burkhard Militzer. The concentric maclaurin spheroid method with tides and a rotational enhancement of saturn's tidal response. *Icarus*, 282:183–194, 2017.

[90] JM Wahr, MT Zuber, DE Smith, and JI Lunine. Tides on europa, and the thickness of europa's icy shell. *Journal of Geophysical Research: Planets*, 111(E12), 2006.

[91] Marco Zannoni. *Development Of New Toolkits For Orbit Determination Codes For Precise Radio Tracking Experiments.* PhD thesis, alma, 2014.

[92] Christophe Zimmer, Krishan K Khurana, and Margaret G Kivelson. Subsurface oceans on europa and callisto: Constraints from galileo magnetometer observations. *Icarus*, 147(2):329–347, 2000.